High-Order Harmonic Spectroscopy of Molecular Structure and Dynamics

by

Xibin Zhou

B.S., University of Science and Technology of China, 2003

M.S., University of Colorado, 2008

A thesis submitted to the
Faculty of the Graduate School of the
University of Colorado in partial fulfillment
of the requirements for the degree of
Doctor of Philosophy
Department of Physics
2009

This thesis entitled:
High-Order Harmonic Spectroscopy of Molecular Structure and Dynamics
written by Xibin Zhou
has been approved for the Department of Physics

Prof. Margaret M. Murnane

Prof. Henry C. Kapteyn

Date

The final copy of this thesis has been examined by the signatories, and we find that both the content and the form meet acceptable presentation standards of scholarly work in the above mentioned discipline.

Zhou, Xibin (Ph.D., Physics)

High-Order Harmonic Spectroscopy of Molecular Structure and Dynamics

Thesis directed by Prof. Margaret M. Murnane and Prof. Henry C. Kapteyn

The recent developments of high repetition rate and high average power ultrafast laser open the door for probing molecular structure and dynamics with intense laser fields. In this regime, the electric field of the laser is comparable to the binding field of the electron in the outer valence shell of atoms or molecules. Thus the potential is strongly modified by the laser electric field as compared to field-free atomic or molecular potential, and the probability for ionization is dramatically enhanced.

High harmonic generation (HHG), as an ionization-initiated strong field process, can be explained well by the semiclassical recollision model. In this work, we demonstrate HHG as a new spectroscopic method for determining the molecular structure of simple linear molecules (such as N_2 and CO_2), and for monitoring the real-time molecular dynamics of polyatomic molecules (such as N_2O_4).

First, we use an extreme-ultraviolet interferometry to measure the phase of high-order harmonic generation from transiently aligned CO_2 molecules. We unambiguously observe a reversal in phase of the high order harmonic emission for higher harmonic orders with a sufficient degree of alignment. This results from molecular-scale quantum interferences between the molecular electronic wave function and the re-colliding electron as it recombines with the molecule, and it is consistent with a plane wave model. We also perform similar experiments with N_2 molecules and observe behaviors that can not be predicted by the plane-wave model.

Second, we perform an accurate polarimetry measurement of high harmonic emission from aligned molecules. Surprisingly, we find that harmonic emission from N_2 molecules can be strongly elliptically polarized even when driven by linearly polarized laser fields. We extract the phase difference between the parallel and perpendicular components of the high harmonic field, which strongly depends on the harmonic order. This nontrivial phase indicates a breakdown of plane wave approximation. This work also shows that it is possible to engineer the polarization properties of harmonic emission by carefully preparing a molecular medium.

Finally, we show that high harmonic emission can reveal coupled electronic and nuclear dynamics in polyatomic molecules. By exciting large amplitude and relative slow vibrations in the N_2O_4 molecule, we show that tunnel ionization accesses the ground state of the ion at the outer turning point of the vibration, whereas the first excited state is populated at the inner turning point of the vibration motion. This state switching due to the coupled electronic and nuclear motions is manifested as bright bursts of high harmonic light that are emitted mostly at the outer turning point of the vibration, due to the different symmetries of the ground state and the first excited state of the cation.

Dedication

To my parents and to my wife.

Acknowledgements

First of all, I would like to thank my academic advisors, Profs. Henry Kapteyn and Margaret Murnane for teaching me the experimental skills from scratch and for giving me the freedom to explore the topics that interested me. Without their patient guidance and generous support, this dissertation would not have been possible.

I would like to thank my close collaborators in the lab, Robynne Lock, Dr. Wen Li, Dr. Nicholas Wagner, and Dr. Andrea Wüest for their inspiring discussions and hard work during the last three years I worked on the molecular HHG project.

I would also like to thank many people in Kapteyn-Murnane group who have taught me so much about lasers, optics, computer programming and of course, physics at various stages of my graduate school career. These include Xiaoshi Zhang, Tenio Popmintchev, Daisy Raymondson, David Gaudiosi, Ariel Paul, Luis Miaja Avila, Oren Cohen, Amy Lytle, Etienne Gagnon, Mark Siemens, Paul Alphin, Qing Li , Ming-chan Chen and Jing Yin. I always appreciate the interactions and discussions with all the members of KM group.

Helpful discussions and collaborations with people outside the KM group and JILA, especially many theorists, are appreciated as well. Special thanks goes to Zach Walter, Drs. Chris Greene, Ramakrishna Shankar, Tamar Seideman, An-Thu Le, Chii-Dong Lin, Xinhua Xie, and Olga Smirnova, Serguei Patchkovskii and Albert Stolow.

I would like to thank the staffs at the JILA machine shop, electronic shop and computing facility for the help they gave me.

Finally I would like to thank my wife, Jianying, for all the caring and love during the last six years. The encouragement and love from her have always kept me cheerful, even when my experiments are not working as planned. She has also helped me discover interest outside physics and the lab.

Contents

Chapter

Appendix

Tables

Table

Figures

Figure

Chapter 1

Introduction

1.1 Laser spectroscopy: an overview

Linear and nonlinear laser optical spectroscopies of gas phase atoms and molecules in the perturbative regime have become major tools for understanding the light-matter interaction [1, 2]. What we have learned from the optical spectroscopy experiments is central to the understanding of quantum mechanics and its application in a multitude of areas in physics and chemistry.

The instruments for a typical laser spectroscopy experiment are usually made up of three major components.

- One or more laser sources at varying wavelengths, intensities, and pulse durations.
- A gas-phase sample that is prepared and injected into an interaction chamber.
- A detection system for detecting the products of the light-matter interaction, which consists of the detection of photons and/or particles resulting from ionization or fragmentation. A spectrometer and photon detector system can measure the intensity and wavelength of the transmitted and scattered light and the spontaneous fluorescence after excitation. The electrons and charged ions resulting from the fragmentation of the atoms or molecules can be detected by an energy resolved time-of-flight mass spectrometer.

While breakthroughs in each of these three component technologies contributes to the progress of laser spectroscopy, the most important component may be the development of new laser sources. Early laser optical spectroscopy techniques—such as absorption spectroscopy and laser induced fluorescence at difference wavelengths—mainly investigated the bound-bound transition between the electronic, vibrational, and rotational states. Recently pushing the spectral line measurement to higher resolution has initiated a number of breakthroughs in physics, such as the realization of Bose-Einstein condensation in dilute atomic gases [3] and the discovery of frequency comb techniques [4].

Ionization spectroscopy [2], especially photoelectron spectroscopy with high energy photons (UV, VUV, EUV and Soft X ray) and resonance enhanced multiphoton ionization (REMPI) allow the investigation of the bound-continuum transition. Compared to high energy photons, REMPI is state selective, thus the state distribution of the molecular fragment offers interesting information about the molecular process. These techniques have become available in many physical chemistry laboratories.

With the development of short pulse laser technologies, such as cavity dumping and Q-switching, nanosecond pulsed lasers with 10^6 W/cm^2 focused intensity become possible. Rich nonlinear optical phenomena come into play at this intensity, including nonlinear harmonic generation and coherent Raman scattering.

Passive mode locking techniques [5], first invented using dye laser (colliding pulse mode locking), then advancing to solid state Ti: Sapphire laser (Kerr lens mode locking). This progress has pushed the pulse duration to picosecond (ps) and femtosecond (fs). Using the femtosecond lasers, ultrafast spectroscopy employing pump-probe techniques enables real time monitoring of molecular dynamics [6]. For the first time, the time evolution of rotational and vibrational dynamics of molecules could be observed in time domain and compared to theoretical calculations. Although time-domain techniques trade off time resolution at the expense of spectral resolution, a good understanding of wave packet motion formed by the superposition of a large number of states has offered a playground for studying and controlling atom motion in molecules [7]. By combining high power Ti: Sapphire laser and nonlinear optical frequency conversion techniques, such as harmonic generation in crystal and gases and optical parametric amplification, it becomes possible to generate an ultrafast rainbow covering from the ultraviolet (UV) to the infrared (IR), and this source can readily be used to explore molecular physics and chemistry. Combination of new pump-probe technique with traditional laser spectroscopy technique, results in techniques such as transient absorption, femtosecond photoelectron spectroscopy, Raman spectroscopy, etc..

In addition to advances in laser development, gas sample preparation techniques have also made considerable progress. Molecular motion can be slowed down by the adiabatic expansion in a supersonic molecular beam, which enhances the resolution of the energy and momentum resolved spectroscopy. Experimental detection methods have also been improved. Photon counting makes it possible to observe new phenomena at single photon level, while charged coupled device (CCD) cameras sensitive to various wavelength light can collect data with very low noise level [8]. On the charged particle side, angular resolved photoion and photoelectron imaging and coincidence techniques can retrieve the 3D vector momentum of the charged particle from a specific reaction channel and offer more detailed information about molecular fragmentations and reactions [9, 10].

1.2 Strong field spectroscopy of molecules

In all of the spectroscopy techniques mentioned above, the interaction between the atomic or molecular electron and the external light field is considerably weaker than the Coulomb binding force between the nucleus and the electron; i.e. the electron wave function is only slightly reshaped by the external field. Theoretically, the laser atom interaction can be treated as a perturbation to the field free atomic or molecular Hamiltonian.

State-of-the-art ultrashort pulse lasers offer not only higher temporal resolution, but also the possibility to generate more intense light. Chirp pulse amplification techniques have advanced to the point that sub-50fs pulses with 10^{12} to 10^{16} W/cm^2 intensity can routinely be generated by table-top lasers at high repetition rate. The electric field at the focus is comparable to the binding electric field between the nucleus and the electrons. For the hydrogen atom, the binding electric field is 5.2×10^9 V/m (corresponding to an intensity of 3.5×10^{16} W/cm^2).

In this intensity regime, a fascinating phenomenon is the high-order harmonic generation (HHG) process, In HHG, by focusing a Ti: Sapphire laser at a center wavelength of 790nm (photon energy 1.56 eV) into a gas sample, we can generate a frequency comb at the odd-order frequencies of the fundamental laser light. The centrosymmetry of the gas medium prevents the generation of even-order harmonics. Unlike in the perturbative regime where the harmonics decrease exponentially with the harmonic order, the plateau region high harmonics in this intensity regime can span a few hundred eV in energy and can extend to the keV range [11].

The work in this dissertation includes studying the HHG from an aligned or excited molecular sample. On one hand, we demonstrate that information about molecular structure and dynamics can be encoded on the various properties of the HHG, such as intensity, phase, and polarization. These data have broad implications for the theory of molecules in strong fields because they cannot be explained by simple theories based on strong field approximation (SFA) and single active electron approximation (SAEA). On the other hand, when combined with the intrinsic temporal resolution of HHG, simultaneous measurements of structure and dynamics are possible. This shows possibility of making a molecular movie with HHG during during a fast reaction process.

1.3 Outline of this dissertation

This dissertation is organized as follows:

In Chapter 2, we review the theoretical and experimental background of HHG generation in atoms. To model the HHG from single atoms, two methods can be used, the time-dependent Schrödinger equation and the semiclassical three step model [12, 13, 14]. Much of our insight about the HHG process was gained from the classical three step model and its quantum mechanical correspondence, the Lewenstein model.

In Chapter 3, we discuss the motivation to study HHG from molecules and introduce the theoretical and experimental background of HHG generation in molecules. We also review previous experiments that initiate the efforts to develop HHG as a spectroscopy tool for molecules.

Chapter 4 presents experimental work on the measurement of the intensity and phase of HHG emission from transiently aligned molecules. Experimental results on three simple molecules N_2, CO_2 and N_2O are presented and compared with a two-charge-center quantum interference model which is based on a plane wave approximation of the recolliding electron. The data on CO_2 and N_2O molecules can be explained well by the two-charge-center model. However, this simple model does not work very well for N_2 molecules.

Chapter 5 presents two experiments. First, we perform an accurate polarimetry measurement of high harmonic emission from aligned molecules. We find that harmonic emission from nitrogen molecules can be strongly elliptically polarized; even when driven by linearly polarized laser fields. Furthermore, we extract the relative phase difference between the parallel and perpendicular components of the high harmonic field, which strongly depends on the harmonic order. This work also shows that it is possible to engineer the polarization properties of harmonic emission by carefully preparing a molecular medium. In the second experiment, we vary the ellipticity of the driving laser used to generate the high harmonic emission. We find that the HHG intensity from aligned molecules does not optimize with linear polarization of the driving laser (as in the atomic case), but rather peaks at a small positive or negative ellipticity. The sign and degree of this ellipticity depend on the molecular orientation.

In Chapter 6, we investigate the HHG from vibrating N_2O_4 molecules. We show that the intrinsic properties of HHG make it a very promising tool for time resolved measurement of molecular dynamics. However, due to the complexity of this process, to make further progress, it will be very important to develop and test new theories beyond the strong field approximation.

In chapter 7, we summarize the results and point to future directions.

In the appendix, we present another experiment conducted earlier, and indirectly related to the main line of this dissertation. In this experiment, We demonstrate for the first time that 0.45 μJ pulses can be obtained from a cavity-dumped Ti: Sapphire oscillator stably operating in the positive dispersion regime. The output pulse can be compressed to 60 fs and used to generate a white light continuum through self-filamentation in a thin sapphire plate.

Chapter 2

Theory of High-Order Harmonic Generation—The three-step model

In the laser intensity range of 10^{13} to 10^{16} W/cm^2, the strong field atomic and molecular phenomena result from the extreme distortion of the electronic wave function of an atom or molecule in the presence of the laser electric field.

To deal with the strong field response of atoms and molecules in general, and HHG in particular, the most rigorous, but computationally-demanding method is the direct integration of the time-dependent Schrödinger equation (TDSE):

$$\frac{\partial\psi(\mathbf{r},t)}{\partial t} = \frac{1}{i\hbar}\left[-\frac{\hbar^2}{2m}\nabla^2 + V(\mathbf{r},t)\right]\psi(\mathbf{r},t), \tag{2.1}$$

where the time-dependent potential $V(\mathbf{r},t)$ is the sum of the atomic potential $V_{atomic}(\mathbf{r})$ and the dipole interaction with the laser electric field $e\mathbf{r}\cdot\mathbf{E(t)}$ [15, 16], where $\mathbf{E}(t) = \hat{\mathbf{e}}Ecos(\omega t+\psi)$ is the oscillating electric field vector of the laser. The exact solution of this equation can be written in integral form,

$$\psi(\mathbf{r},t_f) = e^{\left\{\int_{t_i}^{t_f}\frac{dt}{i\hbar}\left[-\frac{\hbar^2}{2m}\nabla^2 + V(\mathbf{r},t)\right]\right\}}\psi(\mathbf{r},t_i), \tag{2.2}$$

where t_i and t_f are the initial and final time.

To solve this equation numerically, we split the operator with a small time step Δt to eliminate the time dependence of potential during each time step. We then integrate by parts,

$$\psi(\mathbf{r},t_f) \qquad = \exp\left\{\sum_{n=0}^{N-1}\frac{\Delta t}{i\hbar}\left[-\frac{\hbar^2}{2m}\nabla^2 + V(\mathbf{r},n\Delta t)\right]\right\}\psi(\mathbf{r},t_i)$$

$$= \left\{ \prod_{n=0}^{N-1} \exp\left\{ \frac{\Delta t}{i\hbar}\left[-\frac{\hbar^2}{2m}\nabla^2 + V(\mathbf{r}, n\Delta t)\right]\right\}\right\} \psi(\mathbf{r}, t_i), \tag{2.3}$$

Using the identity of the Fourier transform, we obtain

$$\begin{aligned} e^{\left\{\frac{\Delta t}{i\hbar}\left[-\frac{\hbar^2}{2m}\nabla^2+V(\mathbf{r},t+\Delta t)\right]\right\}}\psi(\mathbf{r},t) &= \mathcal{F}^{-1}\mathcal{F}e^{\left\{\frac{\Delta t}{i\hbar}\left[-\frac{\hbar^2}{2m}\nabla^2+V(\mathbf{r},t+\Delta t)\right]\right\}}\psi(\mathbf{r},t) \\ &= \mathcal{F}^{-1}\left\{e^{-\frac{\Delta t}{i\hbar}\frac{p^2}{2m}}\mathcal{F}\left[e^{\frac{\Delta t V(\mathbf{r},t+\Delta t)}{i\hbar}}\psi(\mathbf{r},t)\right]\right\}. \end{aligned} \tag{2.4}$$

In this way, the propagation of the wave function in time can be calculated by the iterative Fourier transform between real and momentum spaces. If the temporal step length and spatial grid size are small enough, the numerical solution of the TDSE can be very accurate.

Once the time-dependent electronic wave function is known, the power spectrum of HHG can be calculated through the Fourier transform of the dipole acceleration (second order derivative of the time-dependent dipole moment). The calculation of the HHG amplitude in the length, velocity and acceleration gauges is shown in Eqn. 2.5.

$$\begin{aligned} S(\Omega) \quad &= \mathcal{F}\left\{\frac{d^2}{dt^2}\left\langle\psi(\mathbf{r},\mathbf{t})\left|\mathbf{r}\right|\psi(\mathbf{r},\mathbf{t})\right\rangle\right\} = \Omega^4\mathcal{F}\left\{\left\langle\psi(\mathbf{r},\mathbf{t})\left|\mathbf{r}\right|\psi(\mathbf{r},\mathbf{t})\right\rangle\right\} \\ &= \mathcal{F}\left\{\frac{d}{dt}\left\langle\psi(\mathbf{r},\mathbf{t})\left|\mathbf{v}\right|\psi(\mathbf{r},\mathbf{t})\right\rangle\right\} = \Omega^2\mathcal{F}\left\{\left\langle\psi(\mathbf{r},\mathbf{t})\left|\mathbf{v}\right|\psi(\mathbf{r},\mathbf{t})\right\rangle\right\} \\ &= \mathcal{F}\left\{\left\langle\psi(\mathbf{r},\mathbf{t})\left|\mathbf{a}\right|\psi(\mathbf{r},\mathbf{t})\right\rangle\right\} \end{aligned} \tag{2.5}$$

As an example, the wave function evolution of a hydrogen atom in a strong laser field is shown in Fig. 2.1. An 800 nm laser pulse with a peak focused intensity of 3×10^{14} W/cm^2 is used in the 2-dimensional TDSE calculation. In principle, given the wave function $\psi(\mathbf{r},\mathbf{t})$ solved using the TDSE, these three gauges should give the same results. However, if approximations are used when the wave function is solved, the result will depend on the gauge used.

Although the TDSE can be solved in the case hydrogen atom, it requires considerable computational time. Even for helium atoms or hydrogen molecular ions, a

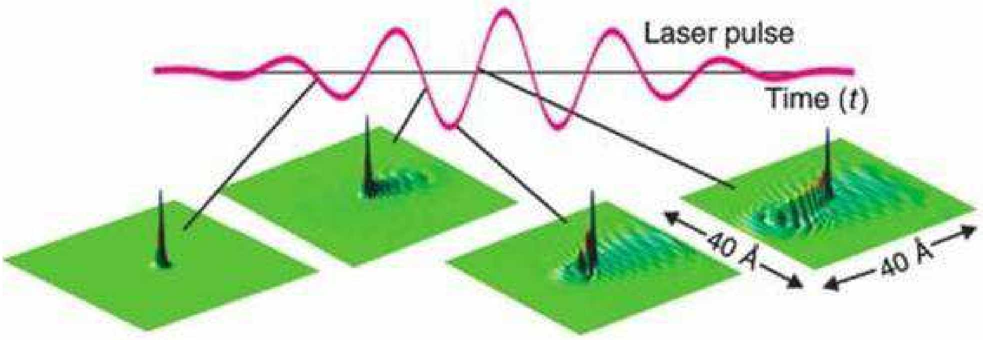

Figure 2.1: This figure shows how the wave function of a hydrogen atom evolves with time in a strong infrared laser field. Before the pulse arrives, the wave function is localized or bound. As the electric field becomes stronger, the electron density starts to tunnel through the barrier and to spread in space. The oscillation of the electron density shows the wave nature of the electron.

full calculation (including three spatial dimensions and the temporal dimension) is still considered state-of-the-art. Thus the TDSE is intractable for multielectron atoms. To simulate multielectron atoms with TDSE, we can consider a single active electron under an effective Hartree-Fock potential. Calculations have been carried out for Xe and Ne atoms [15, 16].

2.1 Three step model

For more complex atoms or molecules, it is harder to construct a potential function to exactly simulate the energy and wave function of electrons. Fortunately, a simple semiclassical three-step model [12, 13, 14] can be used to understand much of the physics of the HHG process. As we show, the three-step model and its variations offer more physical insights than solving the TDSE directly. In the three-step model of HHG, the electric field of a focused laser first ionizes an outer valence electron from the ground state of an atom or molecule. This electron is then accelerated by the electric field of the laser. If it returns to the vicinity of the parent ion, the electron can recombine into the ground state. This continuum-bound transition converts the kinetic energy of the electron into an extreme ultraviolet (EUV) photon.

2.1.1 Ionization

In the intensity regime above 10^{14} W/cm^2 , ionization is the dominant process and the starting point for consequent physical processes. In 1965, Keldysh published a classical paper [17], where he gave a unified picture of nonlinear ionization by both low and high frequency lasers. The Keldysh theory identifies two limiting cases of strong field ionization— tunnel and multiphoton ionization—distinguished by the so-called Keldysh adiabatic parameter. The Keldysh parameter depends on three quantities: the ionization potential I_p of the atom, the laser frequency ω, and the electric field strength

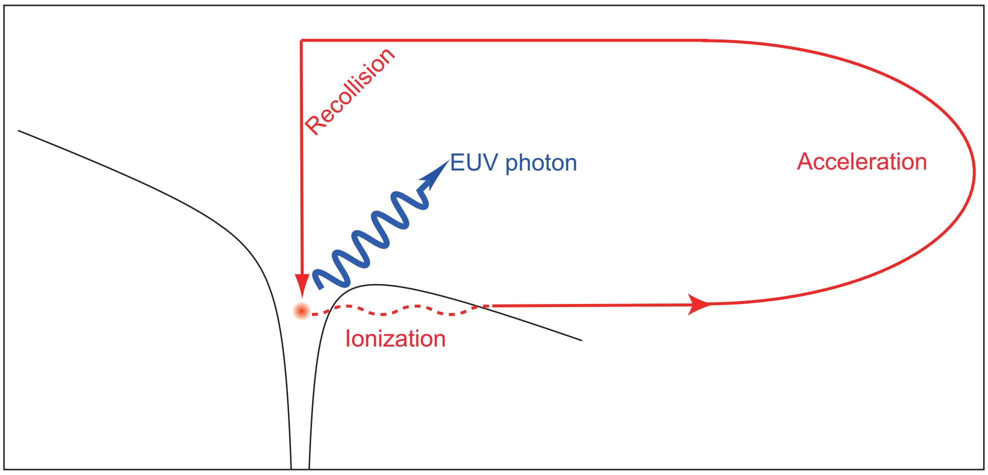

Figure 2.2: Schematic of the classical three-step model of HHG, including ionization, acceleration, and recollision steps.

E. The Keldysh parameter can be defined as

$$\gamma = \frac{\omega\sqrt{2mI_P}}{eE} = \sqrt{\frac{2I_p}{U_p}} = \frac{T_{tunnel}}{T_{optical}}, \tag{2.6}$$

where e and m are the charge and mass of electron, $U_p = \dfrac{e^2E^2}{4m\omega^2}$ is the average kinetic energy of the electron in the oscillating electric field, and $T_{ionization} = 2\pi\dfrac{\sqrt{2m_eI_p}}{eE}$ is the ionization time the electron takes to tunnel through the barrier.

At high laser frequency, when $\gamma \gg 1$, multiphoton ionization, as shown in Fig. 2.3(a) is the dominant process. This process is well described by perturbation theory. The ionization rate is proportional to E^{2q}, where q is the order of the nonlinear process. In the multiphoton ionization regime, there is insufficient time for the electron to tunnel through the barrier during each laser cycle. The electron is bounced back and forth by the oscillating potential until it absorbs enough photons to become a free electron.

For $\omega \to 0$, $\gamma \ll 1$ and $T_{tunnel} \ll T_{optical}$, the ionization can be seen as quasi-static. The electron has enough time to tunnel through the barrier in one laser cycle, as shown in Fig. 2.3(b). This is called the tunnelling limit.

For certain atomic species, the Keldysh parameter depends on both the strength of the electric field and the frequency of the laser, which is plotted in Fig. 2.4. We can see that, at the intensity of 10^{14}W/cm^2, the Keldysh parameter is around 1. Thus we are in the intermediate region between tunnel and multiphoton ionization.

When the electric field becomes even stronger, the maximum of the potential barrier becomes significantly lower than I_p, and the ionization becomes above-barrier as shown in Fig. 2.3 (c). Above-barrier ionization for hydrogen atoms occurs at 1.5×10^{14}W/cm^2, according to simple calculations. The practical threshold for above-barrier ionization is usually higher than this value due to quantum mechanical effects.

The Keldysh theory was generalized to calculate the tunnel ionization probability of an arbitrary electronic state of an atom or ion in 1986 (the ADK theory) [18],

$$w(t) = A_{n^*l^*}B_{l,|m|}I_p(\frac{2(2I_p)^{3/2}}{E(t)})^{2n^*-|m|-1}\exp(-\frac{2(2I_p)^{3/2}}{3E(t)})$$

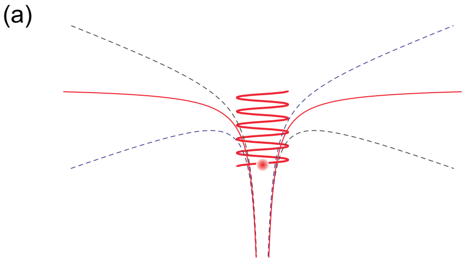

Multi-photon ionization

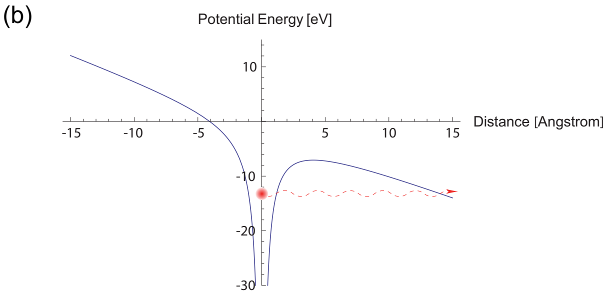

Tunnel ionization

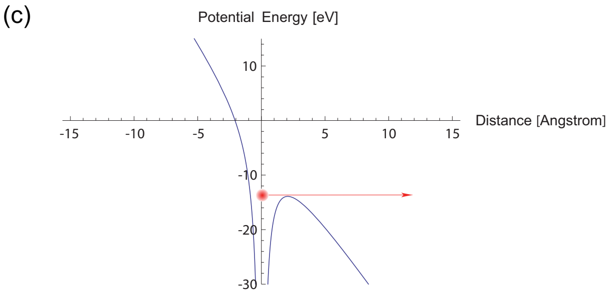

Above barrier ionization

Figure 2.3: (a) In the multiphoton ionization regime, there is insufficient time for the electron to tunnel through the barrier during each laser cycle, and the electron is bounced back and forth by the time-dependent potential. (b) and (c) While in the tunnel and above-barrier regime, ionization can be considered as quasistatic.

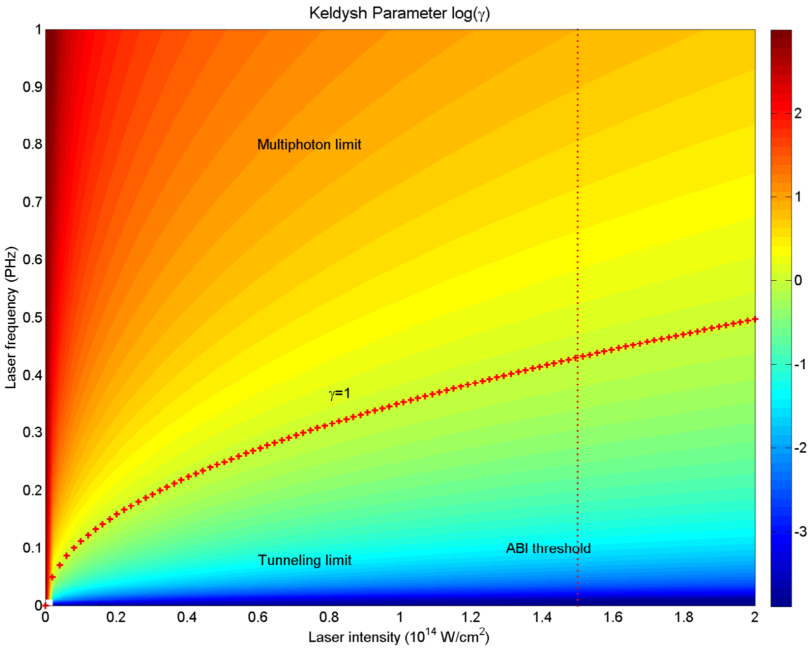

Figure 2.4: The dependence of the Keldysh parameter on the intensity and frequency of the ionization laser radiation.

where $E(t)$ is the instantaneous electric field amplitude, I_p is t the ionization potential and

$$A_{n^*l^*} = \frac{2^{2n^*}}{n^*\Gamma(n^*+l^*+1)\Gamma(n^*-l^*)}$$

and

$$B_{l,|m|} = \frac{(2l+1)(l+|m|)!}{2^{|m|}|m|!(l-|m|)!}$$

are defined by the angular quantum number l and the magnetic quantum number m of the electron. We can calculate the total ionization rate by integrating the instantaneous ionization probability over the laser pulse duration. ADK theory has been shown to be relatively accurate for calculating the instantaneous ionization rate for noble gases in the $\gamma \approx 1$ regime.

2.1.2 Acceleration

After ionization, the electron oscillates in the electric field under the influence of Coulomb forces of the nucleus. In the strong field and low frequency regime, the effect of the nuclear Coulomb force on the ionized electron can be neglected; this is referred to as the strong field approximation (SFA). Depending on the phase in the laser cycle that the electron is ionized, it is possible that the electron will reverse its direction and return to the core. A simple calculation shows that for a $\cos(\omega t)$ waveform, the electron ionized in the phase regime $[0,\pi/2]$ and $[\pi,3\pi/2]$ will return to the core, while the electron ionized at any other phases of the cycle will not return. The electrons ionized at $\approx \pi/10$ after the field peak will gain the maximum kinetic energy $3.2U_p$ when it returns to the core. We plot the return time and return kinetic energy for electrons ionized at different phases of the laser cycle in Fig. 2.5. As we can see from Fig. 2.5, if the return kinetic energy of the electron is less than $3.2U_p$, two electron trajectories will be associated with this kinetic energy. For the long trajectory the electron is ionized before $\pi/10$ and spends more time in the continuum. For the short trajectory, the electron is ionized after $\pi/10$ and spends less time in the continuum.

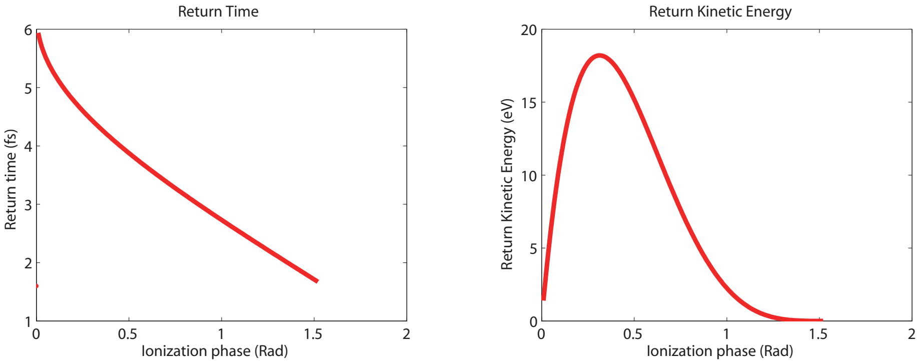

Figure 2.5: The classical calculation of return time and kinetic energy of the electrons ionized at different phases of a laser pulse with intensity of 10^{14} W/cm^2.

2.1.3 Recombination

Recombination of the photoelectron to the parent ion will generate one high energy photon. The frequencies of the generated photons correspond to odd-order harmonics of the incident laser light. The maximum kinetic energy I_p+3.2 U_p of the return electron defines the cutoff energy of HHG as shown in Fig. 2.6, which agrees surprisingly well with the experimental result of HHG from noble gases [19].

The three-step model can also explain other processes in the strong laser fields. The elastic scattering of electrons will contribute to the process referred to as high-order above-threshold ionization (ATI), because more photons than necessary are absorbed to ionize the electron, and the extra photons are converted into kinetic energy of the electron. In the last process, non-sequential double ionization (NSDI), the inelastic recollision of the photoelectron to the parent ion will kick out another electron and generate a doubly charged ion.

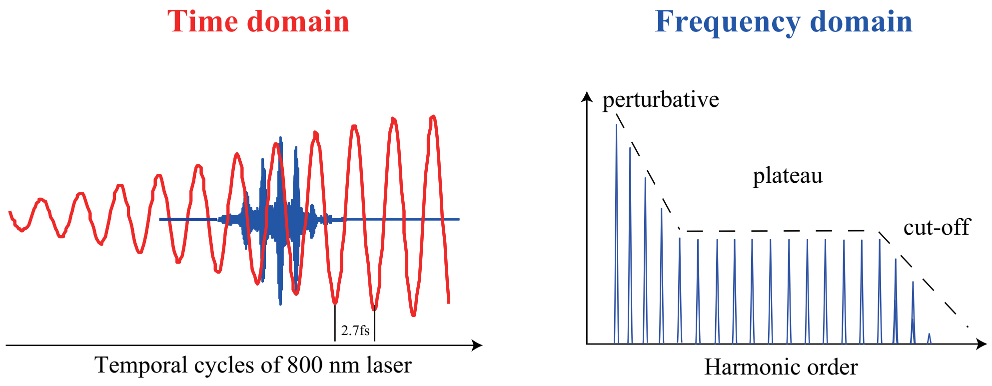

Figure 2.6: Typical HHG in time and frequency domains.

2.2 The Lewenstein model and strong field approximation

An elegant semiclassical quantum model of HHG has been developed in which the classical model has been embedded [10]. For the linearly polarized monochromatic light, the Hamiltonian in the length gauge can be written as $H = H_0(t) + V_L(t) = H_0 + xE\cos\omega t$, assuming $\hat{\mathbf{x}}$ is the polarization direction (note that we use atomic units ($e = m = \hbar = 1$) throughout this section). An exact solution of this equation can be written as

$$\begin{aligned} |\psi(t)\rangle \quad &= -i\int_0^t d\tau \left\{ \left[e^{-i\int_\tau^t \hat{H}(t')dt'} \right] V_L(\tau) \left[e^{-i\int_0^\tau \hat{H}_0(t')dt'} \right] |g\rangle \right\} \\ &\qquad + e^{-i\int_0^t \hat{H}_0(t')dt'} \, |g\rangle \, . \end{aligned} \tag{2.7}$$

Assuming H_0 is the field-free Hamiltonian, and plugging in $H_0 |g\rangle = -I_p |g\rangle$, we obtain

$$|\psi(t)\rangle = -i\int_0^t d\tau \left\{ \left[e^{-i\int_\tau^t \hat{H}(t')dt'} \right] V_L(\tau) \left[e^{-i(-I_p\tau)} \right] |g\rangle \right\} + e^{e^{-i(-I_p t)}} \, |g\rangle \, . \tag{2.8}$$

A natural explanation of this expression is that the electron is ionized at time τ. Before this time the electron evolved in the ground state; after that time the motion of the electron is governed by the total Hamiltonian. With the following two assumptions

(1) All atomic states except the ground state and continuum states labeled by the momentum $|\mathbf{v}\rangle$ are ignored.

(2) The depletion of the ground state is neglected.

The continuum part of the wave function can be expanded with the free electron wave function,

$$|\psi(t)\rangle = e^{+iI_pt}|g\rangle + \int d^3\mathbf{v}b(\mathbf{v},t)|\mathbf{v}\rangle,$$

where the expansion coefficient $b(\mathbf{v},t)$ can be given by

$$b(\mathbf{v},t) = \langle\mathbf{v}|\psi(t)\rangle = -i\int_0^t d\tau\left\{\langle\mathbf{v}|\left[e^{-i\int_\tau^t \hat{H}(t')dt'}\right]V_L(\tau)\left[e^{-i(-I_p\tau)}\right]|g\rangle\right\}.$$

Under SFA, $e^{-i\int_\tau^t \hat{H}(t')dt'}$ can be replaced by $e^{-i\int_\tau^t \hat{H}_F(t')dt'}$. The free electron Volkov propagator then becomes

$$\begin{aligned}\langle\mathbf{v}|e^{-i\int_\tau^t \hat{H}(t')dt'} &= \langle\mathbf{v}|e^{-i\int_\tau^t \hat{H}_F(t')dt'} = \langle\mathbf{v}|e^{i\int_\tau^t \hat{H}_F(t')dt'}\\ &= \langle\mathbf{v}(\tau)|e^{i\int_\tau^t KE(t')dt'} = e^{-i\int_\tau^t KE(t')dt'}\langle\mathbf{v}(\tau)|\end{aligned} \tag{2.9}$$

Thus the expansion coefficient $b(\mathbf{v},t)$ can be given by

$$\langle\mathbf{v}|\psi(t)\rangle = -i\int_0^t d\tau\left\{e^{-i\int_\tau^t KE(t')dt'}\langle\mathbf{v}(\tau)|V_L(\tau)|g\rangle e^{+iI_p\tau}\right\} \tag{2.10}$$

where $KE(t)$ is the free electron kinetic energy.

According to the dipole approximation $\mathbf{E}(t) = -\frac{\partial\mathbf{A}(t)}{\partial t}$, the momentum change of the electron in the electric field is

$$\int_\tau^t e\mathbf{E}(t)dt' = -\int_\tau^t e\frac{\partial\mathbf{A}(t)}{\partial t}dt' = -e\left[\mathbf{A}(t) - \mathbf{A}(\tau)\right] = m(\mathbf{v} - \mathbf{v}(\tau)).$$

We can now introduce the new conserved quantity, canonical momentum

$$\mathbf{p} = \mathbf{v} + \mathbf{A}(t) = \mathbf{v}(\tau) + \mathbf{A}(\tau).$$

So the electron kinetic energy can be expressed as

$$KE(t) = \frac{1}{2}\mathbf{v}(t)^2 = \frac{1}{2}\left(\mathbf{v}(\tau) + \mathbf{A}(\tau) - \mathbf{A}(t)\right)^2 = \frac{1}{2}\left(\mathbf{p} - \mathbf{A}(t)\right)^2.$$

Plugging in $V_L(\tau) = xE\cos(\omega\tau)$, the wave function can be written as

$$\begin{aligned} b(\mathbf{v}(t),t) \quad &= -i\int_0^t d\tau E\cos(\omega\tau)\left\{e^{-i\int_\tau^t dt'\frac{1}{2}[\mathbf{p}-\mathbf{A}(\mathbf{t'})]^2}\left\langle\mathbf{v}(\tau)\right|x\left|g\right\rangle e^{+iI_p\tau}\right\} \\ &= -i\int_0^t d\tau E\cos(\omega\tau)\left\{e^{-i\int_\tau^t dt'\frac{1}{2}[\mathbf{p}-\mathbf{A}(\mathbf{t'})]^2}d_x(\mathbf{p}-\mathbf{A}(\tau))e^{+iI_p\tau}\right\}, \end{aligned} \tag{2.11}$$

where $d_x(\mathbf{p}-\mathbf{A}(\tau)) = \left\langle\mathbf{v}(\tau)\right|x\left|g\right\rangle$.

We then calculate the dipole moment by neglecting the continuum-continuum transition

$$\begin{aligned} x(t) = \left\langle\psi(t)\right|x\left|\psi(t)\right\rangle = \int d^3\mathbf{v}d_x^*(\mathbf{v})b(\mathbf{v},t) + c.c. \\ = i\int_0^t d\tau\int d^3\mathbf{p}E\cos(\omega\tau)d_x^*(\mathbf{p}-\mathbf{A}(t))e^{-iS(\mathbf{p},t,\tau)}d_x(\mathbf{p}-\mathbf{A}(\tau)) + c.c. \end{aligned} \tag{2.12}$$

where the classical action $S(\mathbf{p},t,\tau)$ is defined as $\int_\tau^t dt'\left\{\frac{1}{2}\left[\mathbf{p}-A(t')\right]^2 + I_p\right\}$. The dipole term $d_x(\mathbf{p}-\mathbf{A}(\tau))$ describes the transition between the ground state and continuum state at ionization. The dipole term $d_x^*(\mathbf{p}-\mathbf{A}(t))$ is the recombination dipole between the continuum state and the ground state. Then $e^{-iS(\mathbf{p},t,\tau)}$ gives the phase accumulated by the electron when it is accelerated in the continuum, which is referred to as the intrinsic phase of the HHG.

The Fourier transform of the dipole acceleration is the amplitude of the HHG:

$$S(\Omega = q\omega) = \int \ddot{x}(t)e^{-i\Omega t}dt = -\Omega^2\int x(t)e^{-i\Omega t}dt$$

Due to the sinusoidal oscillation of the electric field and the central symmetry of the atomic potential, $x(t)$ can be expanded a as Fourier series, $x(t) = \sum\limits_K x_{2K+1}e^{i(2K+1)\omega t}$, with the coefficients defined as

$$\begin{aligned} &x_{2K+1} = \int_0^{2\pi} dtx(t)e^{i(2K+1)\omega t} \\ &= i\int_0^{2\pi} dt\int_0^t d\tau\int d^3\mathbf{p}E\cos(\omega\tau)d_x^*(\mathbf{p}-\mathbf{A}(t))e^{-iS(\mathbf{p},t,\tau)+(2K+1)i\omega t}d_x(\mathbf{p}-\mathbf{A}(\tau)) \\ &+c.c. \end{aligned} \tag{2.13}$$

Then $[(2K+1)\omega]^2x_{2K+1}$ is the amplitude of the $q = (2K+1)$ order harmonic.

This integral can be evaluated by the stationary phase (saddle point) approximation, and the stationary phase conditions for each of these three integrals are shown below,

(1) For $\mathbf{p}$, $\nabla_{\mathbf{p}} S(\mathbf{p}, t, \tau) = x(t) - x(\tau) = 0$

(2) For τ , $\dfrac{\partial S(\mathbf{p}, t, \tau)}{\partial \tau} = \dfrac{\partial}{\partial \tau} \displaystyle\int_{\tau}^{t} dt' \left\{ \frac{1}{2} \left[\mathbf{p} - \mathbf{A}(\mathbf{t'})\right]^2 + I_p \right\} = \frac{1}{2} \left[\mathbf{p}(\tau) - \mathbf{A}(\tau)\right]^2 + I_p = 0$

(3) For t , $\dfrac{\partial S(\mathbf{p}, t, \tau)}{\partial t} = \dfrac{1}{2} \left[\mathbf{p} - \mathbf{A}(t)\right]^2 - \dfrac{1}{2} \left[\mathbf{p} - \mathbf{A}(\tau)\right]^2 + I_p = (2K + 1)\omega$

These three conditions correspond elegantly to the assumptions made in the classical method. Condition (1) means that the electron should return to the vicinity of the parent ion. Condition (2) corresponds to the zero initial velocity after ionization, assuming $\frac{1}{2} \left[\mathbf{p}(\tau) - \mathbf{A}(\tau)\right]^2 = -I_p \ll U_p$. Condition (3) is simply energy conservation. The saddle point method reveals that the most important contribution to HHG is from the "quantum trajectories" which are close to the classical motion of the electron. This is a result of the quantum interference of all quantum paths, and is similar to the Feynman path integral.

Eqn. 2.12 can be easily generalized to a laser field with an arbitrary polarization direction,

$$\begin{aligned} \mathbf{D}(t) &= \langle \psi(t) | \, \mathbf{r} \, | \psi(t) \rangle = \int d^3\mathbf{v} d_x^*(\mathbf{v}) b(\mathbf{v}, t) + c.c. \\ &= i \int_0^t d\tau \int d^3\mathbf{p} \cos(\omega\tau) \mathbf{d}^*(\mathbf{p} - \mathbf{A}(t)) e^{-iS(\mathbf{p}, t, \tau)} [\mathbf{E} \cdot \mathbf{d}(\mathbf{p} - \mathbf{A}(\tau))] + c.c. \end{aligned} \tag{2.14}$$

2.3 Applications of HHG and propagation effects

According to the thee-step model, the recollision process repeats each half laser cycle, generating a burst of EUV radiation. In the time domain, this forms a pulse train synchronized with the fundamental laser, as shown in Fig. 2.6. Since the EUV burst is confined to each half laser cycle, the pulse duration of each burst is in the attosecond regime. In the spectral domain, this corresponds to a comb with a spacing twice the fundamental laser frequency. An intense IR pulse with a well controlled waveform can confine the EUV radiation to only one half cycle, and thus is able to generate a single attosecond pulse. This highly coherent radiation in the soft X-ray spectrum with attosecond pulse structure has been recognized as an important tool for time resolved spectroscopy. Both the single attosecond pulse generated with a few-cycle IR pulse and the attosecond pulse train generated with a multi-cycle IR pulse have been experimentally characterized and applied to a few proof of principle applications [20].

Even without the attosecond time resolution, HHG is still a very good university-lab-scale alternative to synchrotron sources. HHG sources are especially good for experiments which require short temporal resolution and modest pulse energy, such as photoelectron spectroscopy of gases or solid surfaces.

The most important barrier for attosecond science as an emerging field is the low flux that can be generated particularly at shorter wavelengths. To further enhance the conversion efficiency from fundamental laser to HHG, it is important to understand the propagation of the fundamental laser and HHG in the generation medium, especially the phase mismatch $\Delta k = q\mathbf{k}_\omega - \mathbf{K}_\Omega$. Similar to the case of low order harmonic generation, the phase velocity difference between HHG and the fundamental infrared light will limit the effective interaction length to the coherence length $L_c = \pi/\Delta k$. Four terms contribute to the phase mismatch Δk,

(1) The index of refraction difference between the fundamental laser and HHG in a neutral gas $\Delta k = -q\frac{2\pi}{\lambda_0}(1-\eta)(n_q - n)$, where $n_q - n$ represents the index of refraction difference between the qth harmonic and the fundamental laser, λ_0 is the wavelength of the fundamental laser, and η is the ionization level that can be calculated by the ADK formula.

(2) The index of refraction difference between fundamental laser and HHG in a plasma (free electron) $\frac{N_a \eta e^2 \lambda_0}{mc^2} \frac{q^2-1}{q}$, where N_a is the density of the gas.

(3) The geometric phase of the fundamental laser due to the propagation or focusing geometry. For a free space focus, the Gouy phase shift can be written as $q \arctan(z/b)$, where z is the longitudinal coordinate and b is the confocal parameter. Since $\Delta\Phi = \int \Delta k dz = \int (\mathbf{K}_\Omega - q\mathbf{k}_\omega) dz$, the gradient of $\Delta\Phi$ gives Δk. For a fiber, the geometric term is written as $\Delta k = \frac{U_{nm}^2 \lambda_0}{4\pi a^2} \frac{q^2-1}{q}$, where U_{nm} is related to the propagation mode in the fiber. The q factor comes from the fact that the cycle time of the fundamental is q times the cycle time of the HHG.

(4) The intensity dependent intrinsic phase, as we mentioned in our discussion of the Lewenstein model. This term depends on the harmonic order and laser intensity distribution.

The relative importance of these terms depends on the geometry of HHG. In the gas jet geometry, a Gaussian laser beam is focused into a thin gas jet. The intensity dependent atomic phase and the Gouy phase are dominant terms. Since the intrinsic phase of long and short trajectories differ in intensity dependence, the short trajectories can only be phase-matched on axis when focused before the gas jet, while the long trajectories can only be phase matched on axis when focused after the gas jet [21].

For harmonic generation in a fiber [22], there is no Gouy phase shift. Thus the index of refraction difference between the fundamental and HHG in the neutral gas and electron plasma are dominant terms. Tuning the gas pressure can fully phase-match a range of harmonics in a hollow fiber. This method offers more harmonic flux and better coherence than the HHG produced from a gas jet. The spatial intensity distribution in the transverse direction will confine the phase matching region to mainly near the axis, thus reducing the HHG beam size. These properties make the HHG in a hollow fiber available as a source for microscopy and high resolution imaging [23].

Chapter 3

High-Order Harmonic Generation from Molecules—Experiments and Theoretical Models

In contrast to atoms, molecules have more complicated electronic structure and involve rotational and vibrational freedom. Molecular orbital theory mathematically describes the electronic wave function of a molecule by a superposition of atomic orbitals (basis sets). Sophisticated quantum chemistry code implements self-consistent field calculations (methods) to calculate the coefficients of atomic orbital components.

These calculations can predict various properties of molecules, such as optimized molecular geometry (bond length and bond angle), vibrational frequency, energy, wave function, permanent dipole moment, and polarizability of certain electronic states. In Fig. 3.1, we list electronic wave functions of the highest occupied molecular orbitals (HOMO) for several linear diatomic and triatomic molecules used in this work. Also in table 3.1, we list the HOMO symmetry, the ionization energy, and the bond length of these molecules. People generally rely on quantum chemistry calculations to understand the structure and dynamics of small gas-phase molecules. The accuracy of the calculated electronic wave function can be verified by indirect experimental measurements, such as vibrational frequency and the energy level of electronic states. However a direct measurement of the electron wave function is always preferable.

The density distributions of the electrons and the positions of the nuclei can be obtained by hard X-ray diffraction [24]. However, large samples with crystallized

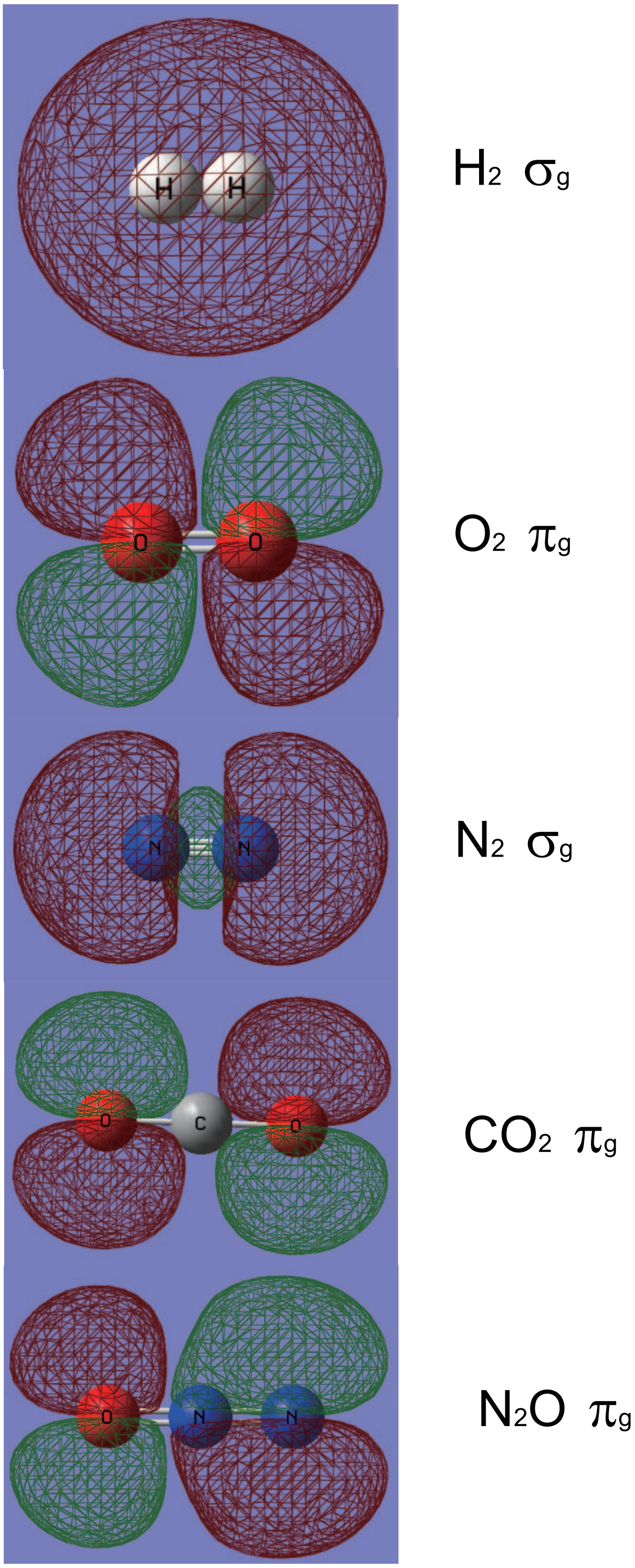

Figure 3.1: HOMO electron wave function for several linear diatomic and triatomic molecules used in this work. the Hartree-Fock single point energy calculation was done with the 6-31G basis set.

structure are needed for these experiments. The X-ray pulse durations from synchrotron sources are usually longer than a few ps, thus offering poor time resolution.

Table 3.1: The HOMO symmetry, ionization energy, and bond length for several linear diatomic and triatomic molecules used in this work.

Molecule	HOMO symmetry	I_p	Bond length
H_2	σ_g	15.43	0.741 Å
D_2	σ_g	15.47	0.742 Å
O_2	π_g	12.03	1.208 Å
N_2	σ_g	15.58	1.098 Å
CO_2	π_g	13.78	C-O:1.16 Å
N_2O	π_g	12.89	N-N:1.186 Å N-O: 1.126Å

Strong field processes such as ionization and HHG are assumed to be sensitive to molecular structure, especially to the electron wave function of the HOMO. The suppression of ionization in O_2 molecules compared to Xe has been explained as the interference of two electron sites [25]. By fitting the wave function of molecules in the asymptotic area with a single center atomic wave function, ADK theory has been generalized to molecules. With this theory, the angularly dependent ionization has been predicted [26].

Since the development of molecular alignment techniques, there has been increased interest in studying high harmonic generation (HHG) from field-free rotationally aligned molecules or vibrating molecules. Using a simple analogy, an atom or molecule driven by a strong laser field behaves like an antenna—the radiated field will depend on the shape of the antenna, which in the case of HHG is the shape and orientation of the molecular electronic wave function or molecular orbital. Thus important information about the atoms and molecules is encoded on the properties of the HHG emission.

The motivation to study HHG from molecules is two-fold. Firstly, once we understand the HHG processes in molecules, coherent control of the generated EUV radiation might become possible by manipulating molecular emitters. Secondly but more importantly, recent experiments (as reviewed later) enable the possibility of imaging molecular structure and dynamics with HHG. Monitoring the structure change in real time offers the opportunity to understand the correlation between structure and dynamics, since the dynamics of the molecules is determined by their transient structure. The evolution from unstable transient structure to stable structure is important to a chemical reaction. Thus the ability to record the electronic wave function changes during a chemical reaction is valuable. HHG has the intrinsically short time resolution, and as will be discussed in the following, it can offer certain structural information as well. These two characteristics allow HHG to give structural and dynamical information simultaneously.

Recently developed time-resolved photoion-photoelectron spectroscopy and imaging techniques can monitor the electron or ion momentum in real time. Combining these with coincidence techniques, indirect structural information can be obtained [27]. Ultrafast electron diffraction (UED) is another promising direction for gas phase molecular dynamics, but the time resolution is limited to the ps range due to the spatial charge effect, which will stretch the duration of the electron pulse [28].

3.1 Experimental Method

In this section, I briefly review the experimental setup and methodology of the molecular HHG experiments. The experimental setup, which consists of a laser system, and harmonic generation and detection chambers, is shown in Fig. 3.2.

3.1.1 Laser system

The fundamental laser light for the HHG experiment is delivered by a high-average power, 2-stage, 1 kHz repetition rate Ti:sapphire amplifier. A 100 MHz pulse train from a Kerr lens mode-locking Ti: sapphire oscillator is amplified, employing the principle of chirped pulse amplification [29, 30]. The energy of the pulse from the oscillator is

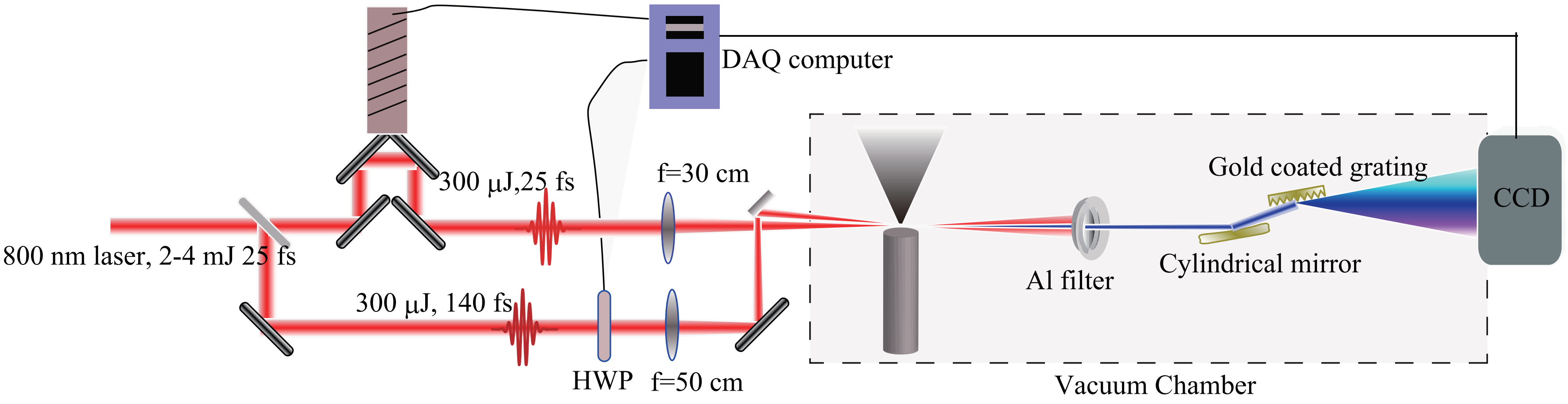

Figure 3.2: The experimental apparatus consists of four major components: a Ti:sapphire amplifier, a Mach-Zehnder interferometer, a harmonic generation chamber, and a glancing-incidence EUV spectrometer.

about 3-5 nJ, with a transform-limited pulse duration less than 20 fs. In the first stage of the amplifier system, a grating-based stretcher stretches the pulse to 20 ps and a Pockels cell can select a 1 kHz pulse train. After recollimation, the pulse is sent to the multipass amplification stage pumped by an intracavity doubled Nd:YAG laser (Falcon, Quantronix, 20 mJ pulse energy, 100 ns pulse duration). After the first stage, the pulse goes through another Pockels cell to supress the amplified stimulated emission. The pulse is further amplified in a double-pass second stage. In both stages, the Ti:Sapphire crystals are contained in cryostat vacuum cells. The copper crystal holders are cooled down to 77 K using liquid nitrogen, cooling can reduce the thermal lens in the Ti: sapphire crystals and improve the beam quality. To avoid water condensation on the crystals, both the cells are maintained under high vacuum by an ion pump. After the amplification, a compressor is used to recompress the pulse to nearly transform limited pulse duration. This amplifier is capable of generating a 25-30fs pulse with more than 5 mJ energy and a decent beam spatial profile (M^2 <1.5). We characterize the spatial profile and pulse duration using a beam profiler (Spiricon) and second harmonic generation based frequency resolved optical gating (FROG). The typical spectrum and FROG trace of the amplifier output are shown in Fig. 3.3.

A Mach-Zehnder type interferometer was used to implement the pump-probe experiments. We split the output pulse from the amplifier to pump and probe beams by a dielectric beam splitter. We vary the transmission of this beam splitter from 20% to 40%, depending on the experimental requirements. A computer-controlled, motorized translation stage is used to adjust the delay between the pump and probe beams. The energies, pulse durations and polarizations of the pump and probe pulses can be separately controlled by adding various optics, such as a wave plate or polarizer into the beam paths of pump and probe. The pump and probe pulses are focused by two anti-reflection coated lenses and recombined either collinearly or non-collinearly before the vacuum chamber The lenses are mounted on 3D translation stages to adjust

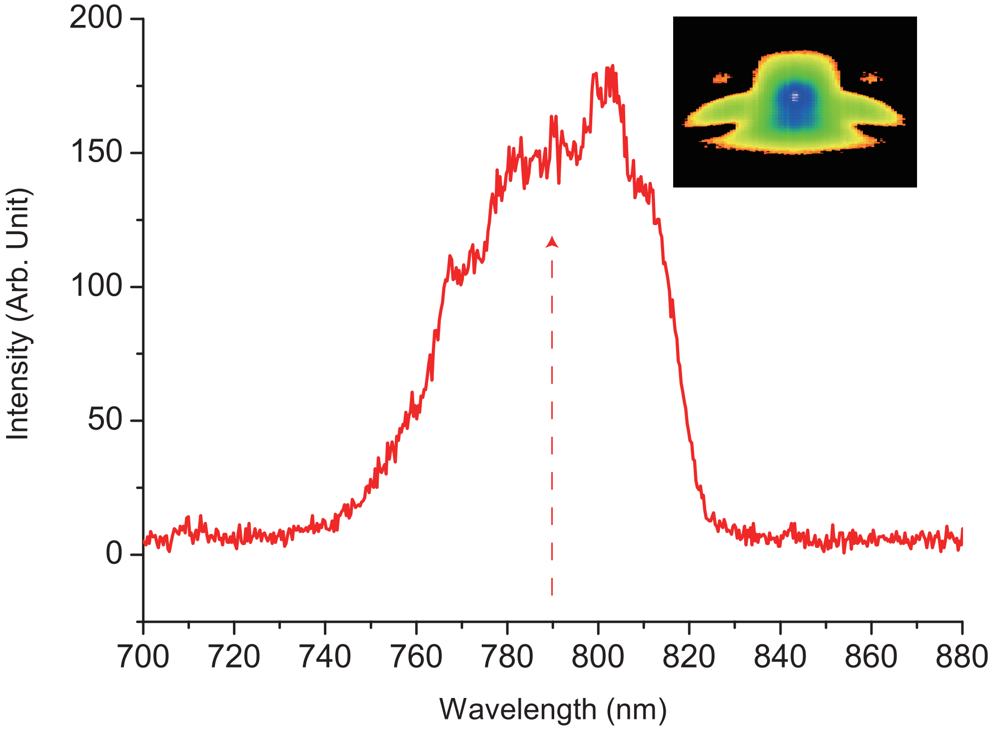

Figure 3.3: Typical spectrum and FROG trace of the amplifier output.

the focus positions. The vacuum chamber window is a 3 mm thick sapphire window in experiments presented in Chapters 3, 4 and 6.

3.1.2 Generation chamber and gas injection

The HHG chamber shown in Fig. 3.4 is equipped with a high speed 550 l/s Turbo pump. The diameter of the connection between the chamber and the pump is 6 inches to ensure maximum pumping efficiency. The atomic or molecular beam is injected into the chamber with a continuous jet made of a ∼1 cm long hollow glass fiber that has a 125 μm inner diameter and a 1.25mm outer diameter respectively. The capillary was glued to a glass tube which extends to the outside of the vacuum chamber by a feedthrough, and is connected to the gas cylinder through an UltraTorr connection. Our backing pressure is usually around 1 atmosphere and controlled by the regulator of the gas cylinder.

Supersonic cooling of the molecular beam has many applications in physics and chemistry, such as high resolution molecular optical spectroscopy and molecular reaction dynamics. The high pressure gas goes through a pinhole into a vacuum chamber. Collisions during the adiabatic expansion strongly reduce the translational energy of the atoms or molecules. Rotational cooling was achieved by the equilibration between the translational and rotational degrees of freedom, thus transferring the population to lower energy rotational states. As the expansion continues, collisions cease, and the lowest temperature is achieved.

With the help of a pulsed jet, high backing pressure, a carrier gas, and skimmers, rotational temperature less than 10K can be achieved by supersonic cooling. However, for the HHG experiments, a reasonably high gas density was needed in the interaction region to generate sufficient HHG flux. Therefore we use a continuous jet to run the experiments at the full repetition rate available from the laser, since kHz pulse valves are still not widely available. This limits the lowest rotational temperature we can achieve,

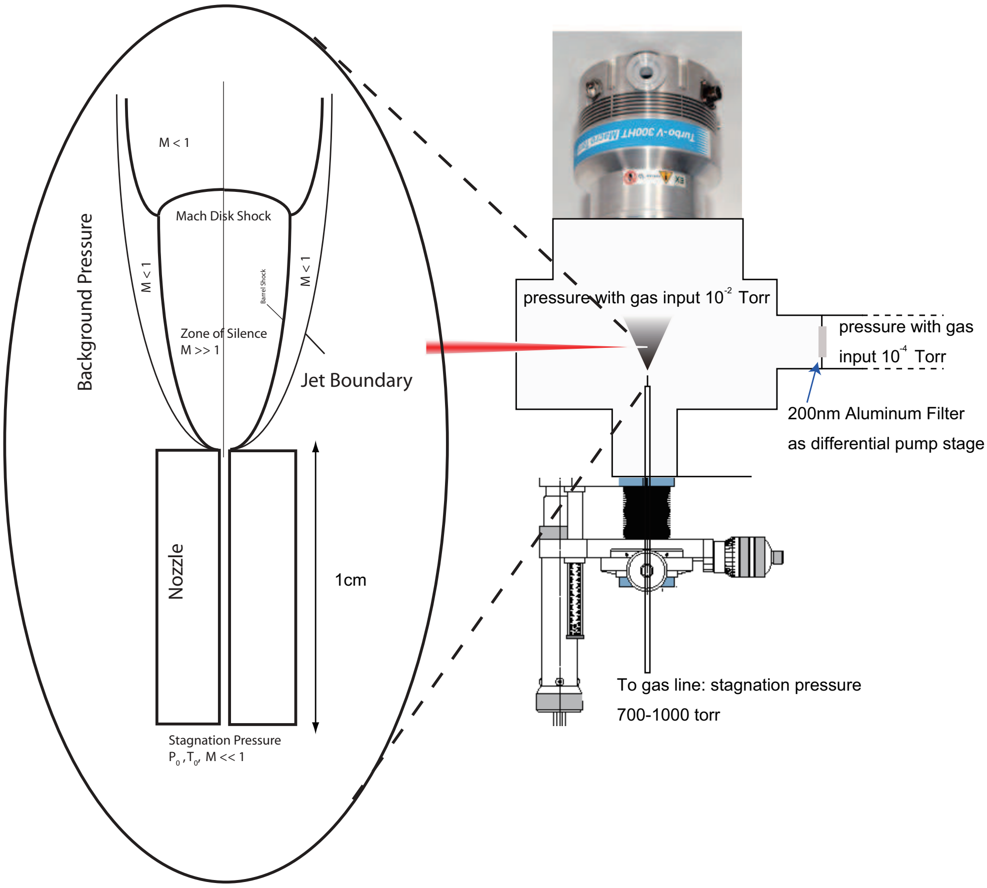

Figure 3.4: The design of the harmonic generation chamber with an illustration of the gas injection.

because we also need to keep the background pressure in the chamber low enough to avoid reabsorption of the generated EUV light.

To estimate the gas flow rate, the gas density distribution, and the rotational temperature in the interaction region, we need to know the chamber volume and the pump speed, as well as the jet parameters discussed above. We estimate that the on-axis gas density 500 μm downstream from our jet is approximately 10^{18} cm^{-3}, and the rotational temperature is approximately 100 K for CO_2 molecules. The total pass length of the gas medium is less than 1mm.

However, the error bar of this estimate is usually quite large. This is due to three factors. First, the length of the final fiber section of the jet was not accurately controlled in fabrication. Second, the distance between the laser focus and the gas jet exit was not accurately controlled in the experiments. Third, the fiber section was made of glass, and thus can be slightly damaged by the focused laser beam due to misalignment.

Due to the short pass interaction length of the jet, we ensure that the short trajectory HHG is fully phase matched —the coherence length is much longer than the medium length—by focusing the laser beam slightly before the gas jet, where the harmonic flux is also maximized. This is very important to our experiments, because the macroscopic HHG is proportional to the HHG from a single atom or molecule only under the phase-matching condition.

In addition to phase matching issues, other macroscopic effects, such as plasma defocusing and self phase modulation of the fundamental pulse can afftect the HHG. Again, due to the short interaction length in our gas jet, we usually neglect these effects.

3.1.3 Imaging of the focus

For our experiments, the spatial profile is important for estimating the laser intensity at the focus. We built an imaging system to measure the beam profile in-situ. We placed a removable steering mirror 15 cm from the gas jet along the optical beam propagation direction to reflect the beam out of the vacuum chamber.. The beam then goes through a 40-cm focal length imaging lens and two intensity attenuators, and is finally detected by a web cam at the image plane. We image the beam profile at the gas jet position. Although the beam focus is slightly before the gas jet, we can a very good estimation of the focused beam size and profile.

3.1.4 Detection of the HHG light

The generated harmonics pass through two 200 nm thick aluminum filters to reject the fundamental laser light. The transmission curve of this filter is shown in Fig. 3.5 (c). The HHG beam is then spectrally dispersed using an EUV spectrometer (containing a grazing incidence cylindrical gold mirror and EUV grating, made by Hettrick Scientific) and finally detected using an EUV charge-coupled device (CCD) camera. We used a back-illuminated CCD camera from Andor Technology with a spatial resolution of 1024×256. A typical experimental harmonic image recorded by the CCD is shown in Fig. 3.5 (a). The image on the CCD has line structures due to the 1D focus of the cylindrical gold mirror. In the fully vertical bin mode of the camera, the photon counts can be electronically integrated along the short camera dimension (256 pixels). A typical HHG spectrum from CO_2, along with the transmission curve of the aluminum filter, are shown in Figs. 3.5 (b) and (c). In practice, the transmission of the aluminum filter will decrease with time due to oxidation on its surface.

3.1.5 Data acquisition and analysis

Processing of raw spectral data from the CCD starts with subtracting a background from the raw spectrum. The background includes two parts, the dark noise of the CCD camera (which is dominant), and the scattered HHG and remaining fundamental photons. Following background subtraction, the harmonic intensity was integrated among the pixels that see significant flux. The wavelength scale are calibrated by the the

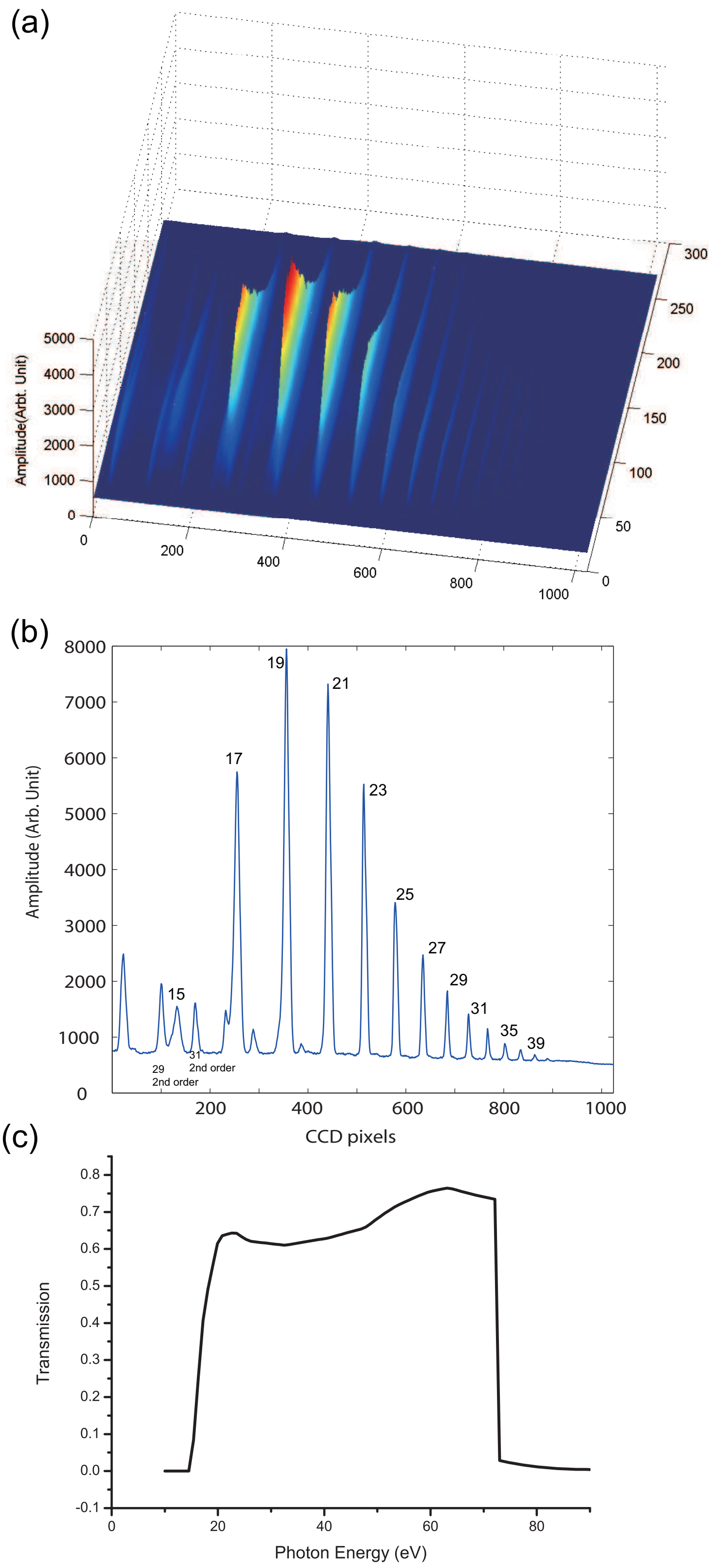

Figure 3.5: (a) and (b) Typical 2D image and fully vertical binned spectrum of the HHG from CO_2 taken by the CCD camera. (c) Transmission of a 200 nm aluminum filter.

aluminum absorption edge at 72.4 eV and further confirmed by identifying the position of the second order diffraction of the grating.

3.2 Nonadiabatic molecular alignment

In our experiments, a ∼100 fs pump pulse is used to align the molecules, this duration is much shorter than the rotational period of the molecules used (usually tens of ps). This allows us to align the molecular sample in the non-adiabatic alignment regime. Note that the intensity of our pump pulse is below 6×10^{13} W/cm^2, so ionization of the sample can safely be ignored.

3.2.1 The interaction Hamiltonian

The alignment of the molecules can be understood through the torques created by the electric field interacting with the induced dipole $\tau = \mathbf{p} \times \mathbf{E}$, where $\mathbf{p} = \alpha \cdot \mathbf{E}$ is the induced dipole. However, a classical model cannot fully characterize rotational revivals, due to the quantized nature of rotation levels. Each rotational eigenstate, $|JM\rangle$, has an energy $BJ(J+1)$, where B is the rotational constant of the molecule, and is inversely related to the moment of inertia: $B = \dfrac{\hbar^2}{2I}$. The field-dressed pendular states are govern by the time-dependent Schrödinger equation (TDSE). We start by deriving the Hamiltonian $H = H_0 + H_L$ for a linear molecule in an optical field. The molecule interacts with light through the dipole operator.

$$H_L = -\mu \cdot \mathbf{E} - \frac{1}{2}\mathbf{p} \cdot \mathbf{E}, \tag{3.1}$$

where μ is the permanent dipole of the molecule. The electric field is a cosine oscillation $\mathbf{E}(t) = \hat{\mathbf{e}}a(t)cos(\omega t + \psi)$, where $a(t)$ is the pulse envelope. We note that the interaction related to the permanent dipole will be averaged out and will not contribute to the potential energy.

In the molecular frame, the polarizability tensor α can be written as

$$\alpha = \begin{pmatrix} \alpha_\perp & 0 & 0 \\ 0 & \alpha_\perp & 0 \\ 0 & 0 & \alpha_\parallel \end{pmatrix} \tag{3.2}$$

where $\alpha_\parallel$ and $\alpha_\perp$ are the polarizability along and perpendicular to the molecular axis, $\Delta\alpha = \alpha_\parallel - \alpha_\perp$ is the difference between them, and the angle θ is the angle between the laser polarization and the molecular axis. Thus the interaction term can be written as:

$$-\frac{1}{2}E^2(t)\left(\alpha_\parallel \cos^2\theta + \alpha_\perp \sin^2\theta\right) = -\frac{1}{2}E^2(t)\left(\Delta\alpha \cos^2\theta + \alpha_\perp\right). \tag{3.3}$$

Since the second term is not angle-dependent, we neglect it for convenience. Averaging over the laser oscillation, the first term can be written as:

$$-\frac{1}{4}a^2(t)\Delta\alpha\cos^2\theta \tag{3.4}$$

The field-free Hamiltonian is $B\mathbf{J}^2$, so the total Hamiltonian can be written as:

$$H = B\mathbf{J}^2 - \frac{1}{4}a^2(t)\Delta\alpha\cos^2\theta \tag{3.5}$$

The rotational constant B and the anisotropic polarizability $\Delta\alpha$ for simple molecules can be found at [31]. We list a few example molecules in Table 3.2.

Table 3.2: The rotational constant, rotational period, and anisotropic polarizability for several common molecules

Molecule	Rotational Constant, B	Rotation period (ps)	anisotropic polarizability, $\Delta\alpha$
H_2	60.853 cm^{-1}	0.274	0.288 Å^3
N_2	1.99 cm^{-1}	8.383	0.7 Å^3
O_2	1.43 cm^{-1}	11.666	1.1 Å^3
CO_2	0.39 cm^{-1}	42.699	2.1 Å^3
N_2O	0.43 cm^{-1}	39.805	2.8 Å^3

3.2.2 Solving the TDSE

The rotational wave functions $|JM\rangle$ are mathematically equal to spherical harmonic functions. The matrix element $\langle JM\,|H|\,J'M'\rangle$ between two rotational states $|JM\rangle$ and $|J'M'\rangle$, is mostly zero, except for $J = J'$ or $J = J' \pm 2$ and $M = M'$. Thus the matrix form of the time-dependent Schrödinger equation can be simplified to a series of differential equations. Each equation corresponds to a specific $|JM\rangle$ state.

As we mentioned in the experimental section, we estimate the rotational temperature at the interaction region is about 100K. At this temperature, only the rotational states of the molecules with $J_i < 40$ can be thermally excited. The population is distributed among the rotational states according to the Boltzmann distribution. Neglecting the rotational states for $J_i > 40$, the initial state of the molecular ensemble can be described by a density matrix:

$$\frac{1}{Q_{rot}}\sum_{J_i=0}^{J_{i,\max}} w_{J_i} e^{-iE_{J_i}/kT} \sum_{M_i=-J_i}^{J_i} |J_iM_i\rangle\,\langle J_iM_i|$$

where the rotational partition function can be written as:

$$Q_{rot} = \sum_{J_i=0}^{J_{i,\max}} w_{J_i}(2J_i+1)e^{-iE_{J_i}/kT}, \tag{3.6}$$

where the factor w_{J_i} are related to the nuclear spin statistics.

We can propagate this initial state density matrix under the Liouville equation. Equivalently we can also assume the initial state is a pure $|J_iM_i\rangle$ state. We then calculate the time evolution of this pure state by solving the TDSE . Finally when the expectation value of an observable operator is calculated, an incoherent thermal average is needed. Thus, the final state after excitation for the initial state $|J_iM_i\rangle$ can be expressed as a coherent rotational wave packet in terms of the rotational eigenstates $|JM\rangle$ with complex coefficients, $C_{JM,J_iM_i}(t)$, and energy-dependent phase accumulation:

$$\psi_{J_iM_i}(t) = \sum_{J,M} C_{JM,J_iM_i}(t)e^{-iE_Jt/\hbar}\,|JM\rangle = \sum_{J,M} C_{JM,J_iM_i}(t)e^{-iBJ(J+1)t/\hbar}\,|JM\rangle \tag{3.7}$$

3.2.3 The expectation value and thermal averaging over initial states

We can calculate the expectation value of operator $\hat{O}$ by $\langle \psi_{J_i M_i}(t) | \hat{O} | \psi_{J_i M_i}(t) \rangle$. The typical operators used to characterize the molecular alignment are the angular density $\langle \psi(t) | \psi(t) \rangle$ and the expectation values of $\cos^2\theta$ and $\sin^2 2\theta$. These values are calculated for each initial state, and then added incoherently, weighted by the thermal populations:

$$\frac{1}{Q_{rot}} \sum_{J_i=0}^{J_{i,\max}} w_{J_i} e^{-iE_{J_i}/kT} \sum_{M_i=-J_i}^{J_i} \langle \psi_{J_i M_i}(t) | O | \psi_{J_i M_i}(t) \rangle \tag{3.8}$$

The rotational wave function $|JM\rangle$ can be represented by the spherical harmonics $Y_{lm}(\theta, \phi)$, and the integration of this is trivial. A C++ code solving this TDSE and calculate different expectation values was developed by Dr. Andreas Wüest and Robynne Lock [32].

We are particularly interested in the angular density $\rho(\theta, \phi, t)$, here:

$$\int_0^{\pi} d\theta \int_0^{2\pi} d\varphi \rho(\theta, \varphi, t) \sin\theta = 1$$

Due to the rotational symmetry around the aligning laser, $\rho(\theta, \phi, t)$ is independent of the azimuth angle Φ. We can define a new function $\rho(\theta, t)$ to represent the time-dependent angular distribution:

$$\rho(\theta, t) = 2\pi \rho(\theta, \varphi, t) \sin\theta,$$

here $\int_0^{\pi} d\theta \rho(\theta, t) = 1$.

We note from our experiments that a good balance of the pump pulse intensity and duration can improve the alignment. We found the optimum pulse duration and intensity for alignment is approximately 100 fs and a few times 10^{13} W/cm^2.

3.2.4 Periodical revivals after time zero

Figs. 3.6 and 3.7 present the molecular alignment for CO_2 and N_2 molecules, characterized by the angular distribution $\langle \psi(t) | \psi(t) \rangle$ and the expectation values of $\cos^2\theta$

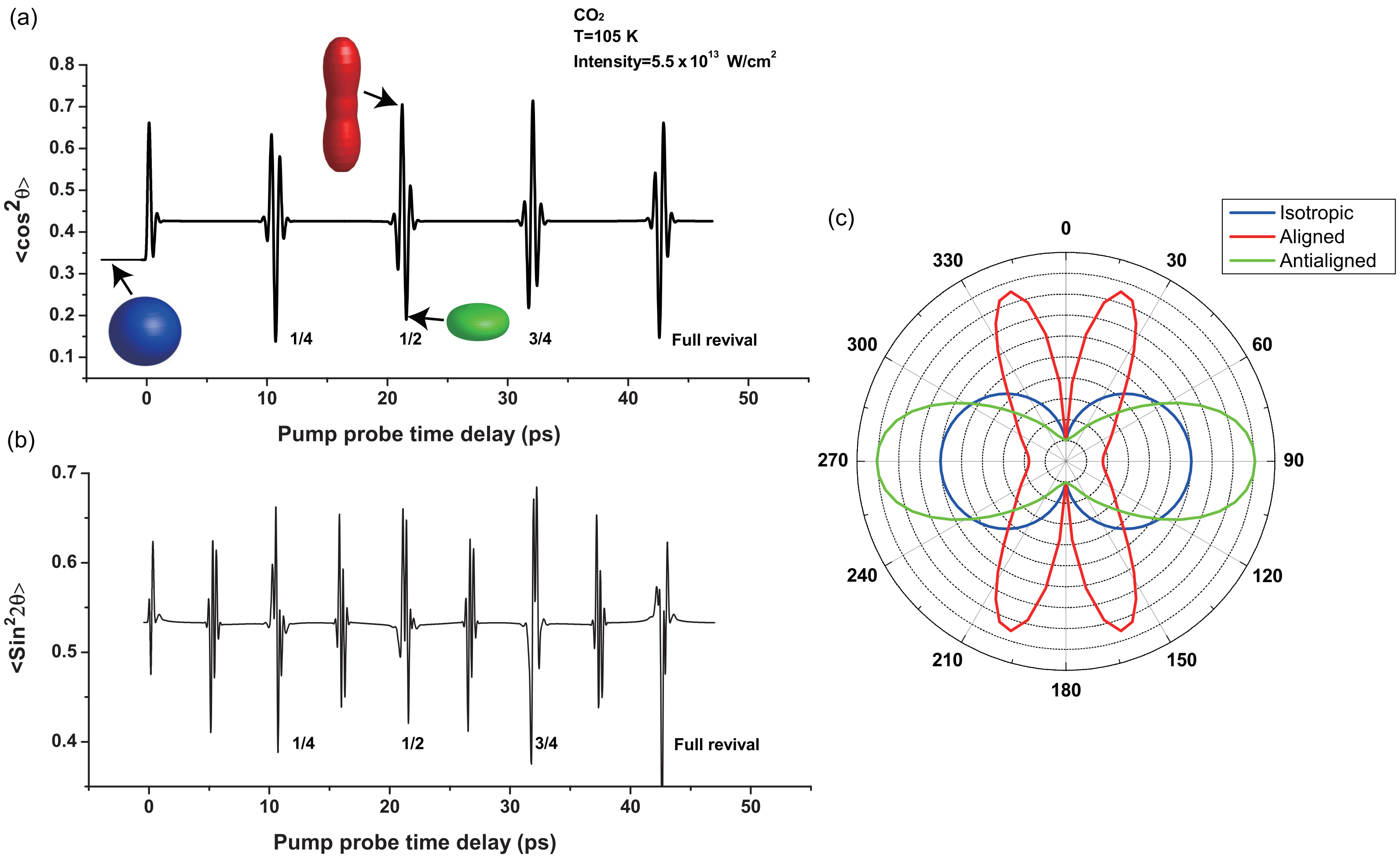

Figure 3.6: This figure shows (a) $\langle \cos^2\theta \rangle$ and (b) $\langle \sin^2 2\theta \rangle$ of CO_2 during a rotational period and (c) the angular distribution $\rho(\theta, t)$ for isotropic molecules and strongly aligned and antialigned molecules during half revival.

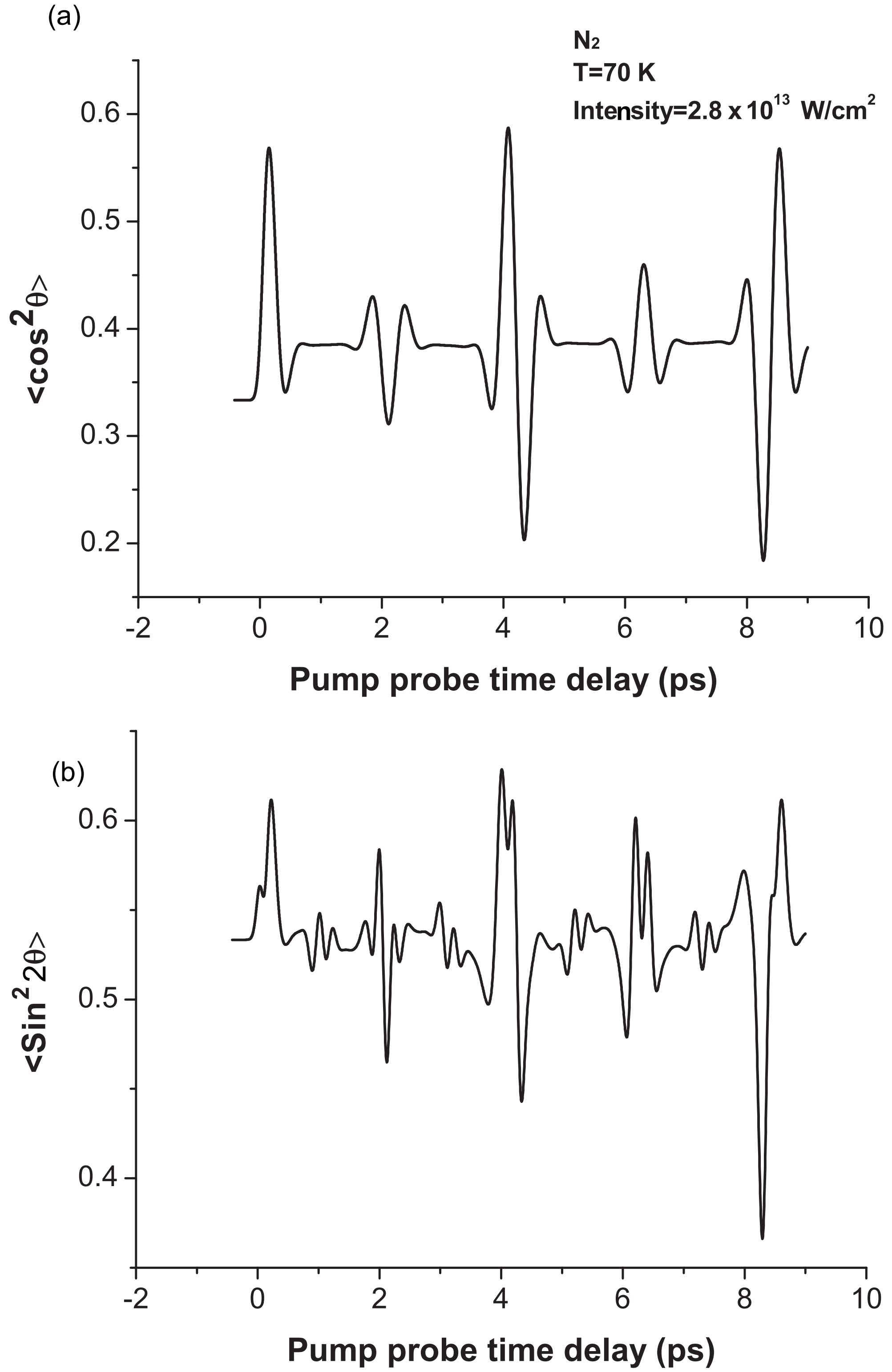

Figure 3.7: This figure shows (a) $\langle \cos^2\theta \rangle$ and (b) $\langle \sin^2 2\theta \rangle$of N_2 during a full rotational period .

and $\sin^2 2\theta$. We confirm, by numerical simulation, that experimental angular distributions are not critically dependent on parameters such as rotational temperature or laser intensity.

At certain time delays after the pump pulse, the excited wave packet will rephase to form a revival. The reason for this periodic behavior is that the wave packet is composed of rotational eigenstates with discrete energies $BJ(J+1)\hbar$. Under field free conditions, the Hamiltonian is independent of time, therefore, the coefficients $C_{JM,J_iM_i}(t)$ are independent of time. The evolution of the wave packet comes from the different phase accumulation of rotation levels of different eigenenergies. Consider a time delay $T = \dfrac{\pi\hbar}{B}$, the phase of each state changes by $\pi J(J+1)$, which is a multiple of 2π for all positive values of J. This means the wave packet at this time (and multiples of this time) repeats the wave packet at $t = 0$. The time $T = \dfrac{\pi\hbar}{B}$, is called the full revival time. There are fractional revivals at fractions of the revival time T (i.e. $1/2, 1/4, 1/8, \ldots$), during which only a portion of the states are in phase. Some of these revivals are not shown in alignment parameters $\langle\cos^2\theta\rangle$ or $\langle\sin^2 2\theta\rangle$, they can only be seen from the time dependent angular distribution $\rho(\theta, t)$.

3.3 HHG from aligned molecules

3.3.1 Coherent buildup of HHG

Replacing the ground state of an atom with the HOMO of certain molecules, we can generalize the Lewenstein model for the case of HHG from molecules.

$$\begin{aligned}\mathbf{D}(t) &= \langle\psi(t)|\,\mathbf{r}\,|\psi(t)\rangle = \int d^3\mathbf{v} d_x^*(\mathbf{v}) b(\mathbf{v},t) + c.c. \\ &= i\int_0^t d\tau \int d^3\mathbf{p}\cos(\omega\tau)\mathbf{d}^*(\mathbf{p}-\mathbf{A}(t))e^{-iS(\mathbf{p},t,\tau)}[\mathbf{E}\cdot\mathbf{d}(\mathbf{p}-\mathbf{A}(\tau))] + c.c. \quad (3.9)\end{aligned}$$

This model has been used to calculate the angular dependence of HHG [33, 34, 35]. In the Lewenstein model, the ionization is characterized as the transition dipole $d(\mathbf{p}-\mathbf{A}(\tau))$

between the ground state and the continuum state, which is different from the ionization rate calculated with the molecular ADK theory.

We can calculate the HHG amplitude $S(\Omega, \theta)$ through the Fourier transform of the time-dependent dipole. Assuming the molecular angle does not change on the time scale of the ultrashort pump pulse, the total harmonic intensity can be written as an convolution of the single-molecule HHG amplitude with the angular distribution:

$$S_A(\Omega, t) = \int_0^{2\pi} \rho(\theta, t) S(\Omega, \theta) d\theta \tag{3.10}$$

This equation is rigorously proved in ref. [36], using the density matrix formula.

3.3.2 Tomography of the molecular orbital

In the integral of the Lewenstein model (Eqn. 3.9), the information about the molecular structure is contained in the dipole term $d^*(\mathbf{p} - \mathbf{A}(t))d(\mathbf{p} - \mathbf{A}(\tau))$. A very general method for probing molecular structure using HHG was demonstrated recently by using a tomographic technique to reconstruct the N_2 molecular orbital [37]. Basically, the return electron wave packet in the HHG process is considered to be a plane wave, and from this it is assumed that the HHG intensity can be characterized by the angle-dependent ionization $N(\theta)$, the return electron wave packet $a(k(\Omega))$ and the recombination dipole between the plane wave and the HOMO.

Under the single active electron approximation the recombination process is a continuum to bound (HOMO) transition. For harmonics with frequency $\Omega = n\hbar\omega$, the return electron wave packet can be written as $|\psi_c(t)\rangle = \sum_{\Omega} a(k(\Omega)) e^{ik(\Omega)x - i\Omega t}$, where $a(k(\Omega))$ is the complex amplitude of the return electron wave packet and the transition dipole between the continuum wave function $\psi_c(t)$and the ground state HOMO ψ_g can be written as:

$$\mathbf{d_L}(\mathbf{t}, \theta) \qquad = \langle \psi_g(\mathbf{r}, \theta) | \, \mathbf{r} \, | \psi_c(t) \rangle$$

$$
\begin{aligned}
&= \sum_{\Omega} a(k(\Omega)) \langle \psi_g(\mathbf{r},\theta) | \, \mathbf{r} \left| e^{ik(\Omega)x} \right\rangle e^{-i\Omega t} \\
&= \int a(k(\Omega)) \langle \psi_g(\mathbf{r},\theta) | \, \mathbf{r} \left| e^{ik(\Omega)x} \right\rangle e^{-i\Omega t} d\Omega \\
&= \int a(k(\Omega)) \mathbf{d}_L(\Omega,\theta) e^{-i\Omega t} d\Omega, \qquad (3.11)
\end{aligned}
$$

where θ is the angle between the driving laser polarization and the molecular axis. From this, we can derive the following definition which relates the dipole moment to the 3D Fourier transform of the molecular orbital: $\langle \psi_g(\mathbf{r},\theta) | \, \mathbf{r} \left| e^{ik(\Omega)x} \right\rangle = \mathbf{d}_L(\Omega,\theta)$. In length gauge this can be expressed as:

$$
\begin{aligned}
S(\Omega,\theta) \quad &= |H(\Omega)|^2 = \left| \mathcal{F}\left[\ddot{\mathbf{d}}_L(t,\theta) \right] \right|^2 \\
&= \Omega^4 \left| \mathcal{F}\left[\mathbf{d}_L(t,\theta) \right] \right|^2 |a(k(\Omega))|^2 \\
&= \Omega^4 |a(k(\Omega))|^2 |\mathbf{d}_L(\omega,\theta)|^2 ; \qquad (3.12)
\end{aligned}
$$

and in velocity gauge this can be expressed as:

$$
\langle \psi_g(\mathbf{r},\theta) | \, \mathbf{v} \left| e^{ik(\Omega)x} \right\rangle = \mathbf{d}_V(t,\theta),
$$

and

$$
S(\Omega) = \Omega^2 |a(k(\Omega))|^2 |\mathbf{d}_V(\Omega,\theta)|^2 ;
$$

in acceleration gauge this can be expressed as:

$$
\langle \psi_{\mathrm{g}}(\mathbf{r},\theta) | \, \mathbf{a} \left| e^{ik(\Omega)x} \right\rangle = \mathbf{d}_A(t,\theta),
$$

and

$$
S(\Omega) = |a(k(\Omega))|^2 |\mathbf{d}_A(\Omega,\theta)|^2 .
$$

According to the three-step model, the harmonic power spectrum generated from aligned molecules not only depends on the recombination dipole, but also on the angle-dependent ionization. With this considered, we can rewrite the harmonic power spectrum as [37]:

$$
HHG(\Omega,\theta) = |S(\Omega,\theta)|^2 = N(\theta)\Omega^4 |a(k(\Omega))|^2 |\mathbf{d}_L(\Omega,\theta)|^2 \qquad (3.13)
$$

where $N(\theta)$ is proportional to the angle-dependent ionization rate. A few assumptions and arguments need to be made to extract the wave function:

(1) It is assumed that for each pump/probe angle θ, the intensity $HHG_{N_2}(\Omega,\theta)$ from a perfectly aligned molecule is measured. The convolution with the angular distribution is neglected. The perpendicularly polarized HHG component when the pump and probe pulse polarization are not perpendicular or parallel to each other is also neglected.

(2) Since Ar atoms and N_2 molecules have similar I_p [37], it is assumed that the recolliding electron wave packets are the same for Ar and N_2, thus the HHG spectrum from Ar can serve as a reference.

(3) A phase jump occurs at the 23rd harmonic, based on the fact that there is a spectral minimum in the normalized HHG spectrum of N_2.

(4) For nitrogen molecules, the angularly dependent ionization and the spatial spreading of the electron wave packet can compensate for each other; thus both can be ignored.

Based on these arguments and assumptions, the following relation can be obtained:

$$\mathbf{d}_{N_2}(\Omega,\theta)=\frac{S_{N_2}(\Omega,\theta)}{S_{Ar}(\Omega)}\mathbf{d}_{Ar}=\frac{\sqrt{HHG_{N_2}(\Omega,\theta)}e^{i\phi_r}}{\sqrt{HHG_{Ar}(\Omega)}}\mathbf{d}_{Ar},$$

where ϕ_r is the relative phase between the emission dipole of N_2 and Ar. Since $\mathbf{d}_{N_2}(\Omega,\theta)=\langle\psi_g(\mathbf{r},\theta)|\,\mathbf{r}\left|e^{ik(\Omega)x}\right\rangle$, the Fourier slice theorem can be used to tomographically reconstruct the HOMO of the molecules from the HHG measurement at 19 different angles θ, similarly to how images are reconstructed in medical tomography.

The significance of this experiment lies in the fact that, since the return electron has a wavelength comparable to the molecular dimension, and since HHG can be considered as the interference of the plane wave continuum electron with the ground state, molecular information is encoded in the HHG properties.

3.4 Recent theoretical advances

As we have shown, the three-step model is central to our understanding of HHG from molecules. However, a few important approximations have been made in this model, compared with the case of a full quantum calculation.

First, the single active electron approximation does not include the multi-electron effects such as the indistinguishability of electrons and spin statistics [38, 39].

Second, the correlation between the continuum and bound electron during both the ionization and electron propagation are not considered. For a rigid molecule, such as N_2, the Koopmans' approximation is valid, which means the cation has the exact same N-1 electron wave function as the neutral. This also means that the I_p of the molecules is the energy level of the HOMO electron. However this is not true for molecules with large polarizability.

Third, since the ionization rate is exponentially related to the ionization potential, for atoms the outer-most electrons are much easier to ionize than the lower lying states, In this case, it is safe to consider only the highest orbital during the strong field process. Thus single ionization channel is assumed, which means the electron being ionized is always from the HOMO. This is equivalent to the statement that only the ground state of the cation is accessed as shown in Fig. 3.8. This approximation does not apply for molecules with closely lying cation states.

Finally and more importantly, in the sense of the strong field approximation (SFA), the influence of the Coulomb potential on the recolliding electron is not considered [40]— an electronic plane wave was used to represent the recolliding electron. Furthermore, at the recollision, the molecules were assumed to be at field free condition.

The various approximations listed above have motivated intense theoretical efforts to extend the 3-step model beyond the SFA and SAEA [13, 14, 16]. However, the validity of these new and more sophisticated theories needs to be compared carefully

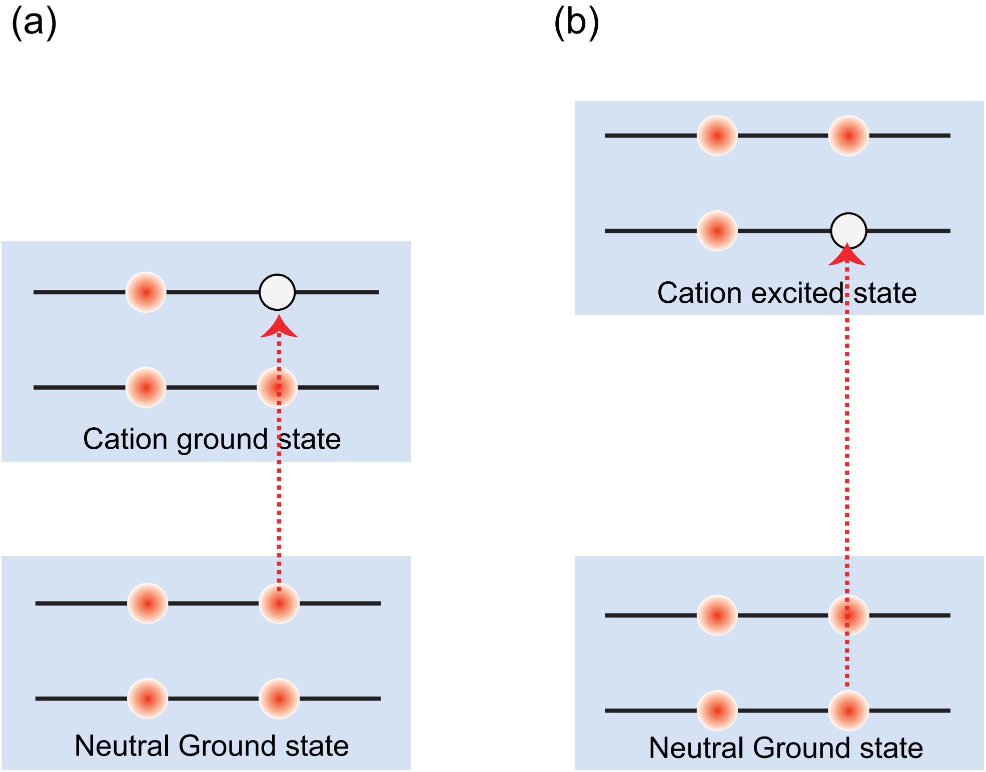

Figure 3.8: The schematics for tunnel ionization from HOMO to cation ground state (a) and from HOMO-1 to cation excited state (b).

with experiments.

3.4.1 Multielectron and multichannel ionization

To account for multielectron effects, instead of considering the dipole moment of a single electron, we can consider the dipole of a multielectron wave function:

$$D(t) = e\langle\psi(\mathbf{r}_1, ..., \mathbf{r}_N)\left|\sum_{\mathbf{i=1}}^{\mathbf{N}} \mathbf{r_i}\right|\psi(\mathbf{r}_1, ..., \mathbf{r}_N)\rangle \tag{3.14}$$

If we neglect the correlation between the continuum and bound state during the electron propagation, we can write the dipole as:

$$\psi(\mathbf{r}_1, ..., \mathbf{r}_N) = \psi_g + \psi_c = \psi_g(\mathbf{r}_1, ..., \mathbf{r}_N) + \sum_j \hat{A}\psi_{ion,j}(\mathbf{r}_1, ..., \mathbf{r}_{N-1})\psi_{c,j}(\mathbf{r}_N) \tag{3.15}$$

Where ψ_g is the N-electron ground state of the molecules and ψ_c is the N-electron state with one electron in the continuum. The anti-symmetric operator $\hat{A}$ is used to account for the indistinguishability of electrons and spin statistics. The index j labels the different ionization channels, which means that more than one cation states can be accessed by the tunnel ionization. Plugging Eqn. 3.15 into the dipole equation, we obtain,

$$D(t) = \sum_j e\langle\psi_{neutral}(\mathbf{r}_1, ..., \mathbf{r}_N)\left|\sum_{\mathbf{i=1}}^{\mathbf{N}} \mathbf{r_i}\right| A\psi_{ion,j}(\mathbf{r}_1, ..., \mathbf{r}_{N-1})\psi_{c,j}(\mathbf{r}_N)\rangle.$$

The continuum wave function can be solved by scattering method [40]. The bound wave function is represented by the Dyson orbital of different ionization channels. The Dyson orbital $\langle\psi_{neutral}(\mathbf{r}_1, ..., \mathbf{r}_N)|\psi_{ion,j}(\mathbf{r}_1, ..., \mathbf{r}_{N-1})\rangle$ is the inner product of the N-electron neutral wave function and the (N-1)-electron cation wave function. Thus, the dipole can be considered as the recombination from the continuum wave function to the Dyson orbital.

3.4.2 Recombination as an inverse process of photoionization

In a recent paper [41], based on an extension of the three-step model, it was shown that accurate HHG intensity can be expressed as

$$HHG(\Omega) = W(E_k)\,|d_R(\Omega)|^2$$

Here $W(E_k)$ describes the flux of the returning electron with energy E_k, and can be calculated by dividing the SFA calculated dipole $S_{SFA}(\Omega)$ by the plane wave recombination dipole. This was confirmed by TDSE calculations of atoms and the molecular ion H_2^+ [42]. $d_R(\Omega)$ is the exact photoionization transition dipole of the molecules ionized by a photon with energy $\hbar\Omega$. It can be derived from the differential photoionization cross section along the laser/EUV polarization [43]. Since the continuum wave function is different for the photoionization process compared with the HHG process, more work is needed to fully verify this theory.

Chapter 4

Phase and Intensity Characterization of HHG Emission from Aligned Molecules

As we discussed in the previous chapter, the continuum-bound transition in the HHG recombination process converts the kinetic energy of the electron into an EUV photon. Information about the molecular structure is encoded in the orientation-dependence of the HHG intensity.

As a simple example, the shape and symmetry of the HOMO can result in multi-center quantum interferences as the electron recombines. This is in exact analogy to the same effects long-recognized in the context of EUV photoelectron spectroscopy of molecules [44], since recombination in HHG is similar to the photoionization process.

4.1 Two-center interference in molecular HHG

Lein et al. theoretically investigated quantum interferences in HHG from hydrogen molecules by solving the time dependent Schrödinger equation (TDSE) [45, 46]. A spectral minimum was found both in the harmonic spectrum for a fixed orientation, and in the angular dependence of the harmonic intensity for given harmonic order. Furthermore, this work predicted a sudden phase jump at the spectral minimum, where the phase of the electric field of the high harmonic emission reverses. These results can be understood as interference of harmonic emission from two spatially separated atomic orbitals in a molecule as illustrated in Fig. 4.1. The evolution of HHG intensity during a full rotational period of CO_2 for harmonic order 23, 33, and 37 are shown in Fig. 4.2. We also plot the alignment parameter $\langle\cos^2\theta\rangle$ on the top of Fig. 4.2, this parameter is calculated at 105 K rotational temperature and $5.5\times10^13\mathrm{W/cm}^2$ pump pulse intensity.

The recombination dipole can be written as $S(\Omega,\theta) = \left\langle e^{i\mathbf{k}(\Omega)\cdot\mathbf{r}}\right| \hat{O}\left|\psi\right\rangle$, where $\hat{O}$ is the velocity gauge dipole operator and $|\psi\rangle$ is the molecular HOMO. If $|\psi\rangle$ can be written as $\frac{1}{2}\left[\phi(\mathbf{r}-\frac{\mathbf{R}}{\mathbf{2}}) \pm \phi(\mathbf{r}+\frac{\mathbf{R}}{\mathbf{2}})\right]$, then $S(\Omega,\theta)$ can be written as,

$$\begin{aligned}
S(\Omega,\theta) = \quad & \left\langle e^{i\mathbf{k}(\Omega)\cdot\mathbf{r}}\right| \hat{O}\left|\psi\right\rangle = \left\langle e^{i\mathbf{k}\cdot\mathbf{r}}\right| \hat{O}\left|\phi(\mathbf{r}-\frac{\mathbf{R}}{\mathbf{2}})\right\rangle \pm \left\langle e^{i\mathbf{k}\cdot\mathbf{r}}\right| \hat{O}\left|\phi(\mathbf{r}+\frac{\mathbf{R}}{\mathbf{2}})\right\rangle \frac{1}{\sqrt{2}} \\
& = \left[\int e^{-i\mathbf{k}\cdot\mathbf{r}}\hat{O}\phi(\mathbf{r}-\frac{\mathbf{R}}{\mathbf{2}})d\mathbf{r} \pm \int e^{-i\mathbf{k}\cdot\mathbf{r}}\hat{O}\phi(\mathbf{r}+\frac{\mathbf{R}}{\mathbf{2}})d\mathbf{r}\right]\frac{1}{\sqrt{2}} \\
& = \left[\int e^{-i\mathbf{k}\cdot(\mathbf{r}+\frac{\mathbf{R}}{\mathbf{2}})}\hat{O}\phi(\mathbf{r})d\mathbf{r} \pm \int e^{-i\mathbf{k}\cdot(\mathbf{r}-\frac{\mathbf{R}}{\mathbf{2}})}\hat{O}\phi(\mathbf{r})d\mathbf{r}\right]\frac{1}{\sqrt{2}} \\
& = \left[(e^{-i\mathbf{k}\cdot\frac{\mathbf{R}}{\mathbf{2}}} \pm e^{+i\mathbf{k}\cdot\frac{\mathbf{R}}{\mathbf{2}}})\int e^{-i\mathbf{k}\cdot\mathbf{r}}O\phi(\mathbf{r})d\mathbf{r}\right]\frac{1}{\sqrt{2}}. \qquad (4.1)
\end{aligned}$$

For '+' sign atomic orbital superposition,

$$\begin{aligned}
S(\Omega,\theta) = \quad & = \sqrt{2}\cos(\mathbf{k}\cdot\frac{\mathbf{R}}{\mathbf{2}})\int e^{-i\mathbf{k}\cdot\mathbf{r}}O\phi(\mathbf{r})d\mathbf{r} \\
& = \sqrt{2}\cos(\mathbf{k}\cdot\frac{\mathbf{R}}{\mathbf{2}})d(\Omega,\theta). \qquad (4.2)
\end{aligned}$$

For '-' sign atomic orbital superposition,

$$\begin{aligned}
S(\Omega,\theta) = \quad & = -\sqrt{2}i\sin(\mathbf{k}\cdot\frac{\mathbf{R}}{\mathbf{2}})\int e^{-i\mathbf{k}\cdot\mathbf{r}}O\phi(\mathbf{r})d\mathbf{r} \\
& = -\sqrt{2}i\sin(\mathbf{k}\cdot\frac{\mathbf{R}}{\mathbf{2}})d(\Omega,\theta). \qquad (4.3)
\end{aligned}$$

The two-center interference model was discovered through the simulation of H_2, which is a '+' superposition of two atomic *s* orbital. However it is relatively difficult to align (because of its small anisotropic polarizability, $\Delta\alpha = 0.288\text{Å}^3$). Furthermore the rotational period is short (274 fs for H_2) makes very short (10 fs) pulse a necessity.

CO_2 is an excellent candidate for studying harmonic phase effects because it is highly polarizable ($\Delta\alpha = 2.109\text{Å}^3$) and easy to align, The degenerate HOMO of CO_2 has a 'two-center" character similar to H_2, but it is a '-' sign superposition of carbon p_y or p_x orbital rather than '+' sign superposition of H_2.

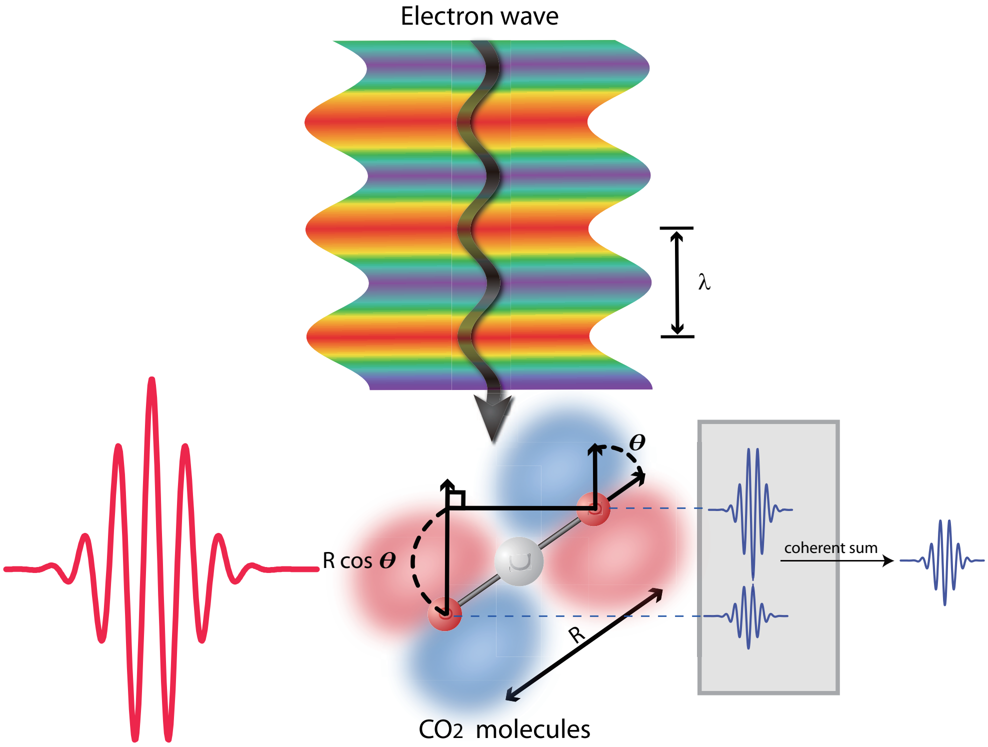

Figure 4.1: Illustration of the recolliding electron plane wave and the quantum interference of HHG in CO_2 molecules. Figure credit: Gregory J. Kuebler.

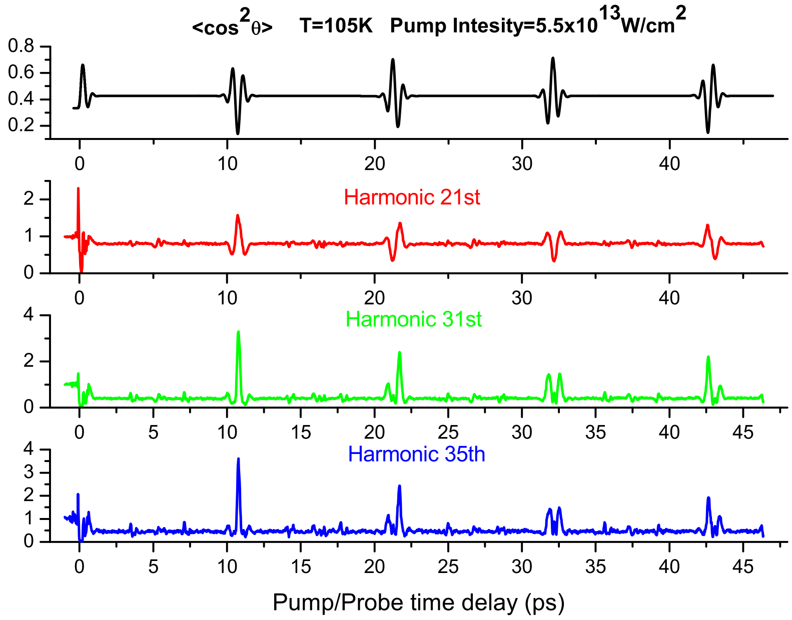

Figure 4.2: The evolution of HHG during a full rotational period of CO_2 for harmonic order 23, 33, and 37 with the alignment parameter $\langle\cos^2\theta\rangle$.

In past work, Kanai et al. and Vozzi et al. attributed the observed alignment dependence of the harmonic emission from CO_2 molecules to quantum interference [47, 48]. However, the harmonic orders most strongly modulated by alignment differed in the two experiments (the $25th$ vs the $31st$ orders, respectively). Furthermore, the authors found that different relationships between the harmonic photon energy and the recolliding electron kinetic energy, $E_k = n\hbar\omega$ or $E_k = n\hbar\omega$ - I_p, best fit their experimental data, where $n\hbar\omega$ is the harmonic energy and I_p is the molecular ionization potential. These two different relationships correspond to slightly different physical pictures—the latter corresponds to the case where the recolliding electron interacts with the HOMO and generates emission when it returns to the edge of the molecular potential, while the former implies that HHG occurs when the electron returns to the "bottom" of the molecular potential, and is thus accelerated by the Coulomb field of the molecule ion.

Other than interference, ground state depletion was also proposed as a possible mechanism for the observed modulations [49]. Therefore more accurate measurements of both the phase and intensity of HHG from aligned molecules are important, both to confirm conclusively that quantum interferences do exist in molecular HHG, and to provide insight on distortion of the recolliding wave function by the Coulomb potential of the ionized molecule. Measurement of the phase of the high harmonic emission is also critical for new approaches to molecular imaging [37]. While past experiments [50, 51] provided some evidence for phase jumps in HHG, they were inconclusive in making accurate comparisons with the two-center model.

In Fig. 4.3, we plot the prefacter $\sqrt{2}\sin(\frac{kR\cos\theta}{2})$ for CO_2 molecules. The wavelength of the returning electron wave is obtained from the relation $\lambda = \frac{\hbar}{\sqrt{2mE_k}}$ where m is the electron mass and E_k is the kinetic energy of the electron. The condition for the interference minimum is $R\cos\theta_c = \lambda$, which is a condition that is satisfied within the harmonic spectral range that is experimentally accessible. For a harmonic of

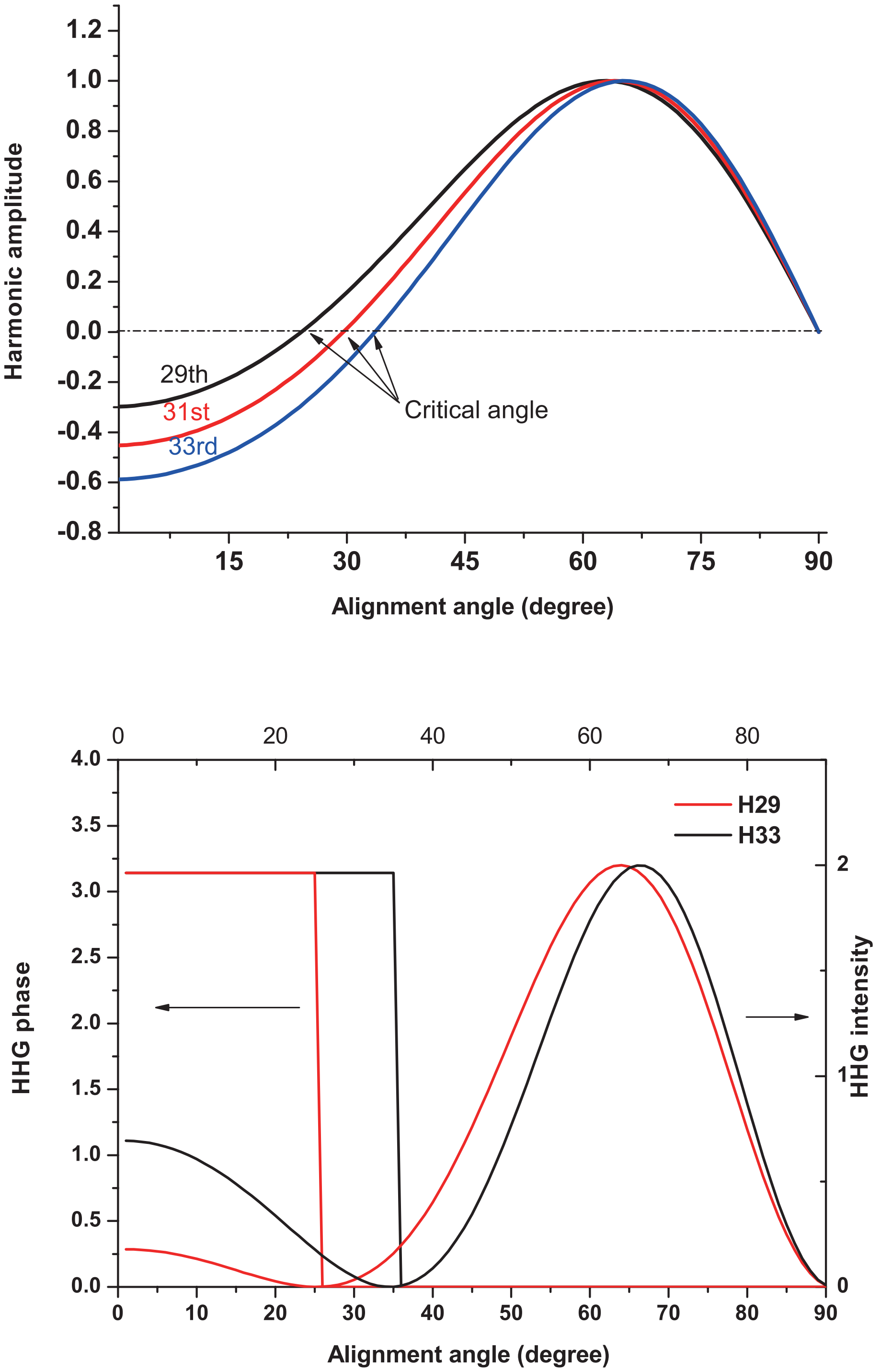

Figure 4.3: The prefacter $\sqrt{2}\sin(\frac{kR\cos\theta}{2})$ from two-center interference for CO_2 molecules.

wavelength λ, the sign of the recombination matrix element $S(\Omega, \theta)$ reverses for angles below and above θ_c. A few subtle points about the two-center interference model must also be considered. We list them in the following:

(1) The fact that the molecular HOMO can be written as $\frac{1}{2}\left[\phi(\mathbf{r} - \frac{\mathbf{R}}{\mathbf{2}}) \pm \phi(\mathbf{r} + \frac{\mathbf{R}}{\mathbf{2}})\right]$ does not mean the molecules are bonding (antibonding), or symmetric (antisymmetric) in terms of the mirror symmetry. The accurate description of two-center structure is that after a translation of distance $\mathbf{R}$, the two atomic orbital can exactly overlap with each other [52].

(2) The term $d(\Omega, \theta) = \int e^{-i\mathbf{kr}} O\phi(\mathbf{r}) d\mathbf{r}$ is still a function of angle θ. For hydrogen molecules, this is not obvious, because the HOMO is a symmetric superposition of two isotropic s orbitals. But for CO_2, which is a superposition of two $\phi(\mathbf{r})$ is p orbitals, the dipole $d(\Omega, \theta)$ depends on the angle θ between $\mathbf{k}$ and $\mathbf{r}$. However, in most cases the prefactor of two-center interference will dominate the angular dependence of HHG.

(3) The phase of HHG $\Phi(n, \theta)$ is a function of the harmonic order n and molecular orientation angle θ. It consists of two parts according to the Lewenstein model: the intrinsic phase that is accumulated in the continuum and the phase of recombination dipole. The intrinsic phase, which gives a chirp of the generated attosecond pulse, depends on the ionization potential I_p and harmonic order, but does not depend on molecular orientation, while the phase of recombination dipole depends on the molecular orientation.

(4) If we plot the prefactor $\sqrt{2}\sin(\frac{kR\cos\theta}{2})$ for CO_2, we can clearly see that the value of this factor has a different sign between $[0,\pi/2]$ and $[\pi/2,\pi]$. This must be an artificial effect because the nuclei of the molecules are fully symmetric around the laser polarization [53]. The reason of this effect is that we break up

the correlation between the continuum and bound electron. Since the electron wave packet is ionized from the most probable region in the molecules (the lobe along the laser polarization), it actually changes sign when molecules rotate from θ to $\pi - \theta$ angle. The HOMO does not have an absolute phase, therefore the relative phase between the return electron plane wave and the HOMO determine the phase of the recombination dipole. This argument can be confirmed by a TDSE calculation of a simple molecule with '-' sign superposition of atomic orbitals.

(5) In the derivation of the two-center interference model, we use velocity gauge operator instead of length gauge. Since the wave function we use to calculate the dipole is not an exact wave function, the result depends on the gauge used. Previous studies have shown that the velocity gauge gives a better agreement with the TDSE calculation than the length gauge [54].

In this section we first use a gas-mixture method to extract the alignment dependent phase of HHG from molecules, where the HHG emission from an atomic gas is used as a reference [51]. Second, we present the first direct and accurate measurement of the phase of harmonic emission from molecules [55]. We directly confirm that a two-center interference in the CO_2 and N_2O HHG emission induces a minimum at certain angular distributions, with a corresponding phase shift of π. We fit the harmonic emission as a function of time within a rotational revival to the two-center interference model convolved with the rotational distribution, which allows us to extract the ratio of the two-center separation in the molecule to the returning electron wavelength as a function of harmonic order. The data show that the contribution from the molecular potential on the electron kinetic energy varies with harmonic order, and as a result, the relationship between the harmonic energy and the recolliding electron kinetic energy also changes. These results have important implications for efforts to extract molecular structure from measurements of the harmonic emission from molecules, and can be used to benchmark realistic theories of molecules in strong fields.

4.2 Using gas mixtures to measure the phase of molecular HHG

Recently we have used a mixture of atomic and molecular gas to indirectly measure the phase of the HHG emission from molecules[51, 56]. Consider a mixture of an atomic (Kr) and a molecular (CO_2) gas. The emission intensity of a single harmonic order generated from a mixture of an atomic (Kr) and a molecular (CO_2) gas. is then the coherent sum of the emissions from both species.

The total emission from CO_2 is a coherent convolution of HHG from perfectly aligned molecules and the angular distribution function $\rho(\theta, t)$.

After exciting the rotational wave packet in CO_2, the magnitude (S_{CO_2}) and phase (ϕ_{CO_2}) of the harmonic emission depends on the wave packet evolution and will vary with the time delay between the pump alignment pulse and probe harmonic-generation pulse.

$$S_{A,CO_2}(\Omega, t) = \int_0^{\pi} S(\Omega, \theta)\rho(\theta, t)d\theta \tag{4.4}$$

We can split the HHG amplitude from CO_2 and Kr as magnitude and phase terms, $S_{A,CO_2}(\Omega, t) = A_{CO_2}(\Omega, t)\exp(i\phi_{CO_2})$ and $S_{Kr}(\Omega, t) = A_{Kr}(\Omega, t)\exp(i\phi_{Kr})$ The total harmonic intensity from the mixture gas with fraction $a(0 < a < 1)$ of CO_2 can be written as

$$\begin{aligned} HHG(a) \quad &= |aA_{CO_2}\exp(i\phi_r) + (1-a)A_{Kr}|^2 \\ &= a^2A_{CO_2}^2 + (1-a)^2A_{Kr}^2 + 2A_{CO_2}A_{Kr}a(1-a)\cos\phi_{CO_2} \end{aligned} \tag{4.5}$$

while $\phi_r(\theta)$ is the phase of the emission from CO_2 relative to krypton.

The atomic phase from unaligned CO_2 and Kr are the same, since they have similar I_p. Therefore, $\phi_r(\theta)$ is the relative phase mostly comes from the recombination step. We take the temporal scan for rotational period of the CO_2 and Kr mixture. With the HHG intensity of pure CO_2 and Kr measured, We can first solves the complex HHG dipole for CO_2.

The rotational wave packet angular probability density is well understood and can be calculated [57] as we discussed in the last chapter. It is therefore possible to retrieve the orientational dipole from the measured time-dependent harmonic emission from rotationally excited molecules and atomic gas mixtures.

Although we observe phase change when the molecules are aligned from the gas mixture data, this method is inaccurate because the fraction a is not a well-controlled parameter. Even given a pre-measured mixture of gases, due to the different adiabatic constant γ of CO_2 and Kr, the real fraction in the interaction region will be different from the original mixture ratio. The rotation temperature and density distributions also depend on a. The recombination phase of Kr is not well-known, because the structure of atoms can result in phase variations as well [58].

4.3 Double-focus interferometry for simultaneous intensity and phase measurement

Hakan TureciTo determine the variations in the phase of HHG emission, an interferometry measurement is ideal. Although a double-focus interferometric geometry has been used before to measure the coherence of HHG and the atomic dipole phase of HHG [59, 60], here we use a new geometry that is both exceedingly stable and simple to implement. Beam path-length stability is especially critical for interferometric measurements due to the short wavelength of the harmonic light. We use two glass plates tilted at slight angles, and partially inserted into the focusing laser beam (2∼3 cm after a lens of 30 cm focal length), to split the focus into two elliptical focal spots with diameters (full width at half maximum) of ∼80 μm, as shown in Fig. 4.4. The transverse distances between the two foci and the exit of a continuous gas jet with 150

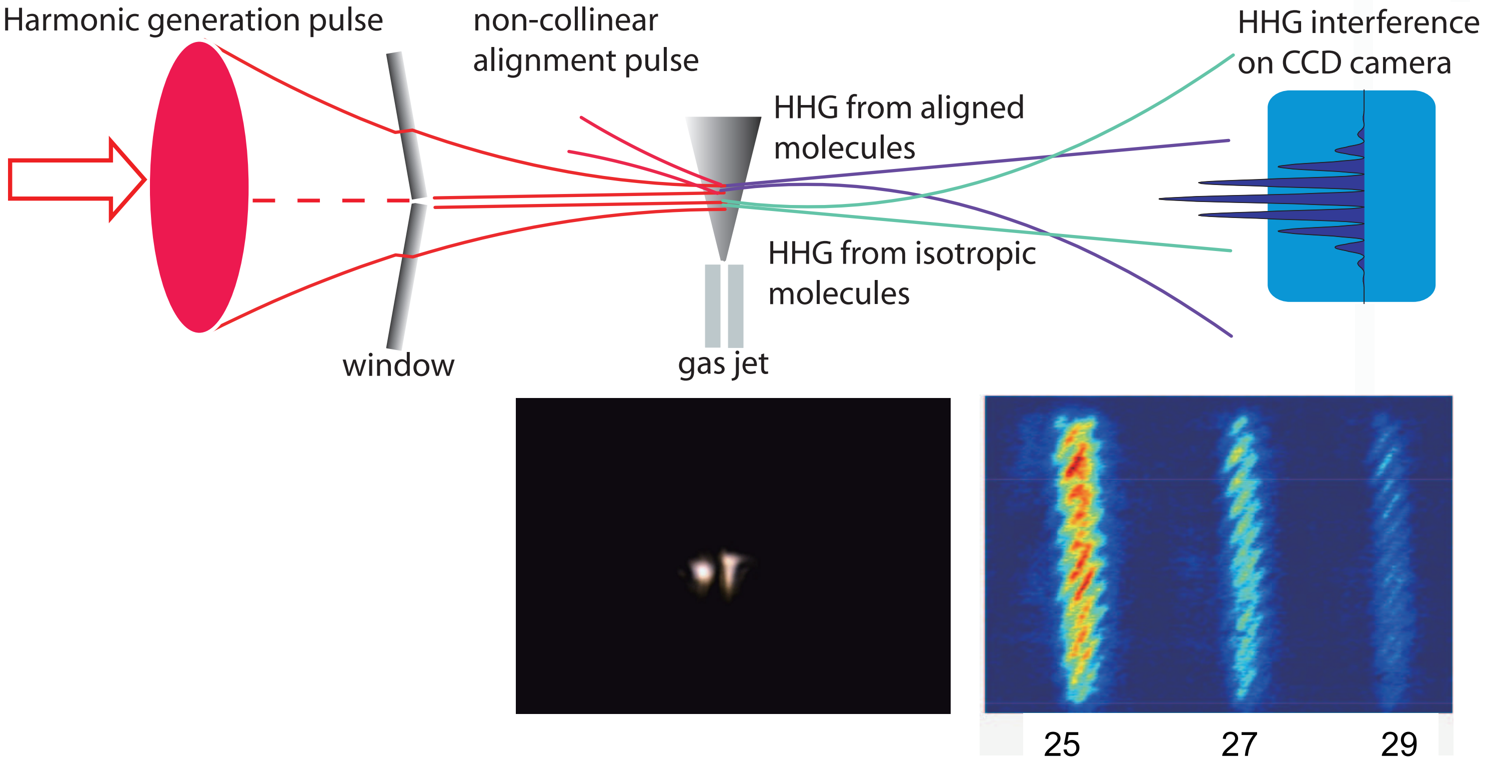

Figure 4.4: Schematic setup for directly measuring the intensity and phase of high harmonic emission from molecules. HHG from aligned and randomly oriented molecules from two different regions interfere in the far field. Figure adapted from [55].

μm diameter are 110 μm and 240 μm respectively. The stagnation pressure of the gas is 700 Torr. The duration of the harmonic generating pulse is 25 fs, with 550 μJ of energy in each focal spot, corresponding to a focal intensity of about 2.5×10^{13} W/cm^2. To select harmonics originating from the short trajectories, the focal positions of both foci are slightly before the gas jet. The harmonics from these two regions emerge and interfere in the far field. Slight adjustment of the angles of the two plates can change the distance between the two foci, and the relative angle between them can change the time delay. A second beam with the same polarization and containing 320 μJ of energy in 120 fs is focused non-collinearly (crossing angle $<$ 2 degrees) into the molecular gas at the position of one focus, at an estimated intensity of 4–6×10^{13} W/cm^2, to create a transient molecular alignment. The HHG from the unaligned focus serves as a constant phase reference. Any fringe shift observed will arise from a phase change of HHG from the aligned molecules. By blocking the high harmonic generation laser pulse in the unaligned region, we can characterize the harmonic emission from the aligned molecules. A flat-field cylindrical focus grating spectrometer dispersed the harmonic spectrum and imaged the harmonic in one dimension onto an EUV CCD. Stable EUV interference fringes were observed for harmonic orders up to order 31, since the divergence of the HHG emission from the two regions causes a spatial overlap on the CCD in the non-imaging direction. Above order 31, the divergence and intensity of the beams is too small in our geometry to observe fringes. A similar setup was also reported recently.

4.4 Quantum interference in CO_2 molecules

Fig. 4.5 (a) shows the net harmonic intensity for orders 19–45 as a function of time delay between the alignment and harmonic generation pulses through the 3/4 revival, where the molecules can be most strongly aligned. These data exhibit a very different behavior for harmonics above and below the 27th. To see this more clearly,

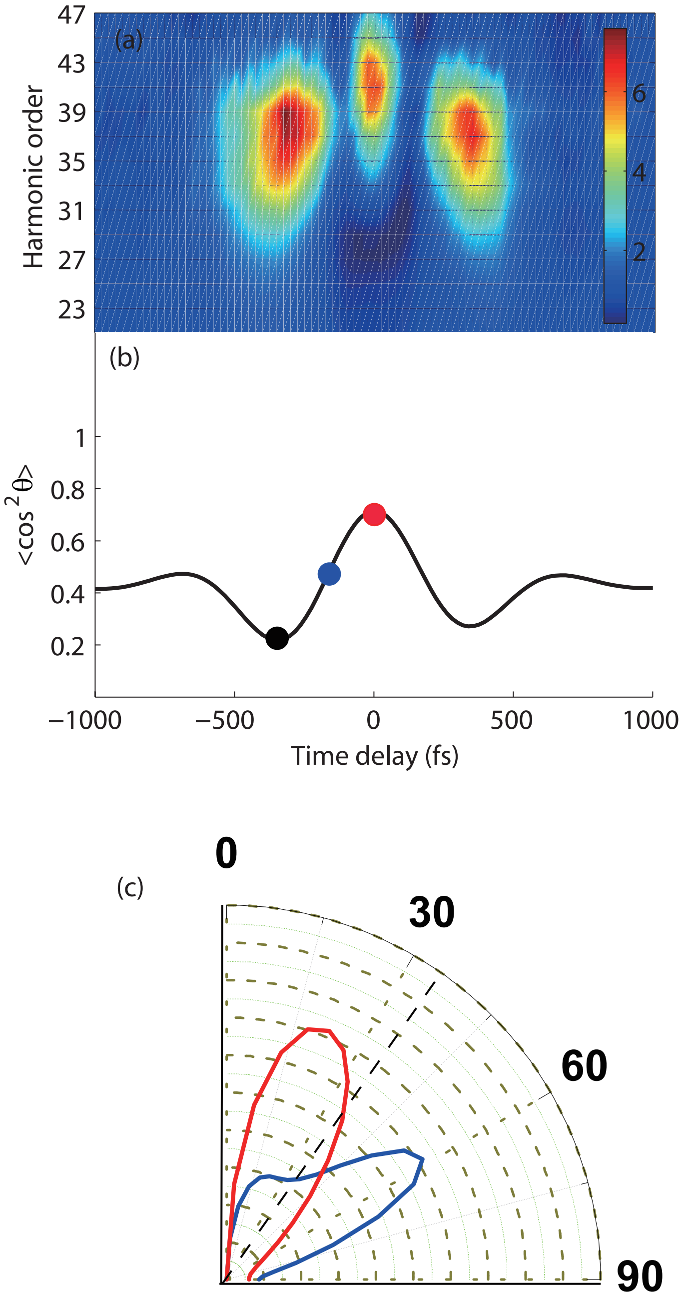

Figure 4.5: (a) Experimentally measured intensity (from the aligned molecular sample only) for harmonic orders 19 - 45 as a function of time-delay between the aligning laser pulse and harmonic-generating pulse within the 3/4 revival. Time zero is shifted to the center of this revival for convenience. (b) Predicted $\langle \cos^2 \theta \rangle$ alignment assuming a rotational temperature of 105 K. The inset plots the angular distribution at three selected times within the revival, color coded to indicate the corresponding time on the $\langle \cos^2 \theta \rangle$ graph. Here, 0° corresponds to alignment along the laser polarization, while 90° corresponds to "anti-alignment." (i.e. perpendicular to the laser polarization) The critical angle of 34° for harmonic order 31 is also labeled. Figure adapted from [55].

lineouts of different harmonics are shown in Figs. 4.6. Below order 27, the intensity follows an inverse of the $\langle \cos^2 \theta \rangle$ ensemble averaged alignment parameter (shown in Fig. 4.5(b)); i.e. HHG emission is minimum when the molecule is aligned parallel to the laser polarization. In contrast, for harmonics > 27, the yield first goes through a minimum, and then increases for a short time when the molecules are best aligned. Stronger molecular alignment in our sample, as well as improved signal-to-noise ratio in the detection of the harmonics, allowed us to observe this anomalous peak which has not been reported previously. This feature is strongly suggestive of a phase shift due to quantum interferences.

To confirm that quantum interferences are the origin of the additional central peak in HHG from aligned molecules, we directly compare the phase of HHG from aligned and unaligned molecules using the setup shown in Fig. 4.4. Fig. 4.7 (a) and (c) plot the observed interference pattern for orders 25 and 31. For order 31, a fringe shift can clearly be observed when the molecules are strongly aligned. No such shift is observed for order 27. The time window for this phase shift exactly matches the duration of the anomalous peak seen in the intensity of order 31 as a function of alignment (Fig. 4.6 (d)). To determine the magnitude of the phase shift between harmonic emission from the aligned and randomly-oriented molecules, we integrate the interferences fringes between -100fs and 100fs. We then compare this with the integrated fringes outside this temporal window, where there is no strong alignment. The results are shown in Fig. 4.7 (b) and (d). We use a sine function added to a slowly varying polynomial background to fit the data. We retrieve a phase difference of 3.4 ± 0.3 radians for order 31, and 0.035 ± 0.5 radians for order 27.

The inset of Fig. 4.5 (b) shows the predicted angular distribution at three different times in the 3/4 revival, to illustrate the effect of angular averaging. As explained above, the critical angle θ_c corresponds to that angle where the phase of the harmonic emission changes. At maximum alignment (red curve), most of the distribution is on one side

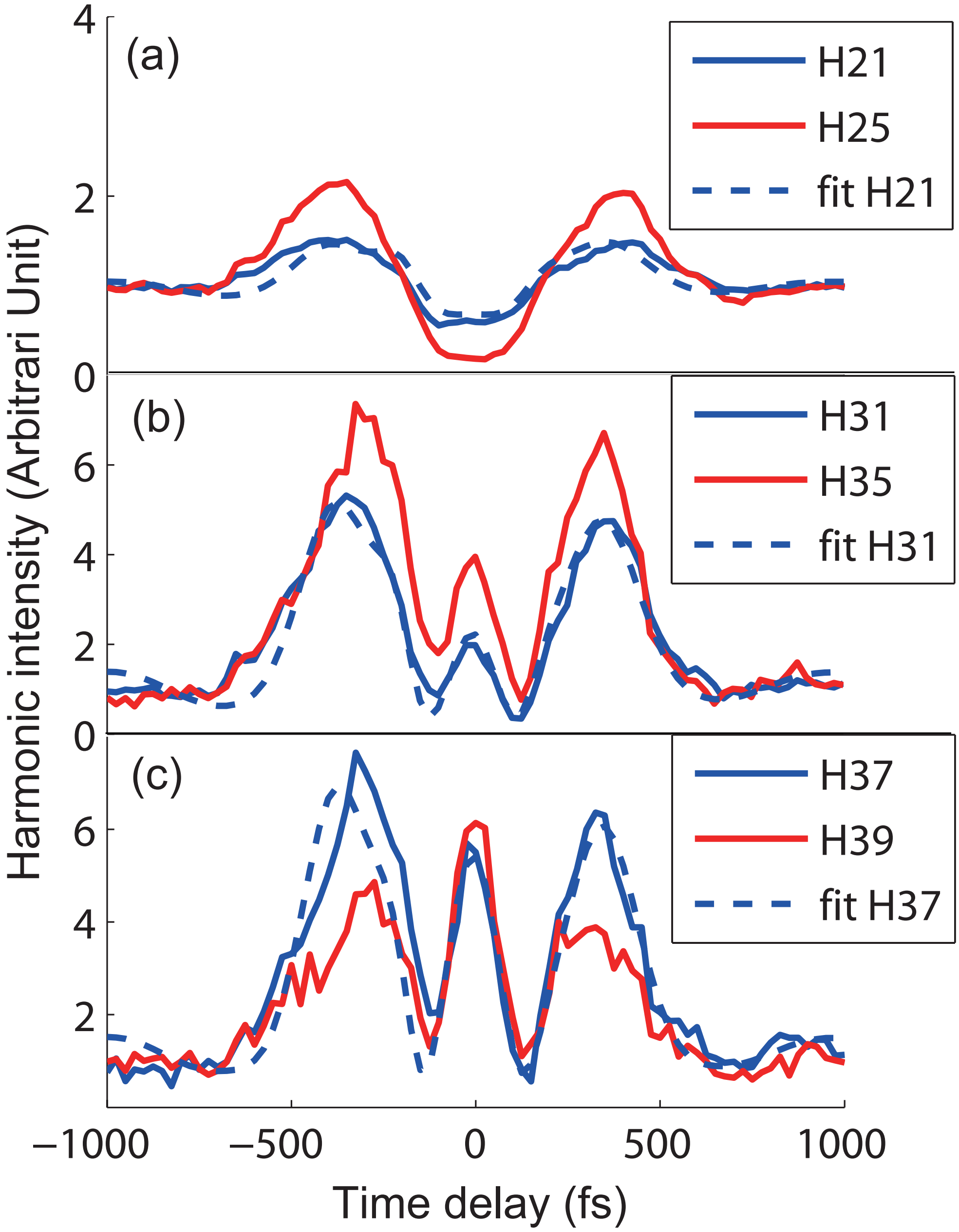

Figure 4.6: Lineout of harmonic orders 21, 25, 31, 35, 37, and 39 that exhibit different sub-structure in the harmonic emission at optimal alignment. The dashed line shows a least-square fit to Eqn. 4.6 for harmonic orders 21, 31 and 37. Figure adapted from [55].

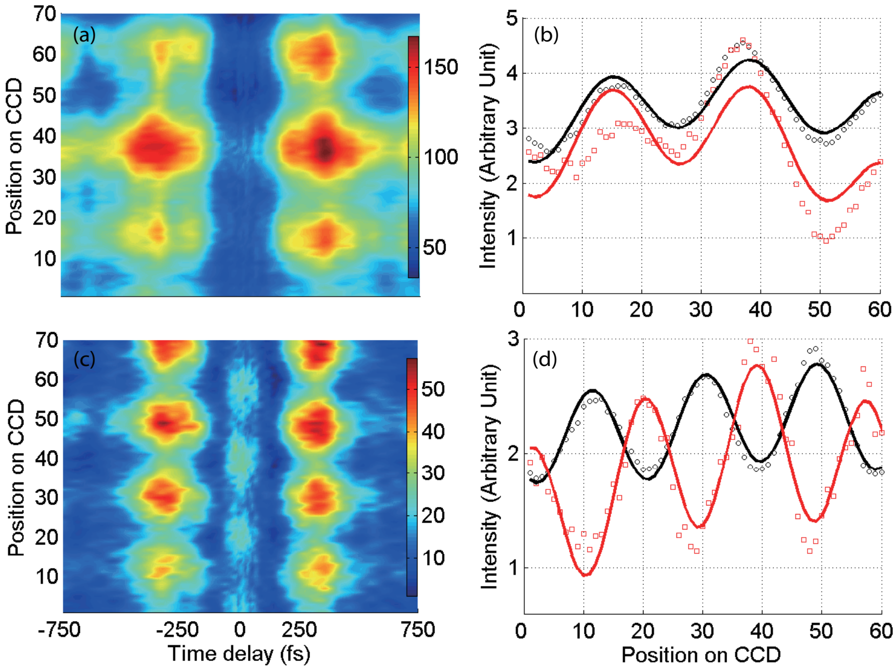

Figure 4.7: (a), (c) Interference pattern as a function of time within the 3/4 revival for harmonic orders 25 (a) and 31 (c). (b) Intensity-scaled integrated fringes for the 25th harmonic in the -100 fs to 100 fs interval (red squares), along with least square fit (red solid line). Integrated fringes outside this temporal window are also shown (black circles) as well as a least square fit (black solid line). (d) Same as (b), but for the 31rd harmonic. Figure adapted from [55].

of $\theta_c \approx 34°$ for order 31. At the other two time delays (blue and black curve), the net harmonic signal will have opposite phase since most of that distribution lies on the other side of θ_c. Therefore, a phase shift of π is expected in the interference pattern during the revival, in agreement with our data. In contrast, for harmonics < 27 the critical angle is smaller, and therefore the phase of the harmonic emission does not change during the revival. Putting this result into the context, in Ref. [48, 49] the authors convolved the two-center harmonic intensity modulation with the angular distribution *without* accounting for the coherent nature of HHG generation. Our work shows clearly that the harmonic emission adds coherently. Other recent work [35] has also found that to reproduce experimental data, a coherent sum of HHG emission is required to model harmonics from aligned molecules.

From our measurements of the harmonic intensity and phase, we accurately identify the spectral position of the interference minimum and corresponding phase shift in harmonic emission, which qualitatively agree with the two-center interference model. To further test the validity of this model, we fit the measured harmonic intensities for times around the 3/4 revival using the expression -

$$HHG(t) = \left| \int_0^{\pi/2} \rho(\theta, t) A \sin(\pi R \cos\theta / \lambda) d\theta \right|^2 + C \tag{4.6}$$

In Eqn. 4.6, the $\sin(\pi R \cos\theta/\lambda)$ term results in quantum interference. A is a scaling factor, while C accounts for any non-coherent part in the detected signal. Since we do not have very accurate independent measures of the rotational temperature and the pump laser intensity, we calculate the angular distribution $\rho(\theta, t)$ for different rotational temperatures (75 K, 85 K, 95 K, and 105 K) and pump intensities (4.0, 4.5, 5.0, 5.5, and 6.0 $\times 10^{13}$W/cm^2 by numerically solving the TDSE following the procedure of [57].

These values are within our experimental estimates. We performed the least square fit with fitting parameters A, B ($=R/\lambda$) and C, using each one of these angular

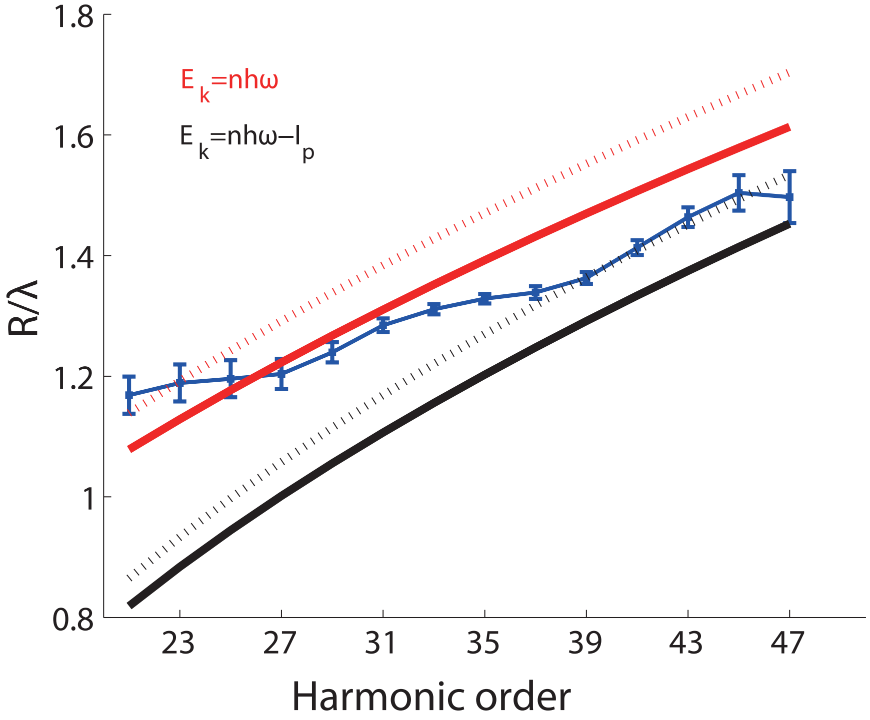

Figure 4.8: Extracted value of $\dfrac{R}{\lambda}$ versus harmonic order from the fits shown in Figs. 4.6 (blue squares with error bar). The calculated value of $\dfrac{R}{\lambda}$ is also shown for two different dispersion relationships and internuclear separations: $E_k = n\hbar\omega$ - I_p and R=2.32Å(black solid line), R=2.45Å(black dashed line); $E_k = n\hbar\omega$ and R=2.32 $\mathring{A}$ (red solid line), R=2.45 $\mathring{A}$ (red dashed line). Figure adapted from [55].

densities for all harmonic orders, and finally we sum the squares of the residuals to determine the goodness of each fit. The best overall fit for all harmonic orders was obtained using a rotational temperature of 105 K, and a pump laser intensity of 5.5×10^{13} W/cm^2. Least squares fits to Eqn. 4.6 for three representative harmonics - orders 23, 33, and 39 – are shown in Fig. 4.6. These fits are also in excellent agreement with the two-center model, and also provide compelling evidence that the primary features in the angular modulation of HHG emission intensity and phase from CO_2 result from quantum interferences in the recombination process.

Since the inter-atomic separation R should be independent of the harmonic order, we can use R as a "ruler" by which to measure the wavelength λ of the recolliding electron [48, 61]. Fig. 4.8 plots the extracted value of $B = R/\lambda$ with the error bar determined by 95% confidence interval, together with the theoretically predicted curves for R=2.32 Å and two different dispersion relationships: $E_k = n\hbar\omega - \delta I_p$ ($0 < \delta < 1$). Our experimental data show that the ratio R/λ does not follow a relationship corresponding to a fixed value of δrather that δ is near 0 for low order harmonics, and increases for higher orders. The effect of the Coulomb potential on the continuum electron is the most probable reason for this behavior. The molecular potential can further accelerate the returning electron and distort the wave front from that of a plane wave. To a first approximation, we can consider the Coulomb effect as a correction to the kinetic energy of the returning electron plane wave. The equation E_k= $nh\omega$ - I_p gives asymptotic kinetic energy of the electron, corresponding to some momentum vector k.

Further acceleration of the electron inside the molecular potential will give an additional momentum shift Δk and a phase shift$\Delta k \cdot R$. Our data show that this phase shift is small for high order harmonic and larger for lower orders. For harmonic orders below 25, our extracted value of $E_k = n\hbar\omega$ is even larger than the calculated value using a dispersion relationship $E_k = n\hbar\omega$, which most likely is due to a breakdown of the plane wave approximation for low order harmonics. Other possible explanations include multi-electron effects, or field distortion of the molecular HOMO which might stretch the effective distance between the centers of electron density. Two dashed curves calculated using a slightly longer R (2.45 Å) are also shown in Fig. 4.8 for comparison. The effort to develop a complete theory of HHG in molecules that includes multi-electron and Coulomb effects will be helpful to fully understand our data [39, 62, 40, 63].

4.5 Quantum interference in N_2O and N_2 molecules

N_2O is a linear molecule with a HOMO structure very similar to CO_2. Because of the asymmetry of nitrogen and oxygen atoms, N_2O has a permanent dipole moment. However, the orientation effect is averaged out during the pump pulse, therefore, we observe similar behaviors of HHG from aligned N_2O and CO_2 molecules. The HHG intensity evolution during a full rotational period of N_2O is shown in Fig. 4.9, Due to different nuclear spin statistics, N_2O molecules do not have strong 1/4 and 3/4 revivals as in the case of CO_2.

There is a local maximum when the molecules are strongly aligned for harmonic order above 27. This local maximum corresponds to the two center interference induced phase flip. We perform a double-foci interferometry measurement as shown in Fig. 4.10 for harmonic orders 25 and 29, the π phase change is clearly visible for harmonic 29th when the molecules are aligned.

There is an extra feature for low order harmonics (15th, 19th, and 23rd), when the molecules are anti-aligned. This local minimum on the top of the anti-alignment peak can also be explained by the two-center modulation factor shown in Fig. 4.3. Because when the molecules are anti-aligned, the angular distribution can pass the peak of the modulation factor and start to decrease. The angle where this peak located is small for low order harmonics, therefore, easy to be achieved.

We also extend our interferometry technique to N_2 molecules. Unlike N_2O and

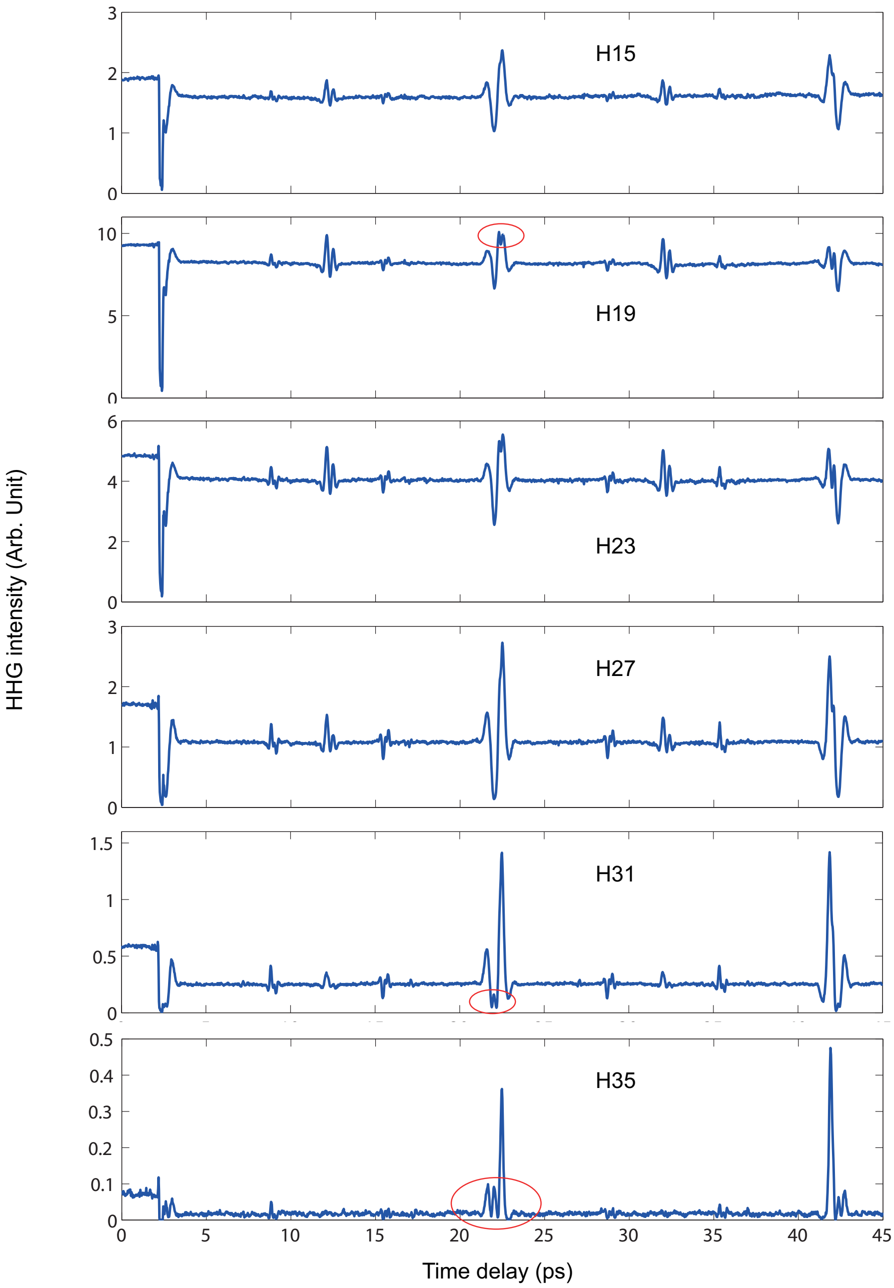

Figure 4.9: Measured harmonic intensity for the 15th, 19th, 23rd, 27th, 31st, and 35th harmonics during a full rotational period of N_2O.

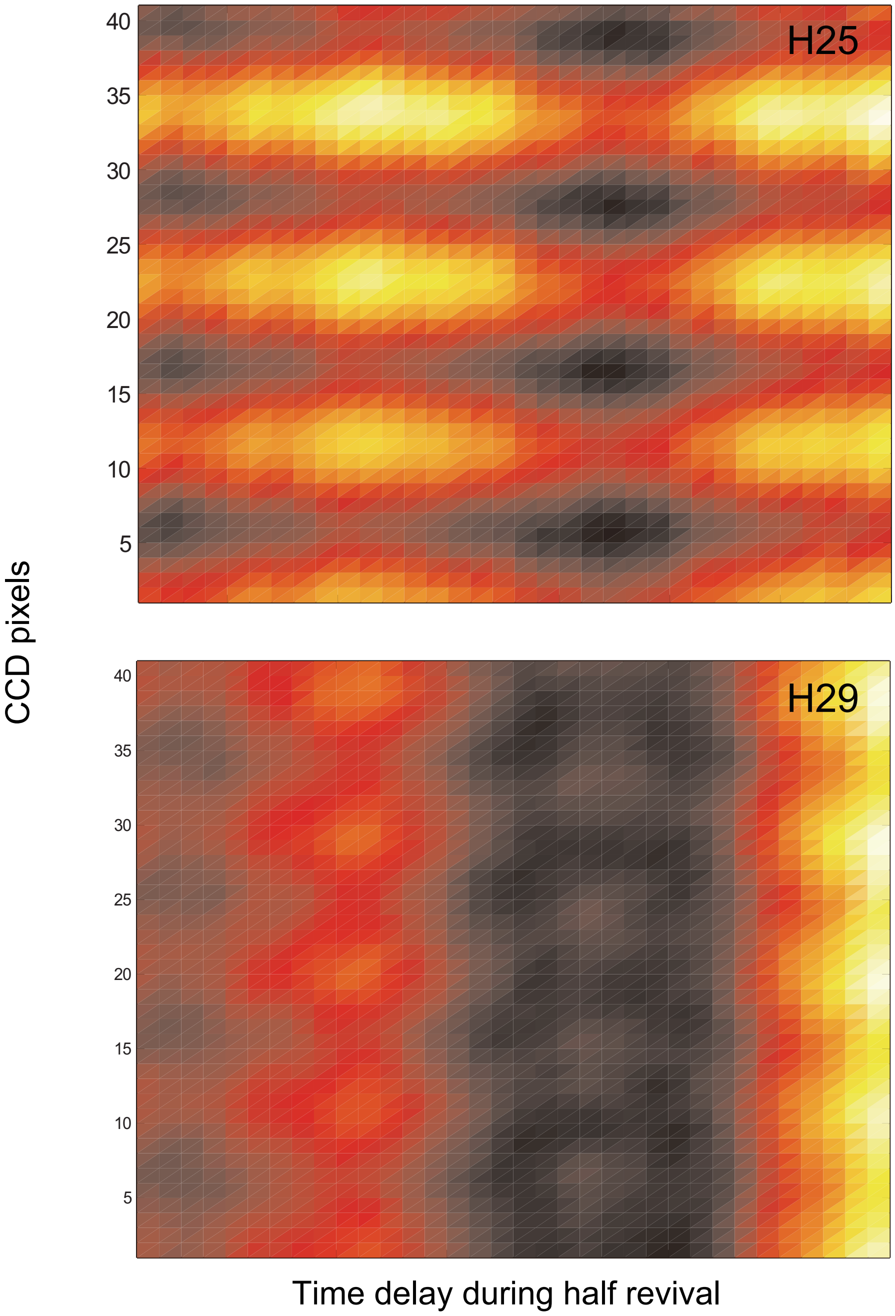

Figure 4.10: Interference fringes as a function of time delay during half revival for the 25th (a) and 29th (b) harmonics from N_2O.

CO_2, the HOMO of N_2 can not be decomposed to pure '+' or '-' sign superpositions of atomic orbitals. The N_2 molecular orbital is constructed by a mixture of 70% of atomic p orbitals and 30% of atomic s orbitals. The atomic p orbitals are superposed with a '-' sign and the atomic s orbitals are superposed with a '+' sign. The HOMO of N_2 has a σ_g symmetry. Consequently, two-center interference model are not enough to describe the alignment-dependent HHG emission from N_2. Under the plane-wave approximation, we can calculate the HHG dipole by performing Fourier transform of the molecular HOMO calculated with quantum chemistry code. These calculations are carried out in two recent papers [64, 65]. Both calculations predict a π phase jump at the harmonic range and alignment angles that are experimentally accessible, although the exact location of this phase jump slightly depends on how HOMO wave function is calculated. However we do not see any angle dependent minimum and phase change in our measurement of N_2 during the revivals, as shown in Fig. 4.11. We perform the phase measurement on N_2 as well, we do not see any phase shift for harmonic orders between 19 and 33.

In summary, for CO_2 and N_2O molecules, we present an accurate and unambiguous measurement of the phase shift of high-order harmonic emission in molecules for the first time. The data also allow for a detailed measurement of the dispersion relation between the wavelength of the recolliding electron and the harmonic order. While for N_2 molecules, we do not observe the angular dependent phase shift and minimum predicted by the plane-wave recombination model. Therefore, our data will be very useful to benchmark complete theories of harmonic emission from molecules.

A recent experiment [66] also measures the angular dependent harmonic phase of CO_2 using the interference of two-photon (one EUV photon and one IR photon) transitions [67].

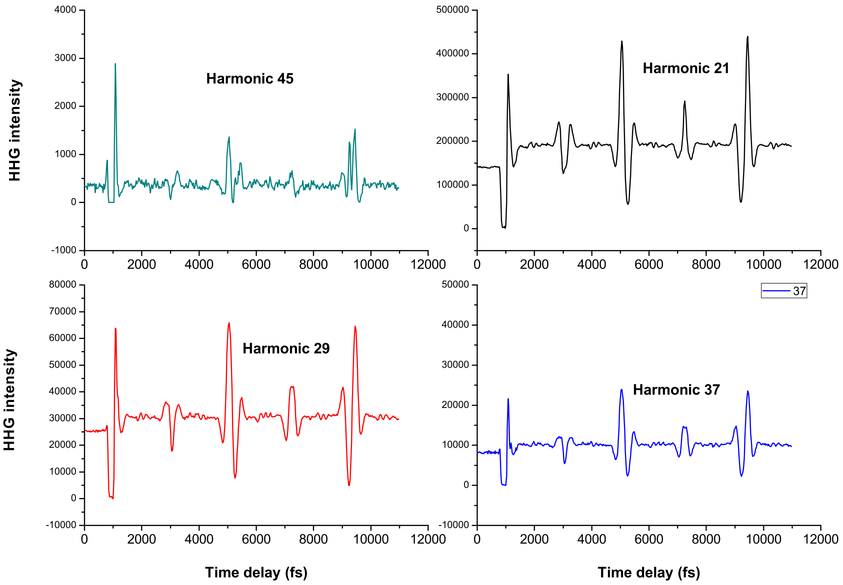

Figure 4.11: Intensity change versus time delay during a full rotational period of N_2.

Chapter 5

Polarization resolved characterization of HHG from aligned molecules

5.1 Observation of elliptically polarized HHG from molecules driven by linearly polarized laser light

In principle, the amplitude, phase and polarization of the HHG emission can be measured and used to extract the electronic structure of molecules from the transition dipole matrix element. However, until very recently, only the intensity of high harmonic emission was measured. Fortunately, new approaches have allowed the phase of HHG to be determined as we discussed in the last chapter [55, 66].

In this chapter, we perform a full and accurate polarization measurement of high harmonic emission from aligned molecules for the first time. Surprisingly, we find that harmonic emission from nitrogen molecules can be strongly elliptically polarized even when driven by linearly polarized laser fields. We extract the relative phase difference between the HHG components parallel and perpendicular to the driving laser field, which depends only weakly on molecular alignment but which strongly depends on the harmonic order. Our findings differ from previously published results [68], where only linearly polarized harmonic emission was observed, because we achieve stronger molecular alignment and better signal-to-noise ratio (∼1% intensity fluctuation), allowing us to detect an elliptically polarized HHG emission when molecules are driven by linearly polarized laser fields. These findings cannot be explained by a plane wave SFA, and will be very useful to benchmark new and more complete theories of molecules in strong fields. Moreover, our results present a straightforward and efficient way to generate circularly polarized harmonic beams for applications in molecular and materials science.

The polarization state of harmonic emission from molecules is especially interesting for the following reasons. As shown in Fig. 5.1 (a), in general, the complex amplitude of the harmonic field from a molecule has two components, parallel (y) and perpendicular (x) to the laser polarization respectively. Any component along the laser propagation direction cannot be phase matched. $E_y(\omega,\theta) = |E_y(\omega,\theta)|\exp(i\Phi_y(\omega,\theta))$ and $E_x(\omega,\theta) = |E_x(\omega,\theta)|\exp(i\Phi_x(\omega,\theta))$ depend both on the harmonic frequency ω and angle θ. In theory we should get the same reconstruction of the molecular orbital from both of the HHG components [70]. Moreover, according to the 3-step model, the ratio between the x and y components can be written as $|E_x(\omega,\theta)/E_y(\omega,\theta)|^2 = |d_x(\omega,\theta)/d_y(\omega,\theta)|^2$, which is independent of the angle-dependent ionization and is directly related to the transition dipole in these two directions. In this way, the ionization and recombination process in HHG can be isolated and studied separately. Finally, from the polarization properties of the HHG emission (the orientation angle ϕ and the ellipticity ϵ as defined in Fig. 5.1 (b)), we can map out the relative phase difference $\delta = \Phi_x - \Phi_y$ between the x and y components. Again, because the ionization and acceleration steps are common for the x and y components of HHG, this relative phase difference is not entangled with the intrinsic phase accumulated while the electron oscillates in the continuum. Thus, measuring the polarization properties of HHG should allow clear insight into strong field molecular science and also enable critical comparison with theory.

In our experiments, pump and probe pulses from a two-stage Ti: Sapphire amplifier system are focused (non-collinearly) into a molecular gas. The pump pulse is focused by a 75 cm lens to an intensity of $4\sim5 \times 10^{13}$ W/cm^2, and is used to create a rotational wave packet and field-free alignment in the molecular sample. The probe pulse is focused using a 40cm lens to an intensity of 2×10^{14} W/cm^2 and generates harmonics

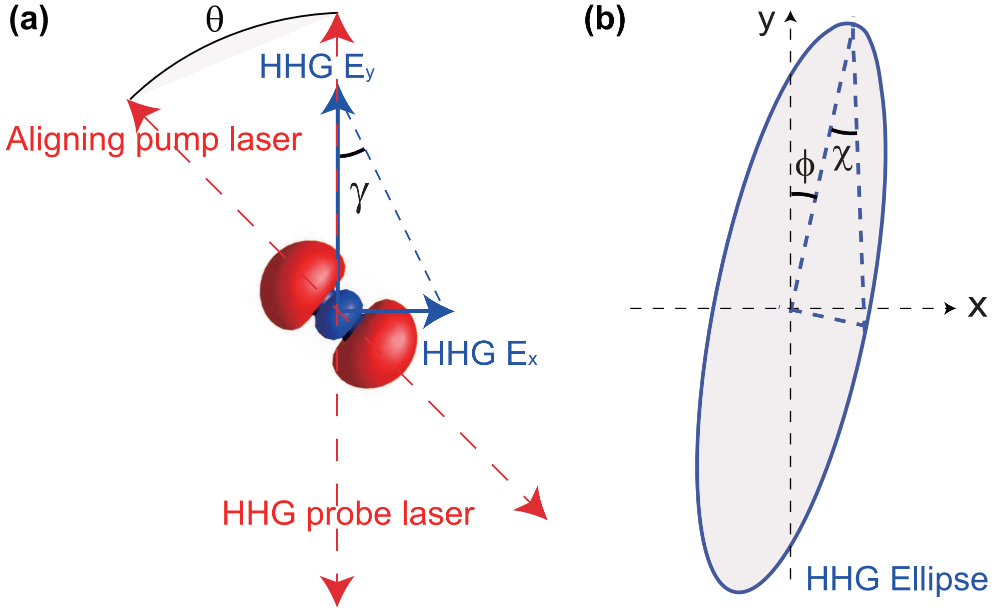

Figure 5.1: High harmonic generation from aligned N_2. (a) HHG components parallel and perpendicular to the probe laser polarization can be generated. The angle γ is defined by $\tan(\gamma)= |E_x|/|E_y|$. (b) The orientation angle ϕ of the HHG ellipse is defined as the angle between the major axis of the ellipse and the y axis. The angle χ is defined by $\tan(\chi)=\epsilon$, where ϵ is the ellipticity. ϕ and θ are positive for clockwise rotation from the y direction and negative for counter-clockwise rotation. Figure adapted from [69].

from the aligned molecules. Both foci are positioned ~150 μm from a supersonic gas jet, with a 150um orifice diameter and 700~800 Torr backing pressure. The rotational temperature of the gas was estimated to be 100 K and $\langle \cos^2 \theta \rangle$ is estimated to be 0.65 when the molecules are aligned. This high degree of alignment improves the measurement precision compared with past experiments, allowing us to observe a strong HHG component perpendicular to the laser polarization. Both alignment and harmonic generating pulses are linearly polarized. A computer controlled half-wave plate (HWP1) in the alignment beam controls the relative angle θ between the polarization of the pump and probe, while a second half-wave plate (HWP2) in the common path of the pump and probe beams can rotate the polarization of both beams together.

5.1.1 Experimental setup

To measure the polarization of the harmonic emission, the HHG beam was reflected from two gold mirrors (consisting of a gold layer of 250 nm coated on a superpolished substrate) at an incident angle of 45°. These mirrors act as an EUV polarizer, selectively reflecting S-polarization. The HHG beam was spectrally separated using an EUV spectrometer (containing a grazing incidence cylindrical gold mirror and EUV grating) and finally detected using an EUV CCD camera (Andor Technology). The transmission of the EUV spectrometer weakly depends on the incident light polarization. Due to the decreasing reflection efficiency of the gold mirrors at shorter wavelengths, only harmonic orders below the 31st can be observed. The intensity extinction ratio e of the entire detection system is carefully measured using HHG generated from isotropic molecules and atoms: e monotonically decreases from 0.08 at harmonic order 13, to 0.005 at harmonic 31. Note that the HHG beam can be partially polarized due to spatial and temporal variation of the HHG field [71]. Thus the extinction ratio measured could be contaminated by any unpolarized HHG emission. However, the

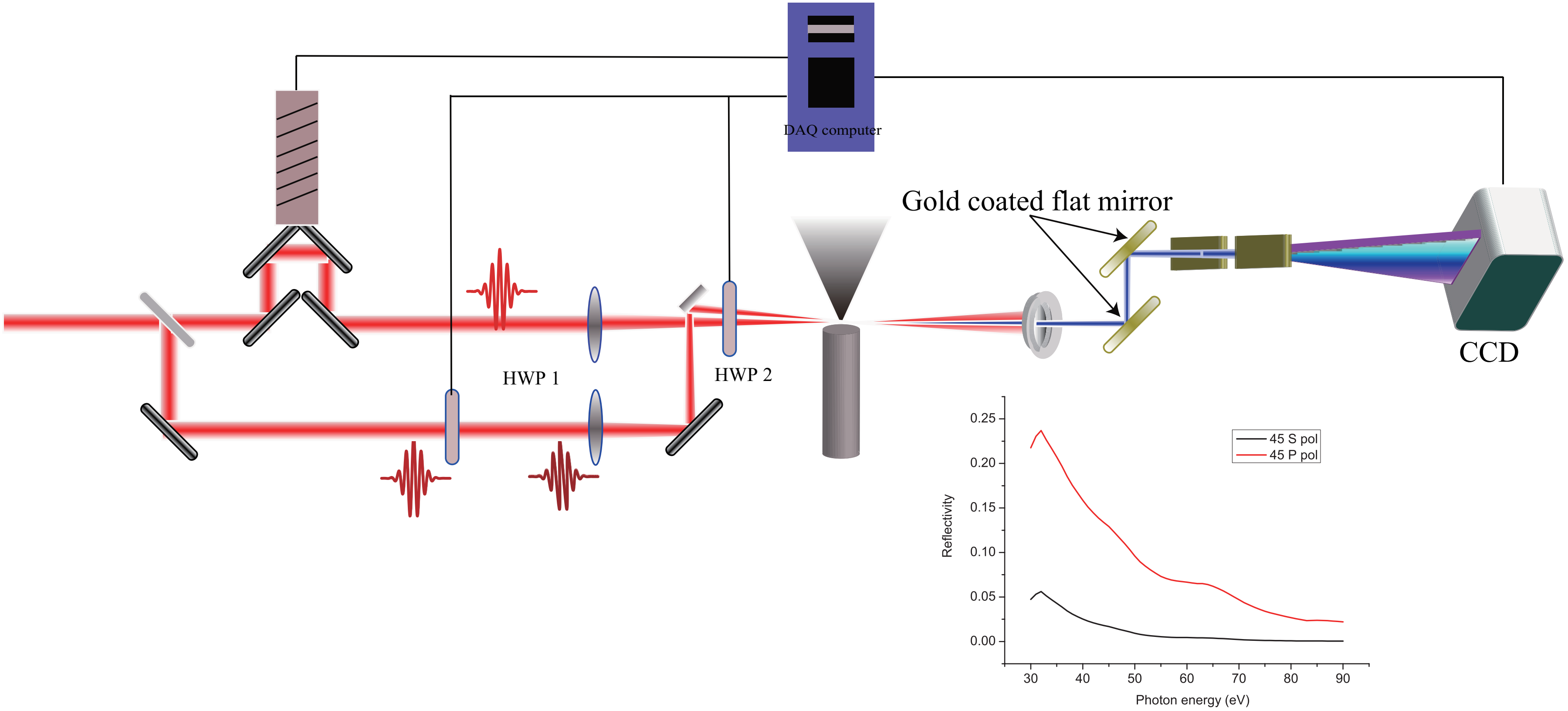

Figure 5.2: Setup for measure the polarization of HHG from aligned molecules and the reflectivity of a gold-coated mirror for S and P polarized light.

measured extinction ratio e is consistent with the calculated value for the gold mirrors pair based on optical constants, within a error of 0.015 for all harmonic orders observed [72]. Thus, we conclude that the harmonic emission is almost fully polarized and that the HHG ellipse parameters (ϕ and ϵ) are constant temporally and spatially [71]. Thus, in this paper we neglect the effect of unpolarized HHG.

If the polarizations of the pump and probe beams are parallel, the molecular angular distribution is cylindrically symmetric around the laser polarization. Thus, harmonic emission is always polarized along the laser polarization direction. To investigate the polarization of the harmonics as a function of molecular orientation, we varied the angle between the aligning pump laser and the HHG-generating probe pulse (see Fig. 5.1), while fixing the time delay corresponding to a full revival for N_2 and a three quarters revival for CO_2 such that the molecules are strongly aligned. When the cylindrical symmetry around the HHG driving laser polarization is broken, a component of harmonic emission that is perpendicular to the driving laser polarization should be observable experimentally.

5.1.2 Intensity ratio between the parallel and perpendicular components

We first analyze the intensity ratio between the parallel and perpendicular components of harmonic emission as a function of angle θ. The ratio between the measured HHG intensity when the harmonic generating laser is parallel and perpendicular to the transmission axis (S polarization) of the EUV polarizer is equal to $\dfrac{eI_y(\theta)+I_x(\theta)}{eI_x(\theta)+I_y(\theta)}$ where $I_x(\theta)=|E_x(\theta)|^2$ and $I_y(\theta)=|E_y(\theta)|^2$. Since $eI_x(\theta) \ll I_y(\theta)$, subtracting the measured e from this ratio gives the true intensity ratio between the y and x components. The intensity ratios for N_2 and CO_2 molecules are plotted in Figs. 5.3 (a) and (b) for different harmonic orders and relative angles. For N_2, we obtain zero values of this ratio for θ =-90°, 0°, and 90°, which confirms the accuracy of our background subtraction

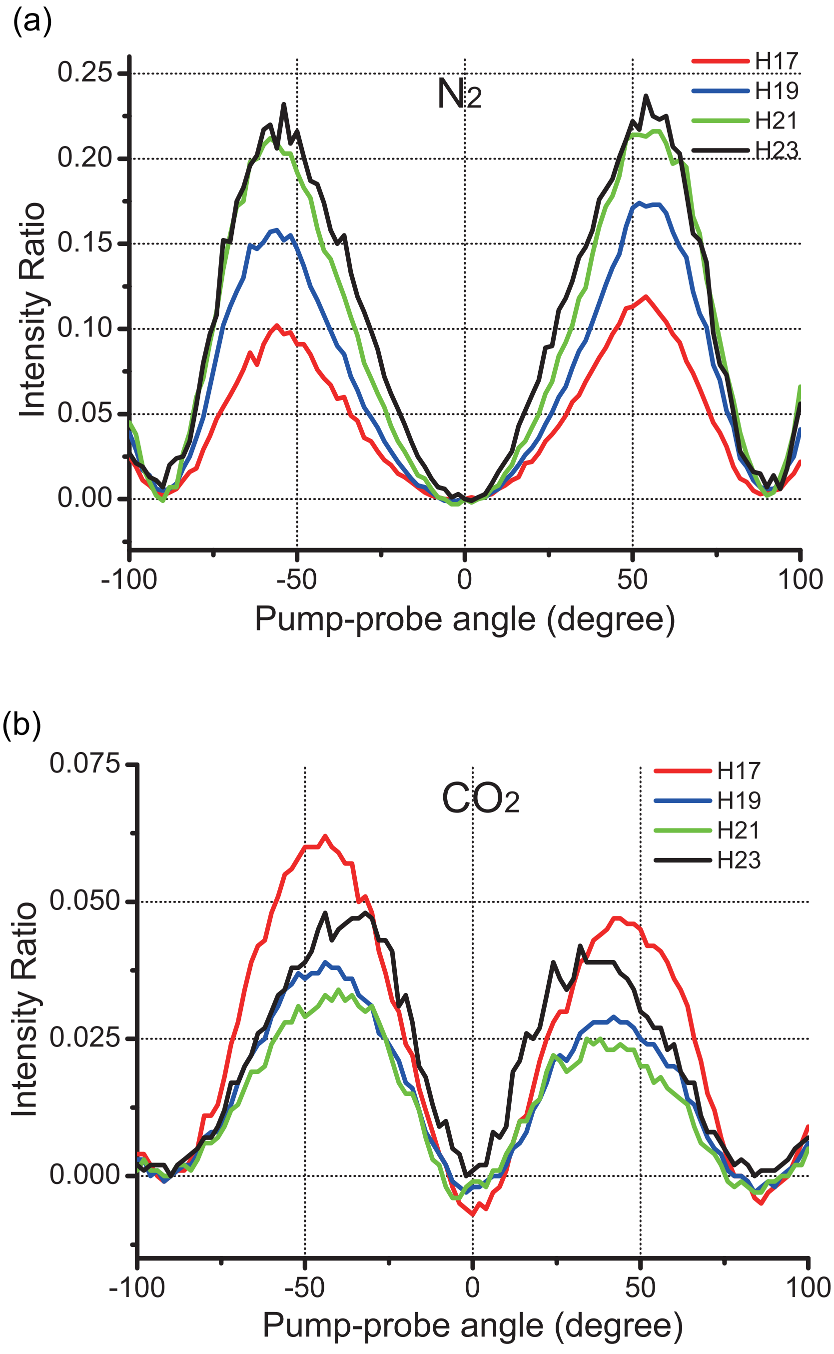

Figure 5.3: Ratio between the perpendicular (x) and parallel (y) components of the HHG field $I_x(\theta)/I_y(\theta)$ (a) for N_2 (a) and (b) for CO_2 molecules. Figure adapted from [69].

procedure. For CO_2, these values can slightly go below zero due to fluctuations, since the intensity of the perpendicular component is smaller compared with N_2. Comparing the intensity ratios of the HHG polarization components for N_2 and CO_2 shown in Fig. 5.3, we can clearly see differences. The ratio for N_2 is peaked at harmonic order 23. For CO_2 however, the ratio decreases between harmonic orders 15 and 21, but then increases quickly for harmonic orders above 23. This is because for harmonics around the 27th, the y component reaches a minimum due to two-center interference effects [9], which also makes an accurate ratio measurement difficult. The polarization properties of the harmonic emission do not only depend on the amplitudes of the x and y components, but also their relative phase difference δ. If δ is 0 or π, the HHG emission will still be linearly polarized, but the nonzero perpendicular component E_x will rotate the HHG polarization away from the driving laser polarization direction by an angle given by $\arctan(|E_x|/|E_y|)$. For other values of δ between 0 and π, the HHG will be elliptically polarized, and the orientation angle ϕ will be less than $\arctan(|E_x|/|E_y|)$. Particularly, for $\delta = \pi/2$ the major axis of the HHG ellipse will be in the direction of the driving laser polarization.

We also measure the temporal evolution of the perpendicular HHG component during a full rotational period of N_2 (Fig. 5.4), when the angle between the pump and probe pulse is 45°.

5.1.3 Orientation angle

To implement a full polarization characterization, we rotate the relative angle θ between the pump and probe from -90° to 90°, in 10° steps. Although the intensity transmission of an elliptical polarized beam through an imperfect polarizer ($e > 0$) can

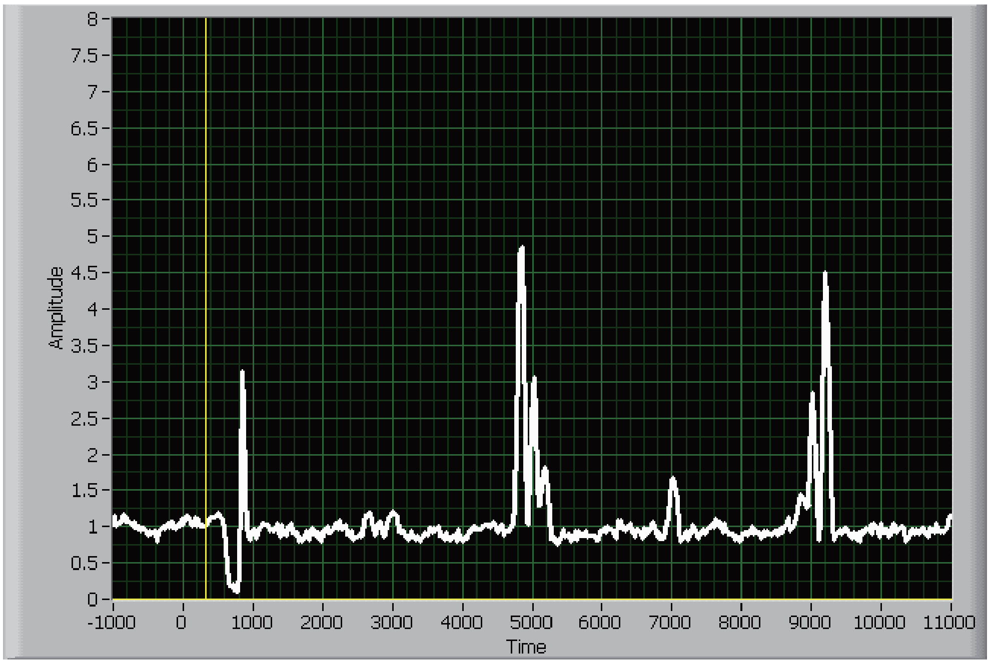

Figure 5.4: The temporal evolution of the perpendicular HHG component during a full rotational period of N_2.

be described by a more sophisticated formula containing I_x, I_y and e as parameters,

$$I(\alpha) = (1+e)(I_x + I_y)/2 + (1-e)\cos(2(\alpha - \varphi))\sqrt{I_x^2 + I_y^2 + 2I_xI_y\cos(\delta)}/2 \tag{5.1}$$

we prefer to use fewer fitting parameters and to extract these values from the final fitting result.

For each pump-probe angle, we rotate the second wave plate (which rotates the pump and probe polarizations together) by 360°, in 4° steps. We then fit the polarimetry scan data using the formula $I(\alpha) = \mathrm{a}\times\cos[2(\alpha-\phi)]+\mathrm{c}$, where α is the angle between the polarizer transmission axis and probe laser polarization. For each polarimetry scan, the maximum and minimum positions correspond to the orientation angles of the major and minor axes of the HHG ellipse.

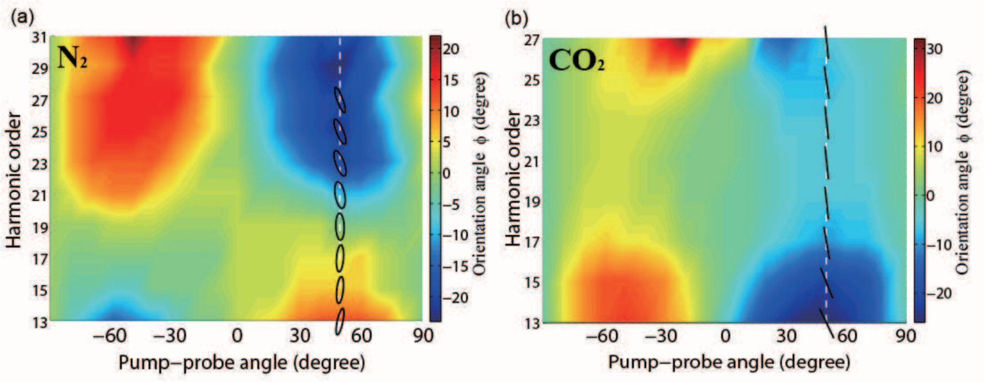

Figure 5.5: Interpolated color map of the orientation angle ϕ in degrees for different harmonic orders and molecular orientations for (a) N_2 and (b) CO_2. The HHG ellipse at θ=50° for harmonic orders 13-27 is also illustrated. Straight lines represent the harmonic polarization in CO_2 since the ellipticity is small. Figure adapted from [69].

The extracted orientation angle ϕ of the HHG ellipse in the case of N_2 is plotted in Fig. 5.5(a). For harmonic orders below 19, the major axis of the HHG ellipse rotates in the same direction as the molecular axis, while for harmonic orders greater than 19, the major axis rotates in the opposite direction to the molecular axis. The change of orientation angle of the HHG ellipse is up to 20°, indicating that a stronger molecular alignment was achieved in our sample than was the case in previous work [68]. As shown in Fig. 5.3 (a), a strong perpendicular component for the 19th harmonic was observed. However, since the orientation angle of this harmonic stays in the same direction as the HHG driving laser polarization, ($\phi \approx 0°$ for the 19th harmonic in Fig. 5.5(a)), this harmonic must be elliptically polarized.

However, for elliptically polarized light, the ratio between the minimum and maximum transmitted intensity of the polarimetry scan $I_{min}(\theta)/I_{max}(\theta)$ is given by $\frac{I_{minor} + eI_{major}}{I_{major} + eI_{minor}} \approx e + \frac{I_{minor}}{I_{major}}$ and I$_{major}$ are the intensity of the minor and major axis of the HHG ellipse. Therefore, the ellipticity of the harmonic emission, defined as $\epsilon(\omega,\theta)$ = , can be extracted from the polarimetry measurement, and is shown in Fig. 5.6 (a). We find that harmonics from aligned N_2 molecules can be strongly elliptical polarized, with ellipticity up to 0.35 for harmonic orders near the 21st. The extracted ellipticity ϵ for different harmonic orders at orientation angles θ=40°, 50° and 60° are plotted in Fig. 5.6 for N_2 (these data are averaged for positive and negative θ angles). In contrast, for CO_2, the measured ellipticity is relatively small (<0.1), which is a few times smaller than in the case of N_2 and only slightly above the noise fluctuation. Thus, the strong perpendicular components at harmonic orders below 17 and above 23 shown in Fig. 5.3 (b) rotates the predominantly linearly polarized HHG without introducing significant ellipticity. As shown in Fig. 5.5 (b), this rotation of the polarization is in the opposite direction to the rotation of the molecular axis.

5.1.4 Ellipticity and phase delay

From the measured ellipticity ϵ and orientation angle ϕ of the N_2 harmonic field polarization ellipse, we can extract the phase difference δ between the polarization components, using the formulae $\sin(2\chi)=\sin(2\gamma)\sin(\delta)$ and $\tan(2\phi)= \tan(2\gamma)\cos(\delta)$ [73].

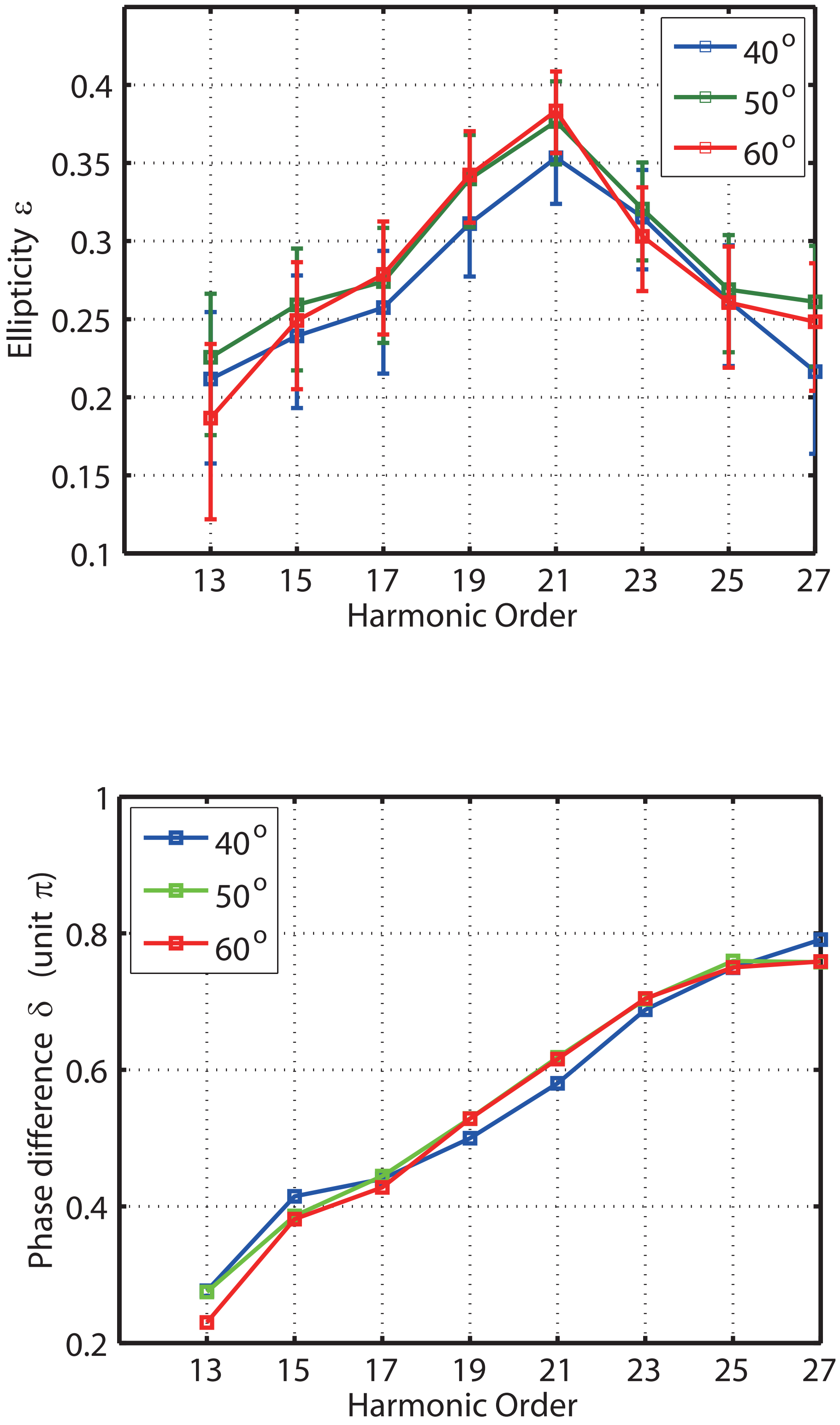

Figure 5.6: (a) Ellipticity ϵ for relative angles between the pump and probe of θ =40°, 50° and 60°, as a function of harmonic order for N_2. (b) Calculated phase difference δ between the parallel and perpendicular components of HHG emission in N_2. Figure adapted from [69].

The extracted value of δ for θ=40°, 50° and 60° degrees for different harmonic orders is plotted in Fig. 5.6 (b) for N_2. The relative phase difference is almost independent of the molecular orientation angle θ, and gradually increases from 0.2 π to 0.8 π between harmonic order 13 and 27. For harmonic order 19, the relative phase δ is nearly $\pi/2$. (Since we do not measure the handedness of the beam, there is an ambiguity in the sign of δ.)

As pointed out in [68], for a plane wave recombination dipole, the phase difference between the y and x components of the harmonic emission is either 0 or π. Thus, the high harmonic emission should be linearly polarized. Moreover, the position of any phase jump arising, for example, from a quantum interference effect should depend on the molecular orientation angle. Using a recently demonstrated molecular interferometry technique to measure the phase of the harmonic emission from N_2 during a rotational revival with parallel polarized pump and probe beams, we found that the phase of the harmonic emission from N_2 does not depend on orientation of the molecule, and that there is no angle-dependent intensity minimum for harmonic orders 19 – 31. Therefore, the observed significant but smooth variation in relative phase difference over 8 harmonic orders cannot be fully explained by assuming a plane wave recombination dipole. Our results possibly indicate a breakdown of the plane wave approximation, which could result in a delay between the oscillating dipole in the y and x directions. In principle, both the signature of the HOMO on the ionized electron wave packet and the influence of the Coulomb potential on the recombination process could generate a phase delay between the dipoles corresponding to the two components of polarization [74]. The significant difference between N_2 and CO_2 molecules clearly are related to their different molecular orbitals. The contribution from the lower-lying molecular orbitals is another potential reason for the observed ellipticity [63]. Thus the observed HHG ellipticity in N_2 may reflect nontrivial electronic dynamics.

In summary, we have uncovered unexpected polarization properties of high harmonic emission from N_2 and CO_2 molecules that have broad implications for the theory of molecules in strong fields. First, we found that elliptically polarized harmonics can be emitted by molecules and that the relative phase between the y and x components of the harmonic field strongly depends on the harmonic order.

Second, although N_2 is a simple diatomic molecule and was used for molecular tomography experiments, the 3-step model cannot completely describe the behavior of harmonic emission from N_2. Combined with recently developed techniques for measuring the phase of HHG from molecules [55, 66], we have made a significant step forward in a complete characterization of harmonics from simple molecules. For N_2, as discussed in the previous chapter, the phase of the parallel component does not depend on the molecular orientation. Although it is difficult to make a direct measurement of the dependence of the phase of the perpendicular HHG component on the molecular orientation due to the small flux, it would be surprising if the phase of the perpendicular components depend on the molecular orientation. Since our measurement show that the relative phase between the parallel and perpendicular HHG component depends on the harmonic order N_2, we conclude that the recombination phases of parallel and perpendicular HHG components of N_2 depend on the harmonic order in a complex way, but these phases do not depend on the molecular orientation.

Finally, our results present a straightforward and efficient way to generate circularly polarized harmonic beams for applications in molecular and materials science.

5.2 Polarization-resolved characterization of HHG emission from aligned molecules with elliptical polarized fundamental light

HHG from atoms with elliptical polarized driven laser have been studied intensively [75, 76, 77, 78]. The ellipticity of the fundamental laser can steer the electron wave packet, which causes a lateral shift of the return electron wave packet away from the parent ion and reduces the probability of recombination. The HHG yield decays very quickly with the increasing ellipticity of the driven laser, and usually, the fundamental ellipticity dependence of HHG is a Gaussian shape and centers at zero ellipticity. Ref. [79] attributed the observed deviation from Gaussian shape of the threshold harmonics to the interaction of the ionized electron with the Coulomb potential. The ellipticity can also change the trajectory and recollision angle of the electron in the continuum.

The harmonics generated by an elliptical polarized fundamental IR laser also have a complicated polarization state, due to the existence of a perpendicular component and the nontrivial phase between the perpendicular and parallel components. A previous measurement revealed that the HHG was elliptically polarized and that the long axis of the polarization rotates away from the long axis of the fundamental laser ellipse [80, 81, 71]. The direction of this rotation depends on the harmonic order.

The ellipticity dependence of the HHG has been used recently for generating a single attosecond pulse with polarization gating techniques [82, 83], where a fundamental laser pulse with time-dependent polarization was used to generate harmonics. A few laser cycles in the center of the pulse have linear polarization, which generate harmonics efficiently. The time-dependent polarization gradually becomes circular on the leading and trailing edge of the pulse, where the HHG yield is suppressed.

The trailing and leading edges of the generated EUV pulse are generated by a slightly elliptically polarized fundamental laser, therefore, they are not linearly polarized. It is interesting to characterize the perpendicular and parallel components separately of these pulses. Thus we can evaluate the importance of the perpendicular components when we apply the attosecond pulses generated by polarization gating techniques to polarization-sensitive applications such as photoelectron spectroscopy.

Some experiments have tried to measure the fundamental laser ellipticity dependence of the HHG from aligned molecules. The ellipticity dependence of HHG from CO_2 and N_2 has been measured for two special cases, aligned or anti-aligned molecules in Ref. [84]. Y. Mairesse et. al. [85] performed a more general measurement for several angles between pump and probe (long axis of the polarization ellipse) polarizations.

In this section, we present a polarization-resolved measurement of HHG from atoms and aligned molecules generated by an elliptically polarized laser light. Our elliptical polarized fundamental light is generated by a combination of a rotatable half-wave plate and a fixed quarter-wave plate. The long axis of the fundamental ellipse remains along the S polarization of the gold mirror polarizer when the HHG component parallel to the long axis of the fundamental ellipse is measured; and along the P polarization of the gold mirror polarizer when the HHG component perpendicular to the long axis of the fundamental ellipse is measured.

We present the data for fundamental ellipticity dependences of the perpendicular ($\perp$) and parallel ($\|$) HHG components of Ar, and N_2. For the parallel HHG component from Ar, we observe same behavior as in Ref. [86] that the higher order harmonics decrease faster with increasing ellipticity than low order harmonics. As shown in Fig. 5.7, there is no perpendicular HHG component at zero ellipticity. The perpendicular HHG components are maximized at a nonzero ellipticity, and further increasing of the ellipticity will finally decrease the HHG yield.

For N_2 molecules, if the angle between the pump and probe polarization is neither 0° nor 90°, as shown in Figs. 5.8 and 5.9, we observe that both parallel and perpendicular HHG components do not peak at linear polarization of the driving laser, but rather peak at a small positive or negative ellipticity. The sign and magnitude of this ellipticity depend on the molecular orientation. An interesting feature is that the sign of this ellipticity is opposite for parallel and perpendicular HHG components. For example, when the angle between pump and probe pulses is -50°, the maximum of the parallel component of the 15th harmonic is located at a slightly negative ellipticity, -0.017, similar to the result of [85]. While the maximum of the perpendicular HHG component is located at a much larger positive ellipticity 0.08.

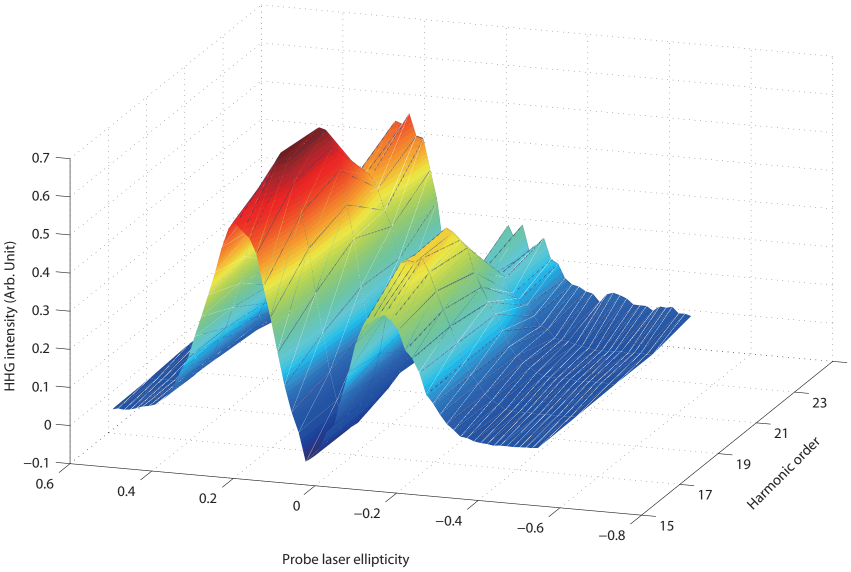

Figure 5.7: Perpendicular HHG components from Ar atoms for harmonic order 15-23 versus the fundamental ellipticity.

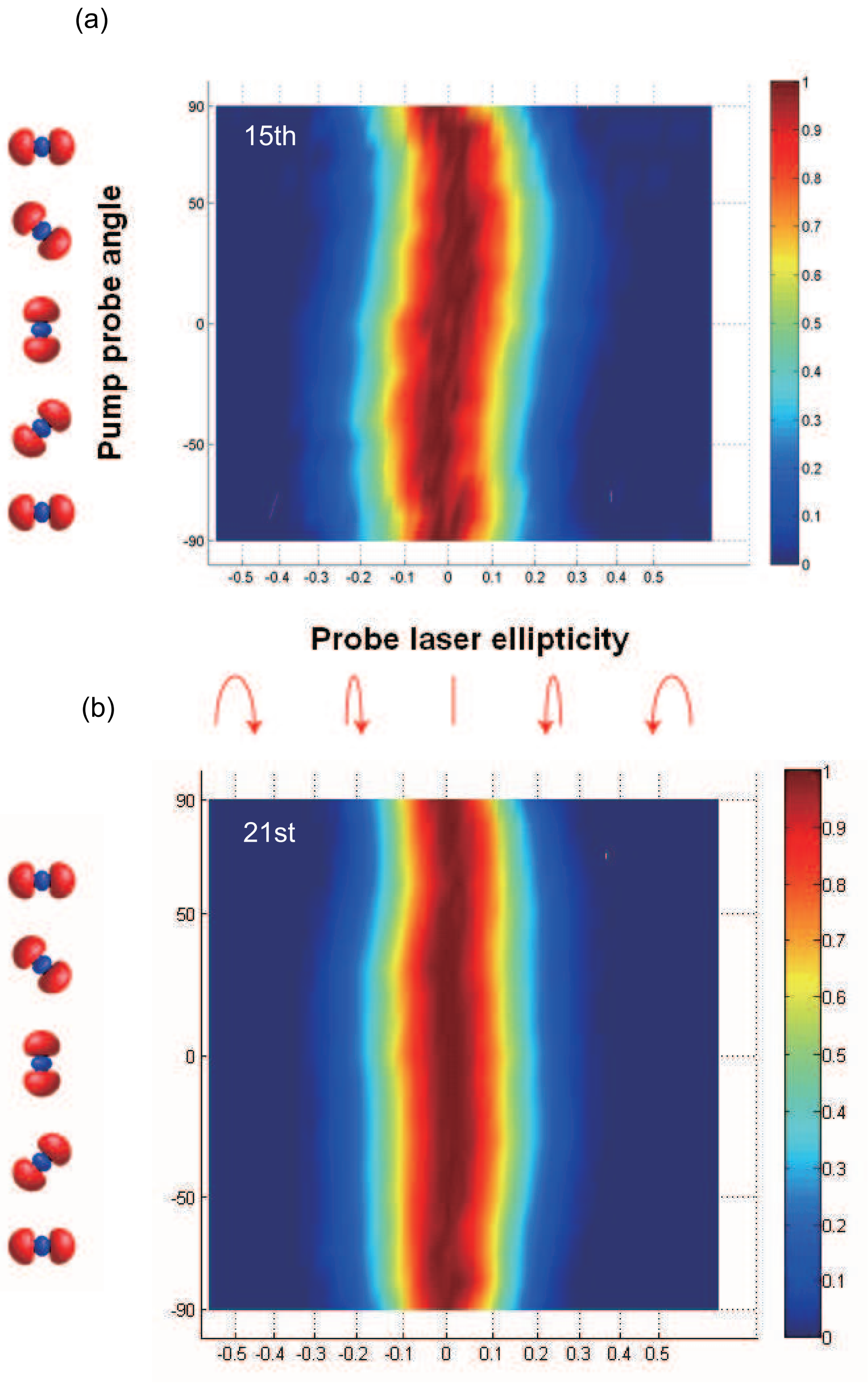

Figure 5.8: 2D color map of parallel HHG components of 15th (a) and 21st (b) harmonics from N_2 molecules as a function of the fundamental laser ellipticity and molecular alignment angle. These data have been normalized to the maximum value of each harmonic.

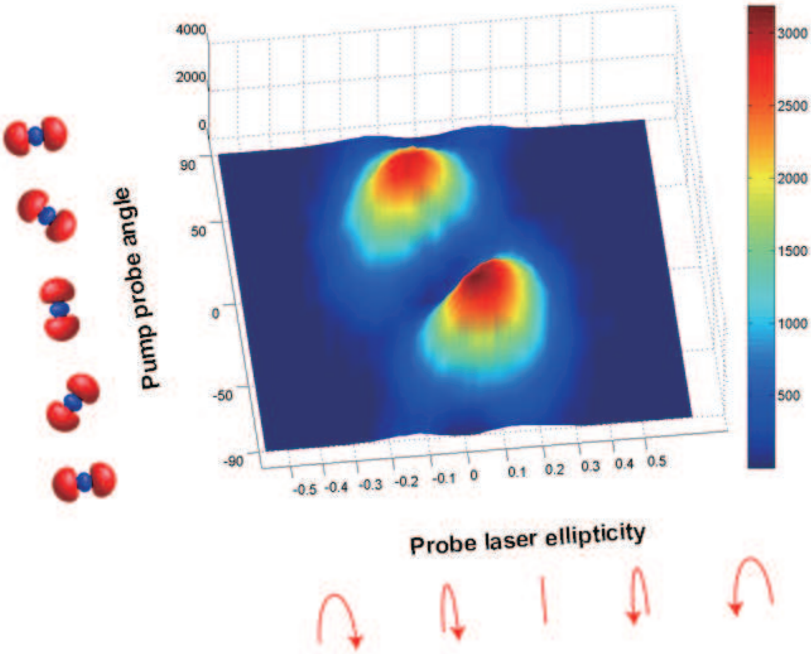

Figure 5.9: 2D color map of perpendicular HHG component of 21st harmonic from N_2 molecules as a function of the fundamental laser ellipticity and molecular alignment angle.

In summary, the HHG from aligned molecules using an elliptical polarized driven laser offers more information than the HHG using a linearly polarized laser. However, to fully understand the data of these experiments, a more sophisticated model is required.

Chapter 6

Real Time Monitoring of Molecular Dynamics with HHG

The experiments discussed in the last two chapters have confirmed the sensitivity of HHG to the static electronic structure of aligned molecules. Scientists are also interested in studying the dynamics of molecules with HHG. The attosecond time-scale electron recollision process that underlies high harmonic generation shows great promise as a probe of molecular dynamics, particularly so if it can be applied to complex polyatomic molecules.

Recently, two experiments were performed to investigate the effects of nuclear motion on HHG. Baker et al. studied the harmonic generation from H_2 and D_2 molecules [87]. They showed that the ratio between the HHG from H_2 and D_2 molecules depends on the harmonic order, which can be explained by the faster nuclear motion of the protons in H_2 during the ionization and recombination events of HHG. The recollison electron acts as the probe for the nuclear motion, that is initiated by the ionization. The different recollision times for different harmonic orders serve as the pump probe time delay.

We performed another experiment on SF_6 molecules, which is more similar to the conventional pump probe experiments. In this effort, we used the pump pulse to excite the vibration motion in SF_6 molecules through impulsive stimulus Raman processes, which excited three of six Raman active modes in the SF_6 molecules [88]. The modulation of the HHG yield was small in this experiments and the result can be explained by vibrational wave packet beating [89].

In this chapter we show that high harmonic generation can reveal coupled electronic and nuclear dynamics in polyatomic molecules [90]. By exciting large amplitude vibrations in the N_2O_4, we show that tunnel ionization accesses the ground state of the ion at the outer turning point of the vibration, but populates the first excited state at the inner turning point. This state switching mechanism is manifested as bright bursts of high harmonic light emitted mostly at the outer turning point of the vibration. Theoretical calculations attribute the large modulation to suppressed emission in the first excited state of the ion. More broadly, the result imply that high harmonic generation and strong field ionization in polyatomic molecules undergoing bonding or configurational changes involve participation of multiple molecular orbitals

6.1 Vibration in N_2O_4

In polyatomic molecules, electronic and vibrational excitations can couple and dynamically redistribute both energy and charge during dynamic processes. Due to the importance of these dynamics in chemical and biological systems, the capability to probe dynamics in large polyatomic molecules is ultimately a requirement for any broadly useful spectroscopy or dynamical imaging technique. Time-resolved photoelectron spectroscopy (TRPES) is a weak field (perturbation regime, laser intensity$<10^9$ W/cm^2) method that can uncover these dynamics [27, 91, 92]. In TRPES, the molecule is first excited by a pump pulse. A time-delayed probe pulse then projects the complex evolving wave packet onto the molecular ionization continuum, and the outgoing electron is analyzed as a function of pump-probe delay. The cation electronic states and their associated electronic continua, and the vibrational structure of the ionization continuum, are both used as a 'templates' for projecting out the electronic and vibrational components of the complex wave packet. This evolving projection onto multiple electronic continua permits the disentangling of electronic and vibrational dynamics during non-adiabatic processes in polyatomic molecules [93].

High harmonic generation (HHG) is a strong field (non-perturbation regime, laser intensity $>10^{12}$ W/cm^2) process [94, 95]that is closely related to photoelectron spectroscopy. In atoms, HHG is successfully described by an adiabatic, single active electron (SAE) model involving three steps: strong-field tunnel ionization, propagation of the continuum electron in response to the laser field, and finally recombination of the electron with its parent ion resulting in emission of a high energy photon [12, 13, 14]. However, in the case of HHG from a polyatomic, the physics is more complex due to the many-body electronic structure of polyatomic molecules and the existence of ro-vibrational and non-adiabatic dynamics. The recombination matrix element for the HHG process and the photoionization matrix element of the photoabsorption process are the same since these steps are inverse to each other. Therefore, the multiple electronic continua relevant to probing complex polyatomic dynamics via TRPES must also play a role when HHG is used to probe these dynamics. The use of HHG as a probe has two potential advantages over TRPES: first, the ability to access attosecond time scale processes, and second, the ability of HHG to simultaneously probe with many photon energies. However, until recently, only the highest occupied molecular orbital (HOMO) has usually been considered to explain both strong field ionization and high harmonic emission. This simplification comes from the adiabatic and single active electron approximations that underlie theories of tunnel ionization in atoms and molecules (ADK and molecular ADK) [18, 26]) and that are integral to the three-step model of HHG [12, 13]. In polyatomic molecules however, both approximations can fail dramatically - particularly so when the molecule is dynamically evolving, as we show in this work. Strong field ionization can become both non-adiabatic and involves multi-electron excitations [96, 97]. Theoretical efforts to relax the single active electron approximation are being attempted in order to address this issues by introducing multi-electron effects in the recombination step of HHG [39, 98].

Past work has investigated HHG from rotationally aligned molecules as a potential probe of static molecular structure [37, 55], since the emission strength depends on the molecular orbital nature of the ground electronic state and its alignment with respect to the laser field. Recent, related work has also used the photoelectrons released and rescattered during the strong field ionization process to recover the static orbital structure of simple diatomic molecules [99]. High harmonic generation also has been used as a probe of simple dynamics in molecules where, for example, the molecular structure was slightly changed without any bond reorganization. Past work has shown that the high harmonic generation process is sensitive to simple vibrational dynamics in a molecule, even to modes that cannot readily be probed optically [88, 89]. The rearrangement of atoms within a molecule during the HHG process can also be inferred by comparing HHG spectra of isotope-substituted molecules [87]. Chemical dynamics, however, involve large amplitude motions. HHG experiments have yet to succeed in observing and understanding large-amplitude structural rearrangements within a polyatomic molecule, where the simple assumptions are unlikely to remain valid because of dramatic and evolving changes in the ionization/recombination dynamics.

Here we successfully apply high harmonics generation as a time-resolved probe of chemical dynamics in a polyatomic molecule. By exciting a large amplitude vibrational wave packet motion in the ground state of a dinitrogen tetraoxide (N_2O_4) molecule, we observe large modulations in harmonic yield. We discover that at the outer turning point of the vibration, tunnel ionization populates the ground state of the ion (HOMO$^+$ A_g continuum), which has a large recombination dipole and therefore a high probability for harmonic emission. In contrast, at the inner turning point, the first excited state of the ion is populated by tunnel ionization (i.e. the (HOMO-1)$^+$ B_{2g} continuum). This channel has a small recombination cross-section and thus suppresses the harmonic emission.

6.2 HHG probing of N_2O_4 dynamics

N_2O_4 is a dimer of NO_2, with a dissociation energy of $\sim$0.65 eV. N_2O_4 can be present in significant quantities (80%) even at room temperature. The molecule has D_{2h} symmetry and six Raman-active vibrational modes, the strongest being the low frequency N-N symmetric stretch (265 cm^{-1}, 0.03eV). By non-resonantly exciting this mode via impulsive stimulated Raman excitation (ISRS), we can generate a large amplitude ground state vibrational wave packet along the N-N coordinate. This large amplitude motion samples a broad range of ionic configurations, leading to the participation of more than one molecular ionization continuum in the HHG process, as illustrated in Fig. 6.1.

In our experiment, ultrashort laser pulses from a Ti: Sapphire laser system (800 nm, $\sim$30 fs, 4 mJ, 1 kHz) are split into pump (25%) and probe (75%) pulses. The pump pulse is focused onto a N_2O_4 gas jet (backing pressure $\sim$700 torr) at an incident intensity of 2 x 10^{13} W/cm^2, to impulsively excite ground-state vibrations in the molecule. The time-delayed probe pulse is focused to an intensity of $\sim$2 x 10^{14} W/cm^2 to generate high harmonics from the vibrationally excited molecules. The relative polarizations of the pump and the probe pulses are controlled using a half-wave plate in the pump beam path. The generated harmonics are then spectrally separated using a EUV spectrometer (Hettrick Scientific) and imaged onto an EUV-sensitive CCD camera (Andor Technology). The ion signal can also be collected using a mass spectrometer.

Fig. 6.2(A) shows the experimentally observed high harmonics, from orders 19 to 27, as a function of pump-probe time delay. Lower order harmonics were not observed because of absorption by the 0.2 μm thick aluminum filter used to reject the pump laser light. Even in the raw data, a time-dependent oscillation of the harmonic yield

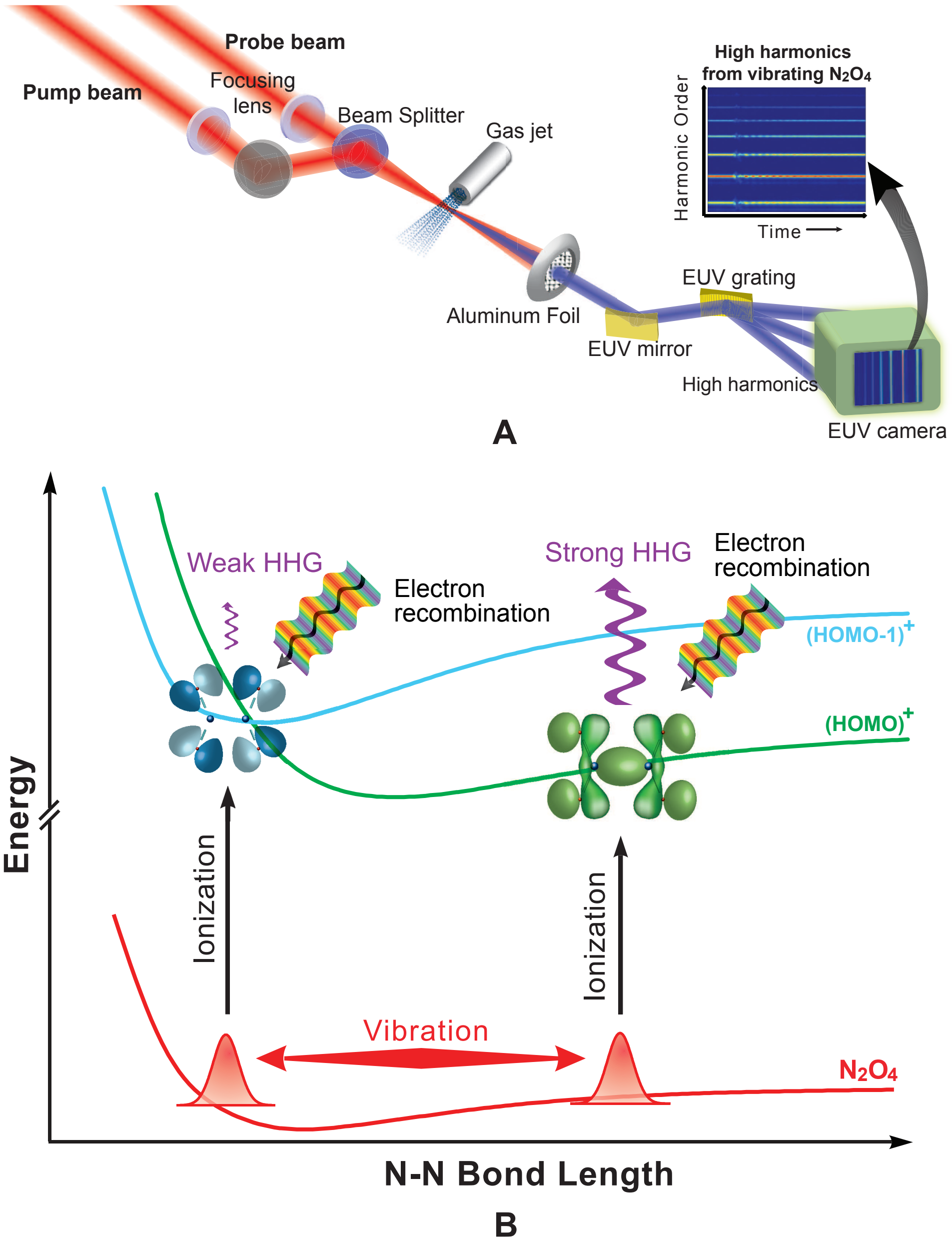

Figure 6.1: (A) Experimental setup. N_2O_4 molecules from an effusive nozzle are excited and probed using ultrafast 800 nm laser pulses. The pump pulse intensity and duration are chosen to impulsively excite, but not ionize or dissociate, N_2O_4. A more intense, collinear, probe pulse (2×10^{14} W/cm^2, 30fs) generates harmonics from the vibrationally-excited dimer. (B) Schematic of the experiment showing potential energy curves for N_2O_4 as a function of N-N bond length. Figure adapted from [90].

is apparent. For all the harmonic orders observed, the time dependence of the HHG emission(Fig. 6.2(C)) shows several common characteristics: a sudden drop in HHG yield when the sample is initially excited at time-zero, followed by strong oscillations in the HHG yield imposed on a slowly rising baseline. The strong suppression of harmonic generation at time zero is a result of coherent effects due to the overlap of the pump and probe. Strong oscillations in the harmonic yield are present for both parallel and perpendicular polarizations of the pump and probe (Fig. 6.2).

The origin of the strong oscillations in the harmonic yield becomes apparent if we apply a discrete Fourier transform to these data. A single peak at 255±10 cm^{-1} appears in the transform spectra (Fig. 6.2 (C), 6.2 (D) inset). This frequency corresponds unambiguously to the Raman active 265 cm^{-1} N-N stretch mode of N_2O_4. Given the ISRS pump mechanism employed here, the initial motion of the vibrational wave packet will be repulsive, with the outer turning point occurring one quarter period after the pump pulse. To verify the exact timing of the emission, we used argon gas in the same setup, since HHG from Ar exhibits a transient only at time-zero due to coherent effects. We thus verified that in N_2O_4, a large peak in HHG yield appears at 170±10fs—in very good agreement with T+T/4 (T=130fs: vibration period) for the N-N stretch mode of N_2O_4. This timing clearly indicates that harmonic yield peaks at the outer turning point of the N-N stretch vibration. The first peak in emission at T/4 (∼35 fs) is less obvious, likely due to pump-probe overlap that suppresses the signal.

6.3 Monitoring the ionization yield

We also measured the ionization yield as a function of pump-probe delay (see Fig. 6.3). The yield of $N_2O_4^+$ is approximately the same at the inner and outer turning points. This finding shows that at the inner turning point, the molecule is ionized but harmonic emission is suppressed. Hence, ionization alone (i.e. modulation

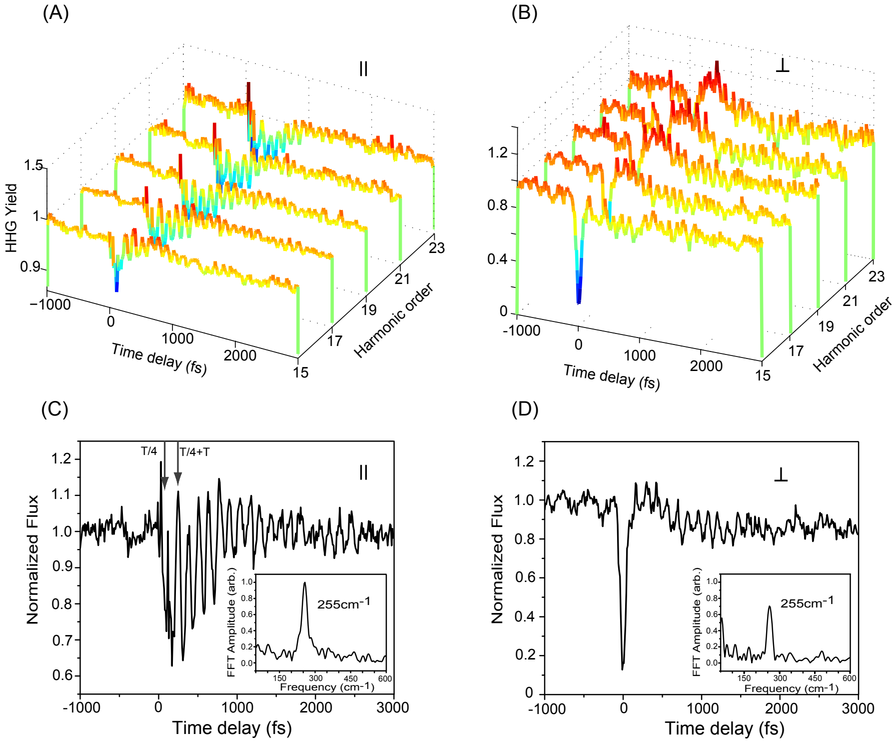

Figure 6.2: Harmonic yield vs. pump-probe delay using (A) parallel ($\parallel$) and (B) perpendicular ($\perp$) pump and probe polarizations. Harmonic yield is normalized to the harmonic emission at the negative pump-probe delay. Time-dependent 21st harmonic yield for (C) parallel and (D) perpendicular polarizations. The insets in (C) and (D) show the Fourier transform, dominated by the N-N stretch mode at 255cm^{-1}. Figure adapted from [90].

of the ionization potential or rate due to the vibrational motion) cannot account for the observed large modulation in HHG yield. Another possibility for the suppression of HHG at the inner turning point is a contribution from a different electronic continuum, one that has smaller recombination amplitudes for HHG. In Fig. 6.7 we plot the measured intensity dependence of the HHG peak-to-peak modulation depth for different harmonic orders. The modulation depth increases with increasing laser intensity and decreases with increasing harmonic order.

Fig. 6.3 plots the measured time-dependent ion yield after strong field ionization of vibrationally-excited N_2O_4. For these data, the gas backing pressure was reduced to 100 torr to avoid strong space charge effects. The ${N_2O_4}^+$ and ${NO_2}^+$ ion yields do not exhibit any obvious oscillation structure and are therefore not plotted. Only the yield of O^+ was observed to be modulated by the vibrational excitation.

The spike near time zero is due to a coherent field effect. Moreover, the modulation depth of the O^+ yield is $<2\%$, which is much less than the 20 to 30% HHG yield modulation. The observed small modulation in all ion yields agrees well with the calculated results of the ionization structure factors, if both the A_g and B_{2g} ionization continua are contributing to the ion yield. In particular, since the ${N_2O_4}^+$ ionization yield is approximately the same at the inner and outer turning points, ionization alone (i.e. modulation of the ionization potential or rate due to the vibrational motion) cannot account for the observed large modulation in HHG yield. Moreover, our findings show that at the inner turning point, the molecule is ionizing but harmonic emission is suppressed. These data can be explained by a contribution from a state that is mostly dark for HHG emission at the inner turning point.

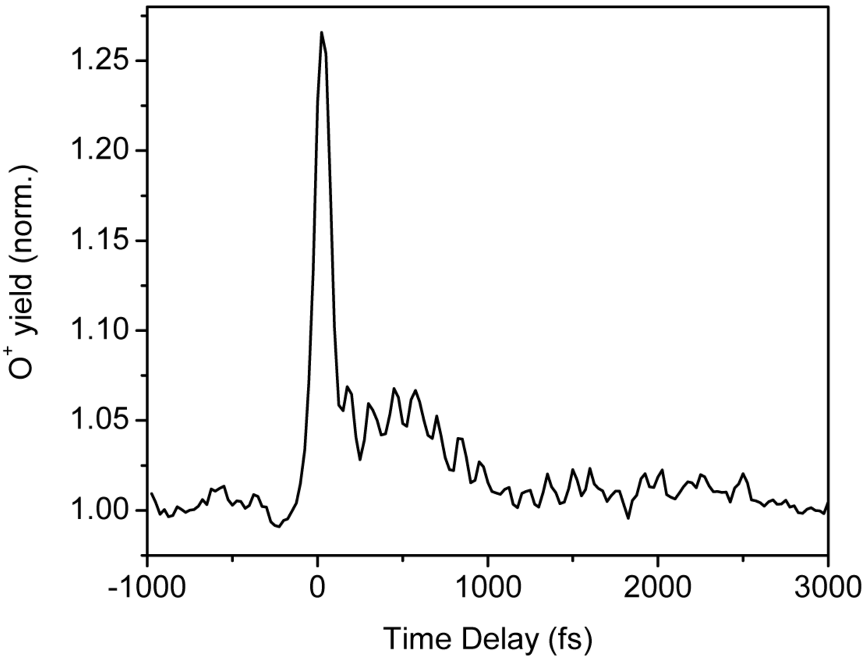

Figure 6.3: Time-dependent O^+ yield from N_2O_4 after strong field ionization. The modulation depth of the O^+ yield is <2%, which is much less than the 20-30% modulation in the HHG yield. Figure adapted from [90].

6.4 Ruling out NO_2 participation by interferometric measurement of the phase change in HHG from vibrating N_2O_4

Because a small portion of NO_2(<20%) co-exists with N_2O_4 in our sample, we had to eliminate the possibility that heterodyne mixing of harmonic emission from N_2O_4 and NO_2 contributed to the observed modulation, . If the phase of harmonics emitted from N_2O_4 at the inner turning and outer turning points were different, interference between emissions from NO_2 and N_2O_4could contribute to the modulation observed. Such phase variations could arise from intrinsic phase changes due to the differing ionization potentials at the inner and outer turning points of the vibration, or from different generating ion states, i.e. A_g and B_{2g}. Only the latter is consistent with our proposed mechanism. Using an interferometry technique demonstrated recently [55], we monitored the fringe pattern generated by interfering HHG from vibrationally excited and unexcited N_2O_4 molecules. No phase change in HHG emission was observed during the vibration, within the sensitivity limit of our measurements. This null result is a clear indication that heterodyne mixing does not contribute significantly to our signal.

If the phase of the harmonic emission from N_2O_4 at the inner turning and outer turning points of the vibration were different, interference between emissions from NO_2 and N_2O_4 could contribute to the observed HHG modulation, since a small fraction ($<$ 20%) of NO_2 will be present in the gas. Such phase variations could arise from intrinsic phase changes due to the differing ionization potentials at the inner and outer turning points of the vibration, or from different generating ion states, i.e. A_g and B_{2g}. To rule out this possibility, we implemented a double foci interferometry measurement [55] to monitor the fringe pattern (i.e. phase difference) between HHG from vibrationally excited and unexcited N_2O_4 molecules. The result is plotted in Fig. 6.4. No phase change in HHG emission from N_2O_4 was observed during the vibration (Fig. 6.4(A)), within the sensitivity limit of our measurements. This null result is a clear indication that heterodyne mixing between NO_2 and N_2O_4 does not contribute to our modulated HHG signal. In contrast, when we implemented the same interferometry technique to compare the phase of HHG from rotationally aligned and unaligned CO_2 molecules during a rotational revival, a clear fringe shift corresponding to a π phase shift can be observed for harmonic order 31 (Fig. 6.4 (B)).

6.5 Theoretical calculation

Our collaborators at National Research Council of Canada carried our the following calculations for us. For this calculation, the electronic structure was calculated using a modified aug-cc-pVTZ basis set, with f-type basis set functions deleted. Structural parameters for the neutral N_2O_4 ground state and the cation ground and electronically excited states were optimized within the D_{2h} point group at the complete active set self-consistent field (CASSCF) level, with 16 molecular orbitals included in the active space. This active space includes 13 occupied and 3 virtual orbitals. The overall composition of the active space was ${a_g}^3$ ${a_u}^1$ ${b1_g}^1$ ${b1_u}^3$ ${b2_g}^2$ ${b2_u}^2$ ${b3_g}^2$ ${b3_u}^2$. At this level, structure of N_2O_4 is in a good agreement with experimental results: r_{N-N}=1.81Å (expt: 1.78), r_{N-O}=1.17 Å (expt: 1.19), α_{ONO}=134° (expt: 135). The effects of dynamical correlations were treated with single-point second-order multi-reference perturbation treatment (MCQDPT2), as implemented in GAMESS-US. Using the above parameters, potential energy curves were calculated assuming adiabatic relaxation of all structural parameters in neutral N_2O_4, other than the N-N bond length. For the N_2O_4 cation states, we used the instantaneous nuclear configuration of the optimized N_2O_4 neutral as a function of N-N bond length. The rationale for this is that during $\sim$1 fs time scale electron rescattering process of HHG, the molecular structure does not have time to relax.

Vibrational wavefunctions were obtained by numerical solution of 1D effective-

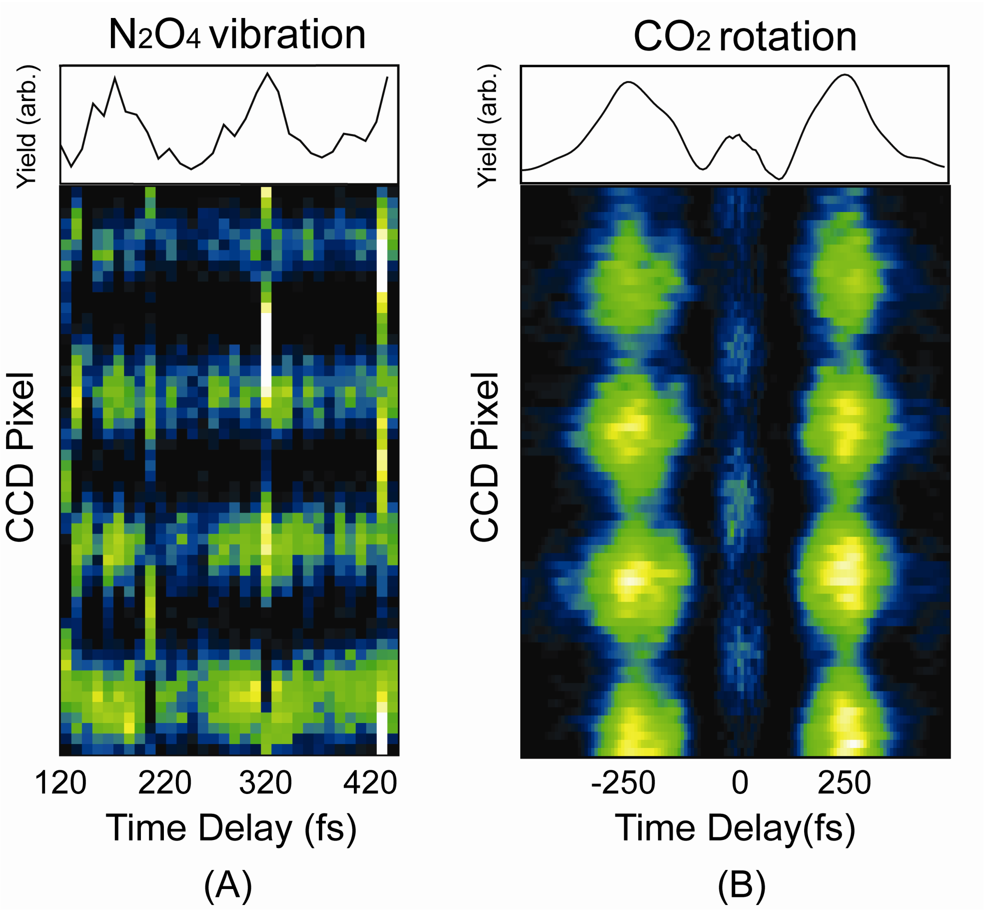

Figure 6.4: Interference pattern obtained by combining HHG emission (15th order) from vibrationally excited and unexcited N_2O_4. No obvious phase shift was observed between the HHG at the inner and outer turning points. The top panel plots the time-dependent HHG yield modulation by vibrations in N_2O_4. (B) For comparison, interference pattern obtained by combining HHG emission (31st order) from rotationally aligned and unaligned CO_2, during a rotational revival. Near 0fs (CO_2 aligned) the HHG phase is shifted 180° relative to that of HHG at -250fs and 250fs (CO_2 anti-aligned). The top panel plots the time-dependent HHG yield modulation by a rotational revival in CO_2. Time zero is at the center of the third quarter revival. Figure adapted from [90].

diatom vibrational Hamiltonian, discretized on a 1.2Å<r<5Å grid. The effective mass of the system was scaled by a factor of 0.7 to match the experimental fundamental vibrational frequency in the neutral molecule. The structural factors were calculated as:

$$f(r) = \sum_d 2 \left| \sum_s a\left(\epsilon_d - \epsilon_s\right) \langle \varphi_d \left| \varphi_s \right\rangle \langle \varphi_s \left| \psi\left(r\right)\right\rangle \right|$$

where φ_s (φ_d)and ϵ_s (ϵ_d) are vibrational wave functions and energies of the neutral (cation), and ø(r) is the initial vibrational wave packet (0.3Å FWHM Gaussian centered at r). All bound vibrational states of the neutral are included in the summation. For the cationic surface, the summation is over all states, both bound and continuum. The energy-dependent part of the ionization amplitude was taken as (atomic units)

$$a\left(\varepsilon\right) = \varepsilon^{1.5/\sqrt{2\varepsilon}-0.25} \exp\left(-\left(2\varepsilon\right)^{1.5}/(3E)\right),$$

with E being the characteristic strength of the ionizing electric field (E ~0.05 a.u.). Approximation of the initial wave packet by a Gaussian ignores the anharmonicity of the N_2O_4 vibration and will not account for the real time evolution of the vibration wave packets. But it is reasonable as a model of the R-dependent Franck-Condon factors for our experiment.

For N_2O_4 molecules, ISRS in the strongly anharmonic ground state potential results in large vibrational amplitudes, up to 0.6 Å (i.e. from ~1.6 to 2.2 Å). To understand the effect of this large excursion on the HHG process, we performed ab initio calculations of the structure of both the N_2O_4 neutral and cation states. The calculated potential energy curves for the ground state of neutral N_2O_4, the ground state of the cation $N_2O_4^+$ (A_g) and the first excited state of the cation (B_{2g}) are shown in Fig. 6.5 (A). The equilibrium bond length of the A_g cation has a substantially elongated N-N bond (2.21Å vertical, elongating to 2.25Å upon complete optimization). This bond lengthening is a consequence of HOMO ionization to the cation ground electronic state removing a bonding electron. In contrast, ionization of the (HOMO-1) to the B_{2g} excited state of the cation leaves the N-N bond relatively unchanged (1.75Å vertical, increasing to 1.80Å upon relaxation). This picture is confirmed by the previously reported He(I) photoelectron spectra of N_2O_4 which show a delayed onset and long progression to the cation ground electronic state, compared with sharp lines and very limited progression to the cation first excited state [100].

The significant difference in bond length for the ground and excited states of the cation implies a strong bond-length dependence of the structural (Franck-Condon) factors for tunnel ionization: the A_g ground state is expected to be favored at longer N-N distances, whereas the B_{2g} excited channel benefits when the N-N bond is compressed. To quantify this argument, we performed a model calculation of the energy-dependent contribution to the structural ionization factors using the potential energy surfaces shown in Fig. 6.5 (A). (see also supporting text) The results (Fig. 6.5 (B)) show that for N-N bond lengths below 1.7Å, structural factors favor ionization to the B_{2g} excited state. At longer bond lengths, ionization to the A_g ground state of the cation is favored, with the corresponding structural factor increasing up to R_{N-N}=2.3Å. Thus, due to the contribution of two ionization channels, the ion yield of $N_2O_4^+$ is not expected to change significantly during the vibration, consistent with experiment.

6.6 Saturation due to the depletion of ground state

At the relatively high laser intensity used here, saturation due to the depletion of the neutral N_2O_4 population may become an important factor. In this regime, the total number of emitters of each type is determined by the ratio of the ionization rates for each species, rather than by the individual rates. The calculated ratio of the A_g/B_{2g} structural factors in N_2O_4 increases monotonically with R_{N-N}, with the B_{2g} state as the preferred channel at short bond lengths, whereas the A_g state dominates when the bond is elongated. Thus, the relative importance of the two channels remains the same,

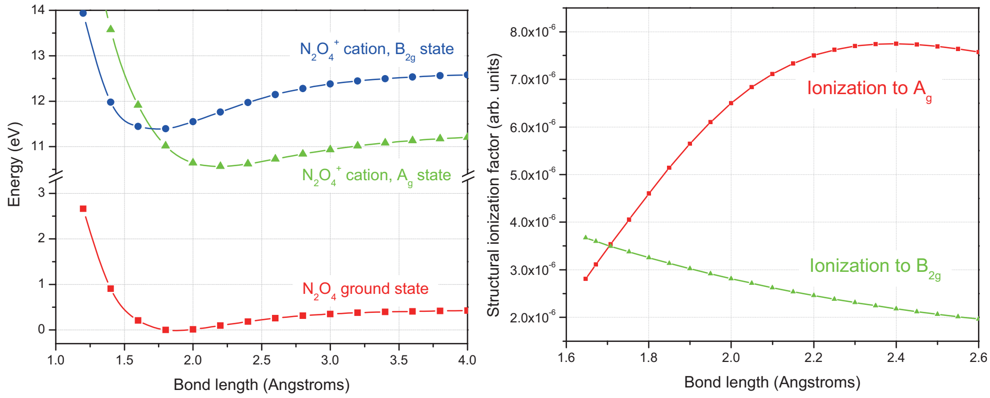

(A) (B)

Figure 6.5: (A) Calculated MCQDPT2//CASSCF potential energy curves for neutral N_2O_4 (bottom) and the first two cation states (top). (B) Structural factors for ionization calculated at different bond lengths. At the short bond length, ionization favors the first excited state of the ion (B_{2g} continuum) whereas the ground A_g continuum dominate at long bond lengths. Figure adapted from [90].

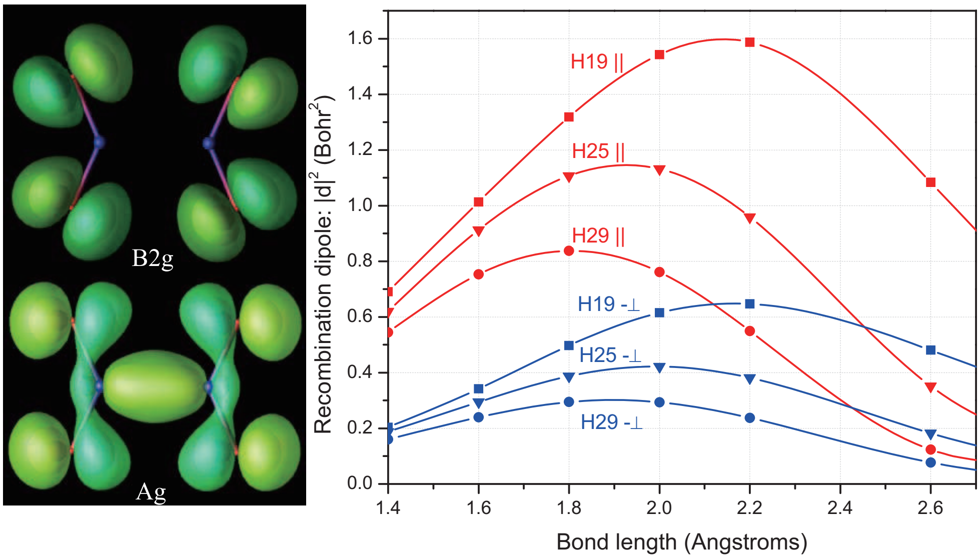

(A) (B)

Figure 6.6: (A) Dyson orbitals corresponding to ionizing to the Ag cation state and the B_{2g} cation state. The calculated equilibrium bond lengths for the neutral, A_g and B_{2g} cation states are 1.808 Å (exp. 1.756Å), 2.248 Å and 1.8 Å, respectively. (B) Recombination dipoles of harmonics at different bond lengths for parallel (red, $\|$) and perpendicular (blue, $\perp$) pump-probe polarization. Figure adapted from [90].

even in the presence of saturation. The observed increase in modulation depth with increasing laser intensity (Fig. 6.7), is in good agreement with this two-continuum-states model. If the HHG process involved emission only from a single continuum transition, a decreasing modulation depth with increasing laser intensity should be observed because ionization saturation at the outer turning, which is reached at the lower laser intensity due to lower ionization potential, will lead to reduced modulation depth.

6.7 Origins of HHG suppression at the inner turning point

To calculate the recombination dipoles, the amplitude of the ionization or recombination process within a given ionization channel is determined by the 1-particle dipole matrix element between the Dyson orbital and the continuum wave function at a given energy. We treat the continuum wavefunctions in the strong-field eikonal-Volkov approximation [40], with the molecular potential included in the Hartree approximation. The residual non-orthogonal contributions in the continuum wavefunction are treated with the exchange corrections of ref. [39]. The recombination dipoles are coherently averaged over relative orientations of the molecular frame and the probe pulse. The angular distribution of the N-N bond in vibrationally excited N_2O_4 molecules created by pump pulse was assumed to be $\cos^2\theta$. The final results are only weakly sensitive to the detailed shape of the distribution.

For the propagation of the liberated electron in the continuum, the long-range part of the molecular potential is not significantly influenced by intramolecular vibrations, and no additional modulation of the HHG signal is expected. Therefore, we now consider the electron recombination step. To this end, we calculated the overlap between the N-electron wave function of the neutral species, and the (N-1)-electron wave function of the ion – the Dyson orbital. This calculation captures the change in the electronic structure of the molecule upon electron removal or recombination. Dyson orbitals for

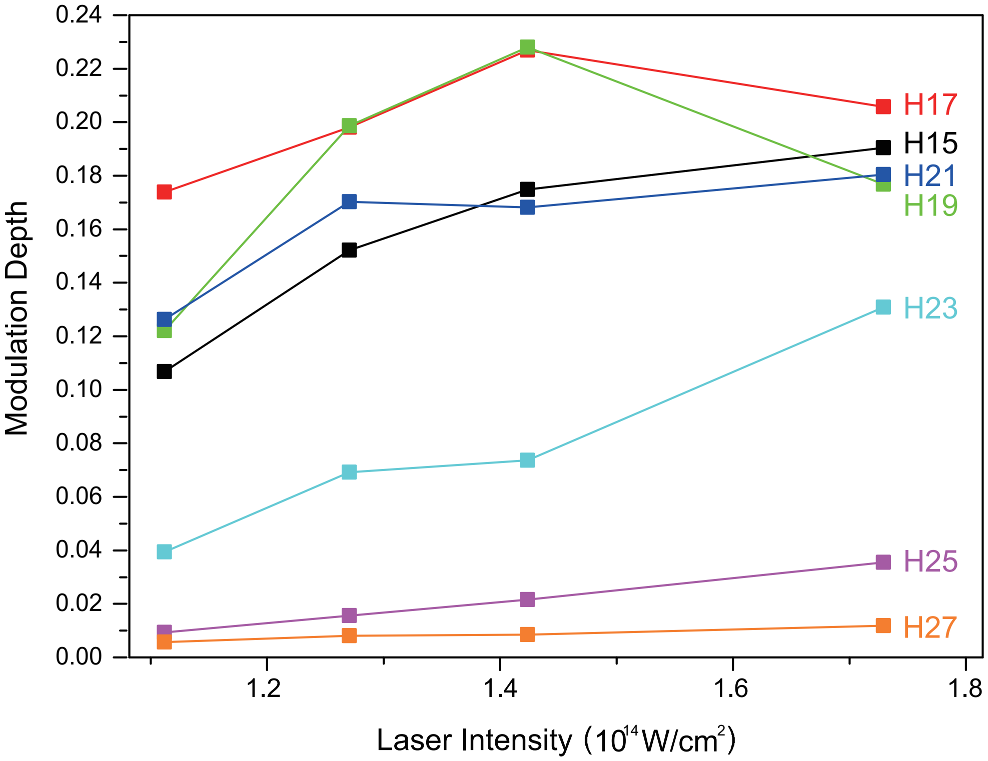

Figure 6.7: Laser intensity dependence of the vibrational modulation depth for different harmonics, showing an increasing modulation depth with increasing laser intensity. Figure adapted from [90].

the two significant ionization channels, calculated at the equilibrium geometry of the neutral species, are shown in Fig. 6.6(A). The final recombination dipoles for the A_g channel as a function of both their N-N bond separations and harmonic order are shown in Figure 6.6(B). As a result of the presence of nodal planes along all principal directions, the excited ion state channel (B_{2g}) is suppressed. Nodal planes both decrease recombination matrix elements and reduce recollision probability.

The radial dependence of the calculated recombination dipoles $\mathbf{d}$ is sensitive to the harmonic order. At low harmonic orders (H17 to H21), the matrix elements for the parallel pump/probe orientation increase with the N-N bond length, leading to a doubling in harmonic radiation intensity at R_{N-N}=2.1Å ($|\mathbf{d}_{H19}|^2 \approx 1.6$ Bohr^2) compared to R_{N-N}=1.5Å ($|\mathbf{d}_{H19}|^2 \approx 0.84$ Bohr^2). At higher orders (H27, H29), the variation of $|\mathbf{d}|^2$ with the bond length does not exceed 15%.

This behavior is consistent with the observed decrease in the modulation of harmonic intensity for higher harmonic orders (Fig. 6.2 (A)). The lower modulation depth observed for perpendicular polarization of the pump and probe pulse is also consistent with the overall 0.37 times$\approx$ decrease of the recombination matrix elements for this geometry. For both geometries, the modulation remains in phase for all harmonics, indicating that the observed dependences cannot be explained by the structural dependence of the recombination matrix elements.

Even though the cation excited state (here B_{2g}) does not contribute significantly to HHG emission in $N_2O_4^+$, in other molecules emission from different ionization continua will add coherently; thus observables such as the ellipticity and phase shift of the HHG emission emerge as a sensitive diagnostic of dynamics in polyatomic molecules.

6.8 Outlook

This discovery brings both challenges and opportunities to the application of strong field ionization and HHG to molecular structure and dynamics studies. Whereas a simple picture involving only a single HOMO orbital may be sufficient for simple diatomic molecules, generalization to larger molecules undergoing large structural changes will require more complicated theoretical treatments. On the other hand, the sensitivity of strong field ionization and HHG to different ionization continua promises that techniques that monitor tunneling ionization, photoelectron distributions and HHG simultaneously can uncover detailed information on electronic and nuclear structure and dynamics in polyatomic molecules.

Chapter 7

Summary and Future directions

7.1 Advantages and disadvantages of HHG spectroscopy

In summary, we have demonstrated that high harmonic generation —a strong field phenomenon initiated by ionization and completed by the electric field driven recollision— can be a very powerful tool for probing molecular structure (Chapters 3, 4, and 5) and monitoring dynamics (Chapter 6). HHG emission from aligned and dynamically excited molecules carries information of molecular structure and dynamics, such as phase and amplitude information on the molecular orbital and adiabatic coupling between electronic and nuclear motion in molecules. As a microscopic collision process, the colliding electron current in HHG is actually quite high as compared to conventional electron colliders [99]. Furthermore, the recollision process in HHG is also a coherent process, which means that it can be considered as an interference between the continuum and bound part of the electron wave function. Forthermore, the state selectivity of tunnel ionization and the time resolution of the HHG spectroscopy technique make it a useful molecular spectroscopy method, that is complementary to weak field methods such as photoelectron spectroscopy.

Notwithstanding these advantanges, HHG spectroscopy also presents important disadvantages as compared to weak field probing methods. The first is the presence of the strong laser electric field during the entire process. The molecular ion with which the electron collides is under distortion by the strong laser field, rather than under a field-free condition. The second disadvantage is the Coulomb laser coupling during the entire process. The recolliding electron wave packet originates from the molecular HOMO and is influenced by the Coulomb potential when it is accelerated in the continuum. This makes it a less that perfectly well-controlled probe.

However, since HHG in molecules offers more information than HHG from atoms, the bright future of the molecular HHG spectroscopy lies in the understanding of the strong field process itself. Our data and work clearly show that the understanding of atoms and molecules in a strong laser field, especially HHG from molecules, is far from complete. Ultimately, a theory which can combine the predictive power of the TDSE with the physical insight of the three-step model is still needed.

7.2 Future directions

The techniques developed in this work can be potentially extended to other questions and systems of strong field physics and chemistry. We list a few examples here.

(1) HHG using driving laser wavelengths longer than 790 nm (in the mid-infrared range) has recently attracted considerable attention. The advantage of using of a long wavelength driver is that it can extend the cutoff of the generated harmonics, because U_p is $\propto \lambda^2$. A long wavelength driver also reduces the level of ionization, which opens the door for HHG experiments on many chemically interesting molecules with a low I_p. For these molecules, only very low-order harmonics can be generated by a 790 nm laser. However, HHG conversion efficiency decreases quickly with the increasing driving laser wave length, because the electron wave packet spreads more when it travels in the continuum, reducing the recollision probability. This decreasing efficiency might reduce the HHG flux to the point where the a sufficient signal-to-noise ratio can not be achieved.

(2) For molecules with a permanent dipole moment, such as N_2O, it is possible

to orient the molecules by either a static electric field or a strong half-cycle pulse at THz frequency. Even-order harmonics can be generated from oriented molecules.

(3) It will be interesting to study more complex molecules such as long carbon chain molecules, which are in liquid form at room temperature. Our current setup is limited to gas phase molecules. In principle, we can inject high-density vapor into the chamber by raising the temperature of the jet.

(4) The recent proposed relationship between the recollision step of HHG and photoionization seems to be a very clear model. Since the HHG yield is related to the differential photoionization cross-section, it would be interesting to investigate the relationship of the HHG polarization state and the photoelectron angular distribution in photoionization.

(5) For the electronically-excited molecular states, a careful measurement of the polarization state of the HHG emitted may reveal interesting physics. From states with different symmetry, it may be possible to generate HHG with perpendicular polarizations.

Bibliography

[1] Wolfgang Demtrder. Laser spectroscopy. Springer, (2003).

[2] Helmut H. Telle, Angel Gonzlez Urea, and Robert John Donovan. Laser chemistry. Wiley, (2007).

[3] E. A. Cornell and C. E. Wieman. Nobel lecture: Bose-einstein condensation in a dilute gas, the first 70 years and some recent experiments. Rev. Mod. Phys., 74(3):875–893, (2002).

[4] S. T. Cundiff and J. Ye. Colloquium: Femtosecond optical frequency combs. Rev. Mod. Phys., 75(1):325–342, (2003).

[5] Rudolph Wolfgang Diels, Jean-Claude. Ultrashort laser pulse phenomena. Academic Press, (2006).

[6] A. H. Zewail. Laser femtochemistry. Science, 242(4886):1645–1653, (1988).

[7] M. J. Rosker, M. Dantus, and A. H. Zewail. Femtosecond clocking of the chemical-bond. Science, 241(4870):1200–1202, (1988).

[8] http://www.andor.com/.

[9] Benjamin Whitaker. Imaging in molecular dynamics. Cambridge University Press, (2003).

[10] R. Dorner, V. Mergel, O. Jagutzki, L. Spielberger, J. Ullrich, R. Moshammer, and H. Schmidt-Bocking. Cold target recoil ion momentum spectroscopy: a 'momentum microscope' to view atomic collision dynamics. Physics Reports-Review Section of Physics Letters, 330(2-3):95–192, (2000).

[11] J. Seres, E. Seres, A. J. Verhoef, G. Tempea, C. Strelill, P. Wobrauschek, V. Yakovlev, A. Scrinzi, C. Spielmann, and F. Krausz. Source of coherent kiloelectronvolt x-rays. Nature, 433(7026):596–596, (2005).

[12] K. C. Kulander, K. J. Schafer, and J. L. Krause. Dynamics of short-pulse excitation, ionization and harmonic conversion. in Super-intense laser-atom physics, (Plenum Press, New York, 1993):95–110, (1993).

[13] P. B. Corkum. Plasma perspective on strong-field multiphoton ionization. Phys. Rev. Lett., 71(13):1994–1997, (1993).

[14] M. Lewenstein, P. Balcou, M. Y. Ivanov, A. Lhuillier, and P. B. Corkum. Theory of high-harmonic generation by low-frequency laser fields. Phys. Rev. A, 49(3):2117–2132, (1994).

[15] K. C. Kulander and B. W. Shore. Calculations of multiple-harmonic conversion of 1064-nm radiation in xe. Phys. Rev. Lett., 62(5):524–526, (1989).

[16] J. L. Krause, K. J. Schafer, and K. C. Kulander. High-order harmonic generation from atoms and ions in the high intenstiy regime. Phys. Rev. Lett., 68:3535, (1992).

[17] L. V. Keldysh. Ionization in field of a strong electromagnetic wave. Soviet Physics JETP, 20(5):1307, (1965).

[18] M. V. Ammosov, N. B. Delone, and V. P. Krainov. Tunnel ionization of complex atoms and atomic ions in a varying electromagnetic-field. Zhurnal Eksperimentalnoi I Teoreticheskoi Fiziki, 91(6):2008–2013, (1986).

[19] Z. H. Chang, A. Rundquist, H. W. Wang, M. M. Murnane, and H. C. Kapteyn. Generation of coherent soft x rays at 2.7 nm using high harmonics. Phys. Rev. Lett., 79(16):2967–2970, (1997).

[20] Ferenc Krausz and Misha Ivanov. Attosecond physics. Rev. Mod. Phys., 81(1):163–72, (2009).

[21] Pascal Salieres, Anne L'Huillier, and Maciej Lewenstein. Coherence control of high-order harmonics. Phys. Rev. Lett., 74(19):3776, (1995).

[22] A. Rundquist, C. G. Durfee, Z. H. Chang, C. Herne, S. Backus, M. M. Murnane, and H. C. Kapteyn. Phase-matched generation of coherent soft x-rays. Science, 280(5368):1412–1415, (1998).

[23] R. A. Bartels, A. Paul, H. Green, H. C. Kapteyn, M. M. Murnane, S. Backus, I. P. Christov, Y. W. Liu, D. Attwood, and C. Jacobsen. Generation of spatially coherent light at extreme ultraviolet wavelengths. Science, 297(5580):376–378, (2002).

[24] B.D. Cullity. Elements of x-ray diffraction. Addison-Wesley, (1978).

[25] J. Muth-Bohm, A. Becker, and F. H. M. Faisal. Suppressed molecular ionization for a class of diatomics in intense femtosecond laser fields. Phys. Rev. Lett., 85(11):2280, (2000).

[26] X. M. Tong, Z. X. Zhao, and C. D. Lin. Theory of molecular tunneling ionization. Phys. Rev. A, 66(3):11, (2002).

[27] J. G. Underwood A. Stolow. Advances in chemical physics. 139:497, (2008).

[28] A. H. Zewail. 4d ultrafast electron diffraction, crystallography, and microscopy. Annual Review of Physical Chemistry, 57:65–103, (2006).

[29] D. Strickland and G. Mourou. Compression of amplified chirped optical pulses. Optics Comm., 56(3):219–221, (1985).

[30] S. Backus, C. G. Durfee, M. M. Murnane, and H. C. Kapteyn. High power ultrafast lasers. Rev. Sci. Instru., 69(3):1207–1223, (1998).

[31] Nist standard reference database. 69.

[32] A. Wuest and R. Lock. unpublished.

[33] X. X. Zhou, X. M. Tong, Z. X. Zhao, and C. D. Lin. Role of molecular orbital symmetry on the alignment dependence of high-order harmonic generation with molecules. Phys. Rev. A, 71(6), (2005).

[34] X. X. Zhou, X. M. Tong, Z. X. Zhao, and C. D. Lin. Alignment dependence of high-order harmonic generation from n-2 and o-2 molecules in intense laser fields. Phys. Rev. A, 72(3):033412, (2005).

[35] R. Torres, N. Kajumba, J. G. Underwood, J. S. Robinson, S. Baker, J. W. G. Tisch, R. de Nalda, W. A. Bryan, R. Velotta, C. Altucci, I. C. E. Turcu, and J. P. Marangos. Probing orbital structure of polyatomic molecules by high-order harmonic generation. Phys. Rev. Lett., 98(20):203007, (2007).

[36] S. Ramakrishna and T. Seideman. Information content of high harmonics generated from aligned molecules. Phys. Rev. Lett., 99(11):113901, (2007).

[37] J. Itatani, J. Levesque, D. Zeidler, H. Niikura, H. Pepin, J. C. Kieffer, P. B. Corkum, and D. M. Villeneuve. Tomographic imaging of molecular orbitals. Nature (London), 432(7019):867–871, (2004).

[38] S. Patchkovskii, Z. X. Zhao, T. Brabec, and D. M. Villeneuve. High harmonic generation and molecular orbital tomography in multielectron systems: Beyond the single active electron approximation. Phys. Rev. Lett., 97(12):123003, (2006).

[39] S. Patchkovskii, Z. X. Zhao, T. Brabec, and D. M. Villeneuve. High harmonic generation and molecular orbital tomography in multielectron systems. J. Chem. Phys., 126(11):114306, (2007).

[40] O. Smirnova, M. Spanner, and M. Ivanov. Analytical solutions for strong field-driven atomic and molecular one- and two-electron continua and applications to strong-field problems. Phys. Rev. A, 77(3):033407, (2008).

[41] Anh-Thu Le, Toru Morishita, and C. D. Lin. Extraction of the species-dependent dipole amplitude and phase from high-order harmonic spectra in rare-gas atoms. Phys. Rev. A, 78(2):023814–6, (2008).

[42] Toru Morishita, Anh-Thu Le, Zhangjin Chen, and C. D. Lin. Accurate retrieval of structural information from laser-induced photoelectron and high-order harmonic spectra by few-cycle laser pulses. Phys. Rev. Lett., 100(1):013903–4, (2008).

[43] Fainstein P. D. Martiarena M. L. Picca, R Della and A. Dubois. Angular distributions of photoelectrons emitted from fixed in-space hydrogen molecular ions. J. Phys. B, 39(3):473, (2006).

[44] H. D. Cohen and U. Fano. Interference in photo-ionization of molecules. Phys. Rev., 150(1):30, (1966).

[45] M. Lein, N. Hay, R. Velotta, J. P. Marangos, and P. L. Knight. Role of the intramolecular phase in high-harmonic generation. Phys. Rev. Lett., 88(18):183903, (2002).

[46] M. Lein, N. Hay, R. Velotta, J. P. Marangos, and P. L. Knight. Interference effects in high-order harmonic generation with molecules. Phys. Rev. A, 66(2):023805, (2002).

[47] T. Kanai, S. Minemoto, and H. Sakai. Quantum interference during high-order harmonic generation from aligned molecules. Nature (London), 435(7041):470–474, (2005).

[48] C. Vozzi, F. Calegari, E. Benedetti, J. P. Caumes, G. Sansone, S. Stagira, M. Nisoli, R. Torres, E. Heesel, N. Kajumba, J. P. Marangos, C. Altucci, and R. Velotta. Controlling two-center interference in molecular high harmonic generation. Phys. Rev. Lett., 95(15):153902, (2005).

[49] A. T. Le, X. M. Tong, and C. D. Lin. Evidence of two-center interference in high-order harmonic generation from co2. Phys. Rev. A, 73(4):041402(R), (2006).

[50] H. Wabnitz, Y. Mairesse, L. J. Frasinski, M. Stankiewicz, W. Boutu, P. Breger, P. Johnsson, H. Merdji, P. Monchicourt, P. Salieres, K. Varju, M. Vitteau, and B. Carre. Generation of attosecond pulses in molecular nitrogen. Eur. Phys. J. D, 40(2):305–311, (2006).

[51] N. Wagner, X. B. Zhou, R. Lock, W. Li, A. Wuest, M. Murnane, and H. Kapteyn. Extracting the phase of high-order harmonic emission from a molecule using transient alignment in mixed samples. Phys. Rev. A, 76(6):–, (2007).

[52] Chirila C. Lein M. Signatures of molecular structure and dynamics in high-order harmonic generation. World Scientific, (2007).

[53] N. Hay, M. Lein, R. Velotta, R. De Nalda, E. Heesel, M. Castillejo, P. L. Knight, and J. P. Marangos. Investigations of electron wave-packet dynamics and high-order harmonic generation in laser-aligned molecules. J. Mod. Opt., 50(3-4):561–577, (2003).

[54] C. C. Chirila and M. Lein. Assessing different forms of the strong-field approximation for harmonic generation in molecules. J. Mod. Opt., 54(7):1039–1045, (2007).

[55] X. B. Zhou, R. Lock, W. Li, N. Wagner, M. M. Murnane, and H. C. Kapteyn. Molecular recollision interferometry in high harmonic generation. Phys. Rev. Lett., 100(7):073902, (2008).

[56] T. Kanai, E. J. Takahashi, Y. Nabekawa, and K. Midorikawa. Observing molecular structures by using high-order harmonic generation in mixed gases. Phys. Rev. A, 77(4):–, (2008).

[57] J. Ortigoso, M. Rodriguez, M. Gupta, and B. Friedrich. Time evolution of pendular states created by the interaction of molecular polarizability with a pulsed nonresonant laser field. J. Chem. Phys., 110(8):3870–3875, (1999).

[58] Hans Jakob Worner, Hiromichi Niikura, Julien B. Bertrand, P. B. Corkum, and D. M. Villeneuve. Observation of electronic structure minima in high-harmonic generation. Phys. Rev. Lett., 102(10):103901–4, (2009).

[59] M. Bellini, C. Lynga, A. Tozzi, M. B. Gaarde, T. W. Hansch, A. L'Huillier, and C. G. Wahlstrom. Temporal coherence of ultrashort high-order harmonic pulses. Phys. Rev. Lett., 81(2):297–300, (1998).

[60] C. Corsi, A. Pirri, E. Sali, A. Tortora, and M. Bellini. Direct interferometric measurement of the atomic dipole phase in high-order harmonic generation. Phys. Rev. Lett., 97(2):023901, (2006).

[61] C. Vozzi, F. Calegari, E. Benedetti, R. Berlasso, G. Sansone, S. Stagira, M. Nisoli, C. Altucci, R. Velotta, R. Torres, E. Heesel, N. Kajumba, and J. P. Marangos. Probing two-centre interference in molecular high harmonic generation. J. Phys. B, 39(13):S457–S466, (2006).

[62] O. Smirnova, A. S. Mouritzen, S. Patchkovskii, and M. Y. Ivanov. Coulomb-laser coupling in laser-assisted photoionization and molecular tomography. J. Phys. B, 40(13):F197–F206, (2007).

[63] Olga Smirnova, Serguei Patchkovskii, Yann Mairesse, Nirit Dudovich, David Villeneuve, Paul Corkum, and Misha Yu Ivanov. Attosecond circular dichroism spectroscopy of polyatomic molecules. Phys. Rev. Lett., 102(6):063601–4, (2009).

[64] R. Torres and J. P. Marangos. Mapping of orbital structure from high harmonic generation through the molecular dipole moment. J. Mod. Opt., 54(13-15):1883–1899, (2007).

[65] Y. Mairesse, J. Levesque, N. Dudovich, P. B. Corkum, and D. M. Villeneuve. High harmonic generation from aligned molecules - amplitude and polarization. J. Mod. Opt., 55(16):2591–2602, (2008).

[66] W. Boutu, S. Haessler, H. Merdji, and P. Breger. Coherent control of attosecond emission from aligned molecules. Nature Physics, 4:545, (2008).

[67] Y. Mairesse, A. de Bohan, L. J. Frasinski, H. Merdji, L. C. Dinu, P. Monchicourt, P. Breger, M. Kovacev, R. Taieb, B. Carre, H. G. Muller, P. Agostini, and P. Salieres. Attosecond synchronization of high-harmonic soft x-rays. Science, 302(5650):1540–1543, (2003).

[68] J. Levesque, D. Zeidler, J. P. Marangos, P. B. Corkum, and D. M. Villeneuve. High harmonic generation and the role of atomic orbital wave functions. Phys. Rev. Lett., 98(18):183903, (2007).

[69] X. B. Zhou, R. Lock, N. Wagner, W. Li, H. C. Kapteyn, and M. M. Murnane. Elliptically polarized high-order harmonic emission from molecules in linearly polarized laser fields. Phys. Rev. Lett., 102(7):–, (2009).

[70] V. H. Le, A. T. Le, R. H. Xie, and C. D. Lin. Theoretical analysis of dynamic chemical imaging with lasers using high-order harmonic generation. Phys. Rev. A, 76(1):013414, (2007).

[71] P. Antoine, B. Carre, A. Lhuillier, and M. Lewenstein. Polarization of high-order harmonics. Phys. Rev. A, 55(2):1314–1324, (1997).

[72] B. L. Henke, E. M. Gullikson, and J. C. Davis. Atomic Data and Nuclear Data Tables, 54:181, (1993).

[73] M. Born and E. Wolf. Principle of optics. (1999).

[74] X. H. Xie, A. Scrinzi, M. Wickenhauser, A. Baltuska, I. Barth, and M. Kitzler. Internal momentum state mapping using high harmonic radiation. Phys. Rev. Lett., 101(3):033901, (2008).

[75] P. Dietrich, N. H. Burnett, M. Ivanov, and P. B. Corkum. High-harmonic generation and correlated 2-electron multiphoton ionization with elliptically polarized-light. Phys. Rev. A, 50(5):R3585–R3588, (1994).

[76] N. H. Burnett, C. Kan, and P. B. Corkum. Ellipticity and polarization effects in harmonic-generation in ionizing neon. Phys. Rev. A, 51(5):R3418–R3421, (1995).

[77] K. Miyazaki and H. Takada. High-order harmonic-generation in the tunneling regime. Phys. Rev. A, 52(4):3007–3021, (1995).

[78] M. Kakehata, H. Takada, H. Yumoto, and K. Miyazaki. Anomalous ellipticity dependence of high-order harmonic generation. Phys. Rev. A, 55(2):R861–R864, (1997).

[79] M. Y. Ivanov, T. Brabec, and N. Burnett. Coulomb corrections and polarization effects in high-intensity high-harmonic emission. Phys. Rev. A, 54(1):742–745, (1996).

[80] F. A. Weihe and P. H. Bucksbaum. Measurement of the polarization state of high harmonics generated in gases. J. Opt. Soc. Am. B, 13(1):157–161, (1996).

[81] F. A. Weihe, S. K. Dutta, G. Korn, D. Du, P. H. Bucksbaum, and P. L. Shkolnikov. Polarization of high-intensity high-harmonic generation. Phys. Rev. A, 51(5):R3433–R3436, (1995).

[82] G. Sansone, E. Benedetti, F. Calegari, C. Vozzi, L. Avaldi, R. Flammini, L. Poletto, P. Villoresi, C. Altucci, R. Velotta, S. Stagira, S. De Silvestri, and M. Nisoli. Isolated single-cycle attosecond pulses. Science, 314(5798):443–446, (2006).

[83] I. J. Sola, E. Mevel, L. Elouga, E. Constant, V. Strelkov, L. Poletto, P. Villoresi, E. Benedetti, J. P. Caumes, S. Stagira, C. Vozzi, G. Sansone, and M. Nisoli. Controlling attosecond electron dynamics by phase-stabilized polarization gating. Nat Phys, 2(5):319–322, (2006).

[84] T. Kanai, S. Minemoto, and H. Sakai. Ellipticity dependence of high-order harmonic generation from aligned molecules. Phys. Rev. Lett., 98(5), (2007).

[85] Y. Mairesse, N. Dudovich, J. Levesque, M. Y. Ivanov, P. B. Corkum, and D. M. Villeneuve. Electron wavepacket control with elliptically polarized laser light in high harmonic generation from aligned molecules. New J. Phys., 10:13, (2008).

[86] N. Dudovich, J. Levesque, O. Smirnova, D. Zeidler, D. Comtois, M. Y. Ivanov, D. M. Villeneuve, and P. B. Corkum. Attosecond temporal gating with elliptically polarized light. Phys. Rev. Lett., 97(25):–, (2006).

[87] S. Baker, J. S. Robinson, C. A. Haworth, H. Teng, R. A. Smith, C. C. Chirila, M. Lein, J. W. G. Tisch, and J. P. Marangos. Probing proton dynamics in molecules on an attosecond time scale. Science, 312(5772):424–427, (2006).

[88] N. L. Wagner, A. Wuest, I. P. Christov, T. Popmintchev, X. B. Zhou, M. M. Murnane, and H. C. Kapteyn. Monitoring molecular dynamics using coherent electrons from high harmonic generation. Proc. Natl. Acad. Sci. USA, 103(36):13279–13285, (2006).

[89] Z. B. Walters, S. Tonzani, and C. H. Greene. High harmonic generation in sf6: Raman-excited vibrational quantum beats. J. Phys. B, 40(18):F277–F283, (2007).

[90] W. Li, X. B. Zhou, R. Lock, S. Patchkovskii, A. Stolow, H. C. Kapteyn, and M. M. Murnane. Time-resolved dynamics in n2o4 probed using high harmonic generation. Science, 322(5905):1207–1211, (2008).

[91] A. Stolow, A. E. Bragg, and D. M. Neumark. Femtosecond time-resolved photoelectron spectroscopy. Chemical Reviews, 104(4):1719–1757, (2004).

[92] O. Gessner, A. M. D. Lee, J. P. Shaffer, H. Reisler, S. V. Levchenko, A. I. Krylov, J. G. Underwood, H. Shi, A. L. L. East, D. M. Wardlaw, E. T. Chrysostom, C. C. Hayden, and A. Stolow. Femtosecond multidimensional imaging of a molecular dissociation. Science, 311(5758):219–222, (2006).

[93] V. Blanchet, M. Z. Zgierski, T. Seideman, and A. Stolow. Discerning vibronic molecular dynamics using time-resolved photoelectron spectroscopy. Nature, 401(6748):52–54, (1999).

[94] M. Ferray, A. Lhuillier, X. F. Li, L. A. Lompre, G. Mainfray, and C. Manus. Multiple-harmonic conversion of 1064 nm radiation in rare-gases. J. Phys. B, 21(3):L31–L35, (1988).

[95] A. McPherson, G. Gibson, H. Jara, U. Johann, T. S. Luk, I. A. McIntyre, K. Boyer, and C. K. Rhodes. Studies of multiphoton production of vacuum-ultraviolet radiation in the rare gases. J. Opt. Soc. Am. B, 4(4):595–601, (1987).

[96] M. Lezius, V. Blanchet, Misha Yu Ivanov, and Albert Stolow. Polyatomic molecules in strong laser fields: Nonadiabatic multielectron dynamics. J. Chem. Phys., 117(4):1575–1588, (2002).

[97] Marc Smits, C. A. de Lange, Albert Stolow, and D. M. Rayner. Dynamic polarization in the strong-field ionization of small metal clusters. Phys. Rev. Lett., 93(20):203402, (2004).

[98] R. Santra and A. Gordon. Three-step model for high-harmonic generation in many-electron systems. Phys. Rev. Lett., 96(7):4, (2006).

[99] M. Meckel, D. Comtois, D. Zeidler, A. Staudte, D. Pavicic, H. C. Bandulet, H. Pepin, J. C. Kieffer, R. Dorner, D. M. Villeneuve, and P. B. Corkum. Laser-induced electron tunneling and diffraction. Science, 320(5882):1478–1482, (2008).

[100] T. H. Gan, J. B. Peel, and G. D. Willett. Reinterpretation of photoelectron-spectrum of dinitrogen tetroxide. Journal of the Chemical Society-Faraday Transactions Ii, 73:1459–1463, (1977).

[101] X. B. Zhou, H. Kapteyn, and M. Murnane. Positive-dispersion cavity-dumped ti: sapphire laser oscillator and its application to white light generation. Optics Express, 14(21):9750–9757, (2006).

[102] M. Ramaswamy, M. Ulman, J. Paye, and J. G. Fujimoto. Cavity-dumped femtosecond kerr-lens mode-locked ti-al2o3 laser. Opt. Lett., 18(21):1822–1824, (1993).

[103] M. S. Pshenichnikov, W. P. Deboeij, and D. A. Wiersma. Generation of 13-fs, 5-mw pulses from a cavity-dumped ti-sapphire laser. Opt. Lett., 19(8):572–574, (1994).

[104] G. N. Gibson, R. Klank, F. Gibson, and B. E. Bouma. Electro-optically cavity-dumped ultrashort-pulse ti:sapphire oscillator. Opt. Lett., 21(14):1055–1057, (1996).

[105] A. Baltuska, Z. Wei, M. S. Pshenichnikov, D. A. Wiersma, and R. Szipocs. All-solid-state cavity-dumped sub-5-fs laser. Appl. Phys. B, 65(2):175–188, (1997).

[106] A. Killi, U. Morgner, M. J. Lederer, and D. Kopf. Diode-pumped femtosecond laser oscillator with cavity dumping. Opt. Lett., 29(11):1288–1290, (2004).

[107] A. Killi, A. Steinmann, J. Dorring, U. Morgner, M. J. Lederer, D. Kopf, and C. Fallnich. High-peak-power pulses from a cavity-dumped yb : Ky(wo4)2 oscillator. Opt. Lett., 30(14):1891–1893, (2005).

[108] A. M. Kowalevicz, A. T. Zare, F. X. Kartner, J. G. Fujimoto, S. Dewald, U. Morgner, V. Scheuer, and G. Angelow. Generation of 150-nj pulses from a multiple-pass cavity kerr-lens mode-locked ti : Al2o3 oscillator. Opt. Lett., 28(17):1597–1599, (2003).

[109] A. Killi, A. Steinmann, G. Palmer, U. Morgner, H. Bartelt, and J. Kobelke. Megahertz optical parametric amplifier pumped by a femtosecond oscillator. Opt. Lett., 31(1):125–127, (2006).

[110] A. Brodeur and S. L. Chin. Ultrafast white-light continuum generation and self-focusing in transparent condensed media. J. Opt. Soc. Am. B, 16(4):637–650, (1999).

[111] S. H. Cho, B. E. Bouma, E. P. Ippen, and J. G. Fujimoto. Low-repetition-rate high-peak-power kerr-lens mode-locked ti : Al2o3 laser with a multiple-pass cavity. Opt. Lett., 24(6):417–419, (1999).

[112] S. H. Cho, F. X. Kartner, U. Morgner, E. P. Ippen, J. G. Fujimoto, J. E. Cunningham, and W. H. Knox. Generation of 90-nj pulses with a 4-mhz repetition-rate kerr-lens mode-locked ti : Al2o3 laser operating with net positive and negative intracavity dispersion. Opt. Lett., 26(8):560–562, (2001).

[113] A. Fernandez, T. Fuji, A. Poppe, A. Furbach, F. Krausz, and A. Apolonski. Chirped-pulse oscillators: a route to high-power femtosecond pulses without external amplification. Opt. Lett., 29(12):1366–1368, (2004).

[114] S Naumov, A Fernandez, R Graf, P Dombi, F Krausz, and A Apolonski. Approaching the microjoule frontier with femtosecond laser oscillators. New J. Phys., 7:216, (2005).

[115] V. L. Kalashnikov, E. Podivilov, A. Chernykh, S. Naumov, A. Fernandez, R. Graf, and A. Apolonski. Approaching the microjoule frontier with femtosecond laser oscillators: theory and comparison with experiment. New J. Phys., 7:217, (2005).

[116] B. Proctor, E. Westwig, and F. Wise. Characterization of a kerr-lens mode-locked ti-sapphire laser with positive group-velocity dispersion. Opt. Lett., 18(19):1654–1656, (1993).

[117] S. Dewald, T. Lang, C. D. Schroeter, R. Moshammer, J. Ullrich, M. Siegel, and U. Morgner. Ionization of noble gases with pulses directly from a laser oscillator. Opt. Lett., 31:In press, (2006).

[118] S. Backus, R. Bartels, S. Thompson, R. Dollinger, H. C. Kapteyn, and M. M. Murnane. Sigh-efficiency, single-stage 7-khz high-average-power ultrafast laser system. Opt. Lett., 26(7):465–467, (2001).

[119] R. Huber, F. Adler, A. Leitenstorfer, M. Beutter, P. Baum, and E. Riedle. 12-fs pulses from a continuous-wave-pumped 200-nj ti : sapphire amplifier at a variable repetition rate as high as 4 mhz. Opt. Lett., 28(21):2118–2120, (2003).

Appendix A

Positive Dispersion Cavity Dump Ti: Sapphire Oscillator

In this appendix, we present the first demonstration that up to 0.45 μJ pulses can be obtained from a cavity-dumped Ti: sapphire oscillator stably operating in the positive dispersion regime [101]. The output pulse can be compressed to 60 fs and used to generate a white light continuum through self-filamentation in a thin sapphire plate.

A.1 Introduction

Cavity dumping is a standard technique for generating moderate-energy pulses from femtosecond Ti: sapphire laser oscillators [102, 103, 104, 105]. A cavity dumper can increase the effective output coupling from a Ti: sapphire oscillator from 5-10% up to ~80%, giving an order of magnitude increase in pulse energy from the laser, at the expense of reduced repetition-rate. Pulse energies of >200 nJ have been reported from electro-optically cavity dumped Ti:sapphire oscillators [104], but at very low repetitions rates (kHz) and with limited repeatability. More generally, multi-pulse and continuous wave (CW) breakthrough instabilities from excessive Kerr nonlinearity have limited the obtainable stable-and-repeatable energy to tens of nJ energy and ~ 100mW average power. Other materials such as Yb:glass [106] and Yb:KYW [107], have operated mode locked and cavity dumped by employing semiconductor saturable-absorber mirrors (SESAMs). Although μJ pulse energies can be generated by these lasers, the peak power is only a few MW since the pulse duration is limited to a few hundred fs. For applications in materials micromachining [108], nonlinear frequency conversion [109], and femtosecond white-light continuum generation [110], a MHz repetition-rate source with ∼μJ pulse energy and sub-100 fs pulse duration would be desirable.

An alternative to cavity dumping is to extend the length of the laser cavity to reduce the repetition rate and increase the per-pulse energy [111, 112, 108, 113]. The extreme example of this is to include a Herriott-type multi-pass telescope in the standard oscillator cavity to obtain repetition rates as low as 2 MHz [114], corresponding to a 150m cavity length. To avoid excessive Kerr nonlinearity due to the high intracavity peak power, these oscillators are operated either with large negative or small positive intracavity dispersion, and in some cases with SESAMs to support stable mode locking [112, 114, 115]. 43 fs, 150nJ pulses have been generated by working in the large negative dispersion regime (NDR) [112] . In the positive dispersion regime (PDR) [116] , the pulse in the cavity is broadened by the combined action of positive group velocity dispersion (GVD) and self phase modulation (SPM), and the laser is mode locked by the dynamic gain saturation, spectral filtering , and self amplitude modulation (SAM) or Kerr-lens mode-locking (KLM) [115]. In PDR, a heavily chirped ps pulse is generated that can be externally compressed to <100 fs [113, 114]. The long pulse duration inside the laser in the PDR offers much better energy scalability, with acceptable pulse quality. Recently 130nJ pulse at 11MHZ and 505nJ pulse at 2MHz has been obtained from these chirped-pulse multi-pass cavity (CPMC) oscillators, with peak power as high as 10MW and 1∼2W average power using a 10W pump laser [114].

Here, we show for the first time that it is possible to combine cavity dumping with the positive dispersion regime of operation. Using a configuration similar to the standard (prism dispersion controlled) cavity-dumped geometry [105], sub-100fs pulses with peak power as high as 7.5MW at a variable repetition rate as high as 2 MHz can be generated stably and reliably. Compared with the CPMC oscillator, this positive dispersion cavity dumped (PDCD) oscillator is substantially more energy-efficient, producing up to 450nJ pulse using as low as 6.5 W pump power. Furthermore, it has an easily variable repetition-rate and occupies a footprint of only 0.3m^2—no larger than a standard Ti: sapphire oscillator. This oscillator fills a gap between standard Ti:sapphire oscillators and more-complex oscillator-amplifier systems [30]. Finally, we demonstrate stable filament-induced white light generation from 400nm to 1μm using this laser.

A.2 Laser setup and performance

The laser system setup and external double-pass prism pair compressor is shown in Fig. A.1. A Bragg cell driver and 18W amplifier (CAMAC) drive a fused silica cavity dumper (Harris). The laser repetition-rate is detected by a photodiode, conditioned using a constant fraction discriminator (CFD, Phillips Scientific) and slightly amplified by a pulse generator (Hewlett-Packard 8082A), before going into the Bragg cell driver. All the mirrors are standard dielectric mirrors with low dispersion. The path length in the Ti: sapphire crystal is ∼5 mm.

With a 5.3% output coupler, the laser can be mode locked stably in both the NDR and PDR. In the NDR, the pump power is limited to below 5W to avoid instabilities. For the transition from negative to positive dispersion, we simply add material dispersion by translating the first intracavity prism. Near the zero dispersion point, the laser shows self Q-switched mode-locking behavior, but with more positive dispersion it settles into a stable, hard-edge, spectrum characteristic of a standard Ti:sapphire oscillator operating in the PDR [116] . Increasing the pump power to the full 10.4W once in the PDR, we then optimize the intracavity dispersion and the KLM parameters, i.e. the relative position of the Ti: sapphire crystal and the focusing mirrors. In translating the prism from the negative dispersion point, we estimate that stable operation with ∼40 nm bandwidth is obtained with a net intracavity dispersion of less than 40fs^2. This value is significantly smaller than previous reported using SF10 prisms for dispersion

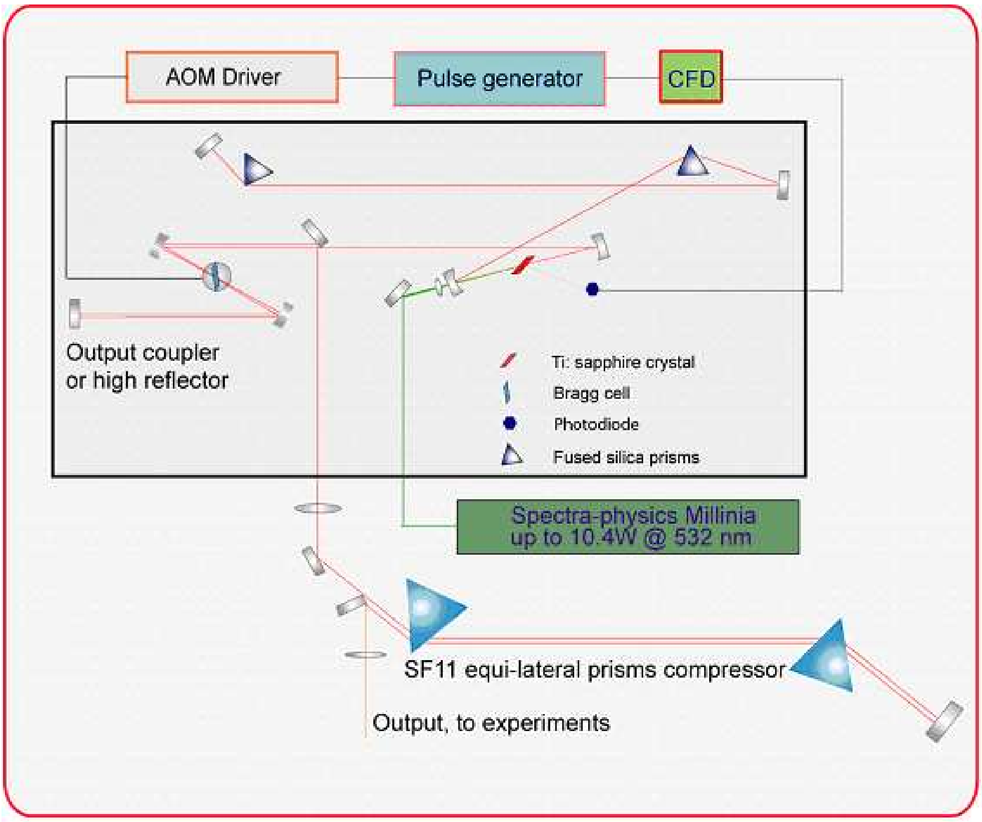

Figure A.1: The setup of the positive dispersion cavity dump oscillator.

compensation in a regular oscillator [116], or using fused silica prisms in multi-pass cavity [114]. The CW output from the output coupler is 2W when pumped by 10.4 W in the PDR, indicating an intracavity pulse energy of 500nJ. The crystal was cooled to -3 °C using antifreeze coolant, and we saw no evidence of thermal lens induced degradation of slope efficiency even at full pump power. Given the very high intracavity pulse energy, non-resonant re-absorption of the 780 nm circulating light might be an issue; however, this absorption appears to be minimal.

A further increase in the intracavity power can be obtained by replacing the output coupler with a standard broadband high reflector (Newport UF20). Stable mode locking operation is sensitive to the relationship between cavity adjustment and dispersion. By comparing the integration of the detected intracavity spectrum with the output coupler used, we estimate that up to 60W intra-cavity power and 750nJ per pulse energy can be obtained at pump power as low as 6.5 W. Stable mode locking, however, is not obtained for higher pulse energies. We believe the limitation is set by saturation of the Kerr lens induced differential gain in the Ti: sapphire crystal, which can occur when the spot size of the red light becomes smaller than the pump light spot size. Robust operation at near-optimum power can be obtained with a high-reflector and 6.5 W pump power. We have used both a Spectra-Physics Millennia X and Coherent Verdi 6 pump laser with comparable results.

When the intracavity peak-power is increased by substituting the output coupler with a high reflector, the spectrum is further broadened, as shown in Fig. A.2 (blue). In this regime, we could obtain up to 60% dumping efficiency without encountering instabilities such as period-doubling or self Q-switching. In the NDR, cavity-dumping only slightly shifts the laser spectrum. However, in the PDR, the spectrum width and shape can be modified dramatically at MHz dumping frequencies, as shown in Fig. A.2 (red). This results from the fact that when the output coupler is replaced with a high reflector, the overall cavity loss (and therefore the intracavity pulse energy) is dominated

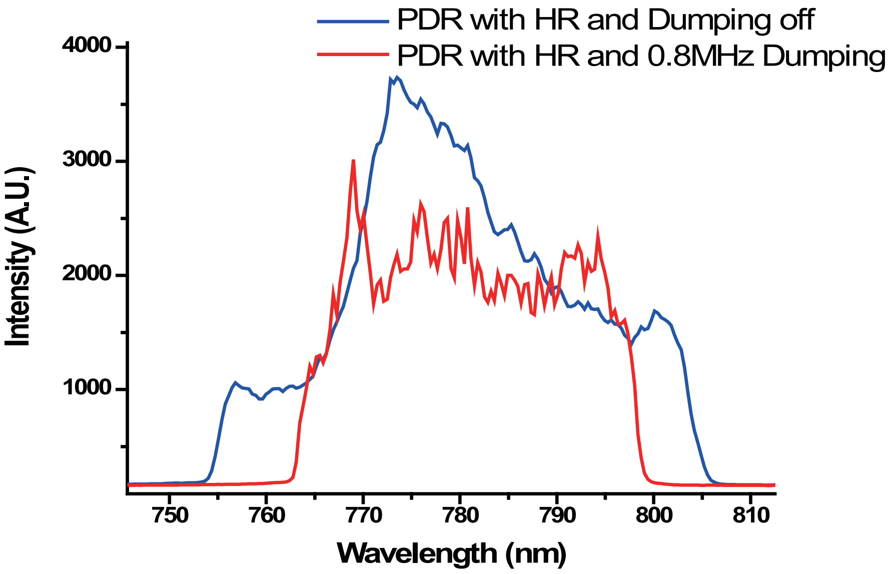

Figure A.2: Spectrum from the cavity-dumped laser in the positive dispersion regime with 6.5 W pump, with the dumper on and off.

by the cavity dumping. Furthermore, in the PDR, the Kerr lens is expected to play a more important role in determining the spectrum inside the cavity than it would for the standard NDR solitary mode of operation.

To obtain the highest pulse energy in a stable mode of operation, we used an RF spectrum analyzer (Agilent E4410B) to monitor the pulse train, and limited the Bragg driver power to below where additional amplitude noise is induced by cavity dumping. A typical microwave spectrum of the intracavity modulated pulse train is shown in Fig. A.3.

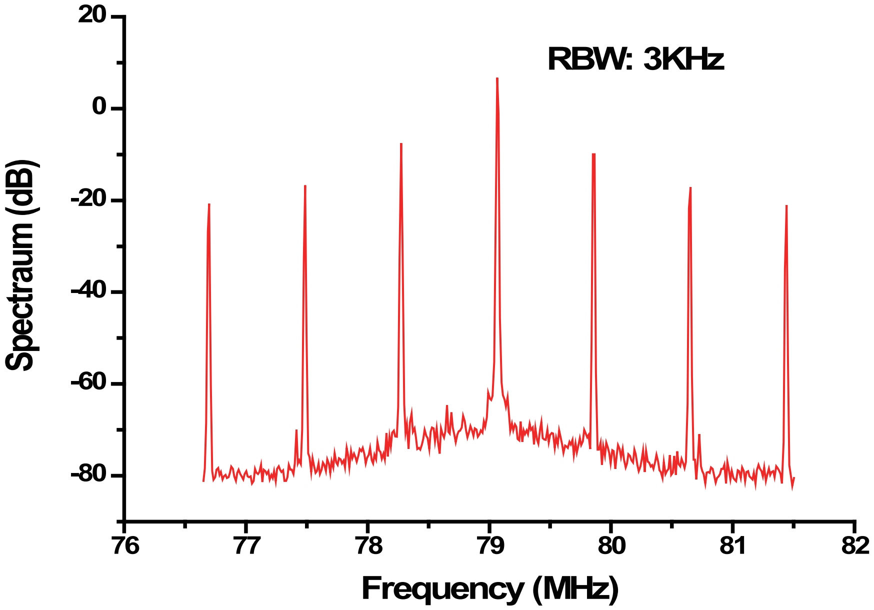

Figure A.3: Typical microwave spectrum of the intra-cavity modulated pulse train.

The dependence of the cavity dumped pulse energy on dumping frequency is shown in Fig. A.4. The peak pulse energy is obtained at 0.8MHz; lower dumping rates give slightly lower energy than at 0.8 MHz, while higher dumping rates give proportionately lower pulse energy. The peak at 0.8 MHz results from relaxation oscillations that give an energy overshoot at about 1.25 μs after dumping of the previous pulse.

Using a fast photodiode (100 ps resolution), combined with a long scan-range (>100 ps) autocorrelator, and a high resolution spectrometer, we confirmed that no secondary pulses are generated even at the highest intracavity peak power. We also measured the intensity contrast ratio between the dumped output pulse and the neighboring pulse. The delay of the Bragg cell driver can be adjusted to give a <1:100 ratio for both the pre- and the post-pulse.

The uncompressed pulse emitted from the laser has duration of about 1.2ps. Using a simple compressor consisting of two equilateral SF11 prisms with 90cm separation, we recompressed the pulse with high (>90%) throughput. Double-passing the compressor gives approximately –10000 fs^2 GVD and -50000fs^3 third-order dispersion. A frequency-resolved optical gating (FROG) measurement of the recompressed pulse is shown in Fig. A.5. The FWHM pulse duration is 60fs, is $\sim$1.3x transform limited, with a peak power of $\sim$7.5MW. The satellite ripples are generated by the sharp edge of the spectrum and the residual third-order dispersion of the prism compressor. The PDCD oscillator and CPMC oscillator have similar sharp edge spectra and satellite pulses in their temporal profiles [113, 114]. We observe slightly longer pulse duration (60fs) than in the case of the CPMC oscillator (45fs at 2MHz repetition rate), because our compressor can not compress the pulse to the transform limit of the spectrum ($\sim$46 fs). Careful engineering of the intracavity dispersion can further broaden the spectrum. The use of a high-throughput pulse shaper or specially-designed TOD compensating chirp mirrors should result in nearly transform-limited pulse duration. As is generally found in lasers operating in the PDR [114, 116], the spectral width and chirp of the output pulse strongly depends on the intracavity dispersion, pulse energy and cavity alignment. Thus the extra cavity dispersion must be re-optimized when the operating parameters of the laser change.

To demonstrate the unique utility of this laser, we generated a white light continuum by focusing the compressed 0.8MHz repetition-rate pulse into thin sapphire and

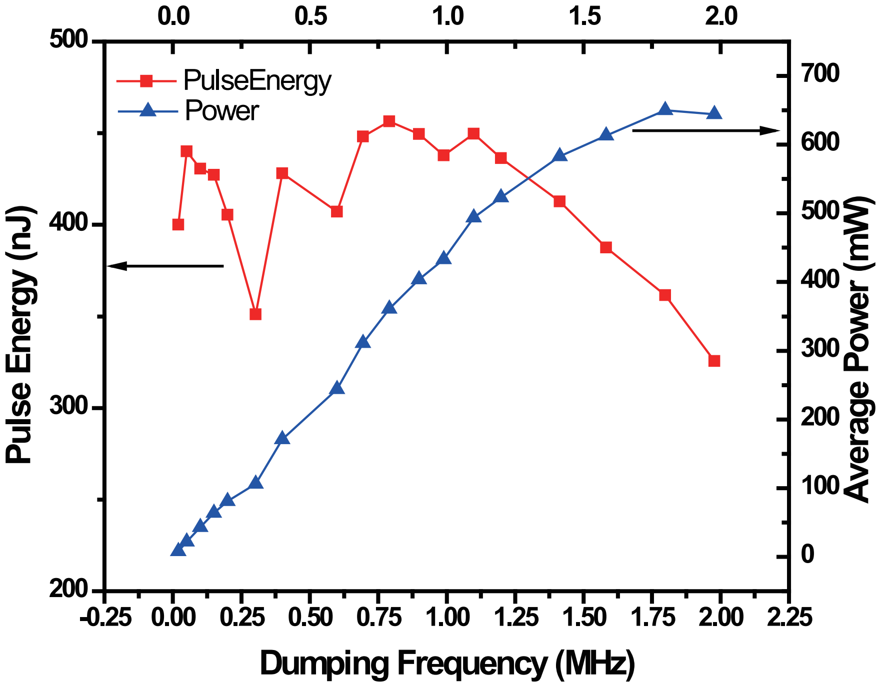

Figure A.4: Pulse energy, and average power as a function of dumping rate in the PDR, with 6.5 W pump power.

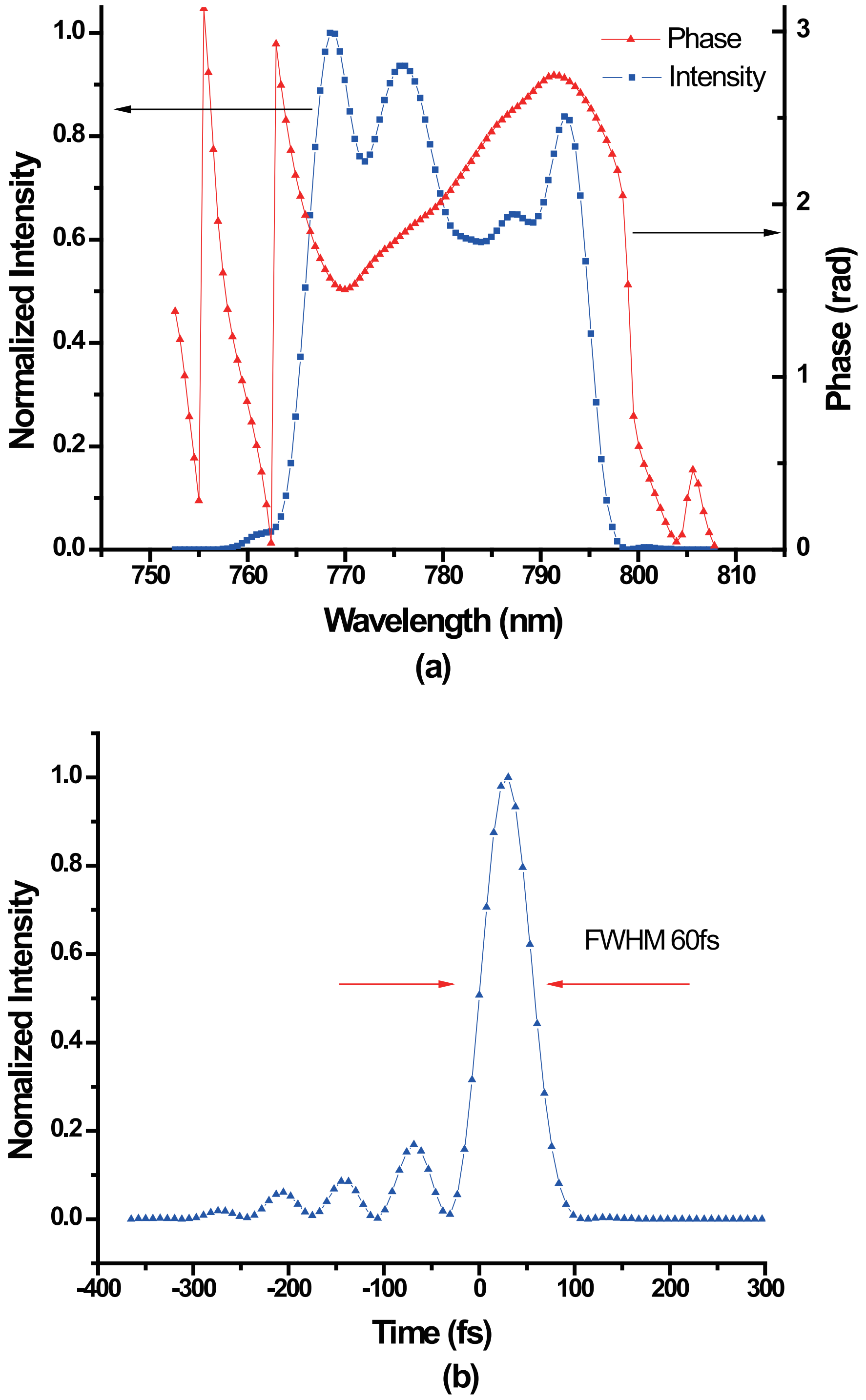

Figure A.5: Spectral (a) and time domain (b) profile of prism-recompressed pulse, reconstructed from FROG measurement.

fused silica plates using a 6 cm FL aspheric lens. Filament-induced white light generation could be observed without the need for careful optimization. The use of sapphire avoids rapid damage and allows extended operation of the white light source. The white light spectrum measured using an optical spectrum analyzer (Ando AQ-6315E) is shown in Fig. A.6. The inset of Fig. A.6 is a digital camera image of the continuum. Although the center of the white light profile is stable, we observe a long time-scale, periodic (∼10 seconds) instability in the red ring. We speculate that this results from a thermal cycling due to the relatively high repetition-rate and average power of this filament compared with past work. To our knowledge these are the first data presented on white-light continuum from a filament generated by the unamplified output directly from a sub-100 fs Ti: sapphire laser oscillator. One recent paper using multi-pass cavity oscillators operating in the PDR with much higher pump laser power, has also mentioned white light generation [117]. Past work using a cavity-dumped Yb:KYW laser with an additional stage of spectrum broadening and re-compression before generating filamentation [107, 109], greatly complicated the setup compared with the one discussed herein.

A.3 Conclusion

In conclusion, we have demonstrated the first cavity-dumped Ti: sapphire oscillator working in the positive dispersion regime. This results in a dramatic enhancement in the average and peak output power from such a laser, while still maintaining pulse duration of well under 100 fs. We believe that this pulse energy is currently limited by saturation of the KLM, and optimum operation can be obtained using a relatively-modest 6 Watt pump laser. Further improvement in the pulse energy might be obtainable using a SESAM, either through an increase in intracavity pulse energy, through an increased dumping of the intracavity pulse before instabilities arise, or through more

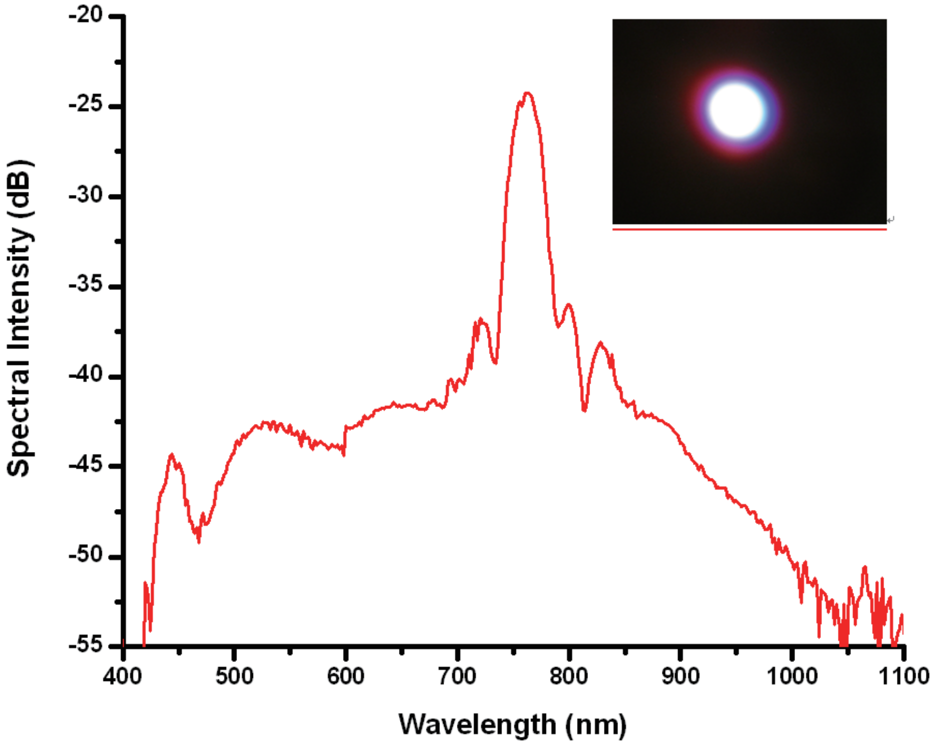

Figure A.6: Spectrum of the filament-induced white light. Inset: A digital photograph of the generated white light continuum.

freedom to optimize the power without losing mode locking. It is likely that energies exceeding 1 μJ can be obtained, and possibly much more with aggressive cooling of the crystal [118]. Such a compact and reliable high peak-power laser could be used for a variety of scientific and industrial applications such as micromachining, nonlinear frequency conversion, broad-band fs spectroscopy, and even strong field physics experiments. Carrier-envelope stabilization of such a laser oscillator, or using it as a seed source for CW-pumped active amplification [118, 119] to the tens of μJ level at MHz repetition rate may also be possible.